



POLITECNICO DI MILANO
DEPT. OF AEROSPACE SCIENCE AND TECHNOLOGY
DOCTORAL PROGRAMME IN AEROSPACE ENGINEERING

DRAG REDUCTION SYSTEMS
TOWARDS AERONAUTICAL APPLICATIONS

Doctoral Dissertation of:
Jacopo Banchetti

Supervisor:

Prof. Maurizio Quadrio

Tutor:

Prof. Luigi Vigevano

Coordinator:

Prof. Pierangelo Masarati

Academic year 2019/2020 – Cycle XXXII

"No matter how great the talent
or efforts, some things just take
time. You can't produce a baby in
one month by getting nine women
pregnant."

WARREN BUFFET

ABSTRACT

THIS Thesis mainly addresses the question: How does turbulent friction reduction measured in a lab experiment at low Reynolds numbers over a flat wall translate into potential savings for a commercial aircraft?

The first part tackles the problem by focusing on a specific drag reduction strategy, namely the streamwise travelling waves of spanwise velocity (StTW). A preliminary investigation based on the Reynolds-averaged-Navier-Stokes equations (RANS) estimates the potential benefit of StTW applied over the external surface of a commercial aircraft in transonic flight. It is found that StTW modifies the shock-wave position and increase lift, so that the interaction between friction reduction and the generation of aerodynamic forces is complex and potentially beneficial.

This suggestion is then more rigorously assessed via direct numerical simulations (DNS) of a turbulent channel flow, where a bump on the wall produces a pressure component of drag. Once again, StTW interacts with the pressure distribution, and pressure drag is reduced significantly. Moreover, the friction drag is reduced by an amount that overcomes the one obtained over a flat wall. Overall, this indicates that studying skin-friction drag reduction in simple geometries may hide potentially important effects.

The interaction between StTW and the components of the aerodynamic force is then studied via a compressible DNS for a wing slab in transonic flight. The qualitative results found in the preliminary RANS-based study are confirmed. Indeed, StTW interferes with the shock-wave position, consequently increasing lift and the overall aerodynamic efficiency, so that

the global performance of StTW largely overcomes the expectations. This is very interesting, especially because this result is general enough to hold for any (active or passive) friction reduction technique.

The second part of the Thesis shifts the focus to a relatively new friction reduction strategy based on non-uniform unsteady blowing. Direct numerical simulations are designed and conducted to accurately reproduce an ongoing experimental investigation, and lead to conclude that the non-uniformity and unsteadiness of the blowing jets play a minor role.

Finally, the fundamental problem of friction prediction over smoothly varying walls is discussed. Recent theories have put forward analytical formulas for the transfer function that translates the wall slope into the friction distribution. Their accuracy is assessed by comparing the predicted friction distribution with numerical results, denoting an interestingly good agreement in both the laminar and the turbulent regime.

SOMMARIO

Questa Tesi cerca principalmente di rispondere alla seguente domanda: Come si traduce la riduzione di attrito turbolento misurata durante esperimenti di laboratorio condotti su una lastra piana e bassi numeri di Reynolds, nel possibile guadagno per un aereo da trasporto?

La prima parte della Tesi affronta il problema concentrandosi su una specifica strategia di riduzione di attrito, ossia le onde di velocità trasversale, viaggianti in direzione longitudinale (StTW). Un'analisi preliminare basata sulle equazioni di Navier-Stokes mediate tramite media di Reynolds (RANS) stima il guadagno potenziale della tecnica StTW applicata sulla superficie esterna di un aereo commerciale in volo transonico. Si osserva che la StTW modifica la posizione dell'onda d'urto ed aumenta la portanza, in modo tale che l'interazione tra la riduzione di attrito e la generazione di forze aerodinamiche risulta non ovvia e potenzialmente benefica.

Questo indizio è stato in seguito investigato in maniera più rigorosa tramite simulazioni numeriche dirette (DNS) di una corrente turbolenta all'interno di un canale, dove un rigonfiamento della parete produce una componente di resistenza di pressione. Ancora una volta, la StTW interagisce con la distribuzione di pressione, e la resistenza di pressione è significativamente ridotta. Inoltre, la resistenza di attrito è ridotta di una quantità che supera la riduzione di attrito misurata su una parete piana. Globalmente, questo risultato conferma che studiare le tecniche di riduzione di resistenza d'attrito in geometrie semplici può nascondere effetti potenzialmente importanti.

Questa interazione tra StTW e le componenti della forza aerodinamica è studiata in seguito tramite DNS comprimibili attorno ad un segmento

di ala in volo transonico. I risultati qualitativi ottenuti nello studio preliminare basato su simulazioni RANS vengono confermati. Infatti, la StTW interagisce con la posizione dell'onda d'urto, e conseguentemente aumenta la portanza e l'efficienza aerodinamica, in modo tale che il guadagno globale dovuto alla StTW supera abbondantemente le aspettative. Questo risultato è particolarmente interessante, specialmente perché è abbastanza generale da valere per ogni tecnica di riduzione di attrito, che sia attiva o passiva.

La seconda parte della Tesi si focalizza su una tecnica di riduzione d'attrito relativamente nuova, basata su soffiaggio instazionario e non uniforme. Simulazioni numeriche dirette sono state condotte per riprodurre accuratamente una campagna sperimentale attualmente in corso, portando alla conclusione che sia la non uniformità che l'instazionarietà dell'attuatore giocano un ruolo trascurabile.

Infine è stato affrontato il problema teorico della predizione di attrito su una geometria con variazioni di pendenza moderate. Alcune teorie recenti hanno esplicitato formule analitiche della funzione di trasferimento, che permette di predire la distribuzione di attrito a partire dalla conoscenza della pendenza della parete. L'accuratezza di queste formule è valutata mettendo a confronto la predizione di attrito con risultati ottenuti tramite simulazioni numeriche, osservando un buon accordo sia in regime laminare che in regime turbolento.

TABLE OF CONTENTS

Abstract	IV
List of Figures	XI
List of Tables	XVII
1 Introduction	1
1.1 Motivation	1
1.2 Flow control techniques for viscous turbulent drag reduction	2
1.3 Spanwise forcing	5
1.4 Towards practical applications	7
1.5 Dissertation overview	13
1.6 Bibliography disclaimer	15
I Towards drag reduction of a transonic transport aircraft	17
2 Drag reduction of a whole-aircraft configuration	19
2.1 Introduction	20
2.2 Simulations	22
2.3 Friction and pressure coefficients	25
2.4 Aerodynamic forces	28
2.5 Global power budget	32
2.6 Conclusions	34
3 Turbulent drag reduction over curved walls	35
3.1 Introduction	36
3.2 Simulations	38

TABLE OF CONTENTS

3.3 Instantaneous and mean flow fields	41
3.4 Skin friction and pressure at the wall	45
3.4.1 Drag coefficients	48
3.4.2 Changes in friction and pressure drag over the curved wall	50
3.4.2.1 Friction drag reduction	51
3.4.2.2 Pressure drag reduction	54
3.5 Global power budget	58
3.6 Conclusions	61
4 Drag reduction for a transonic wing slab	63
4.1 Introduction	64
4.2 Simulations	65
4.3 Instantaneous and mean flow fields	68
4.4 Friction and pressure coefficients	72
4.5 Aerodynamic Forces	75
4.6 Global power budget	77
4.7 Conclusions	77
II Wall friction: manipulation and prediction	79
5 Wall-normal jets for skin-friction reduction	81
5.1 Introduction	82
5.2 Simulations	84
5.3 Spanwise non-uniformity	87
5.4 Unsteadiness	92
5.5 Global power budget	95
5.6 Combination of jets with spanwise forcing	98
5.7 Conclusions	101
6 Linear response of turbulent flows over generic bumps	103
6.1 Introduction	104
6.2 Friction prediction in laminar flows	105
6.3 Friction prediction in turbulent flows	109
6.4 Comparison with literature data	111
6.5 Conclusions	116
7 Conclusions	117
7.1 Roadmap of future research and development	119
Bibliography	123

LIST OF FIGURES

1.1	Classification of friction reduction techniques according to Gad-el-Hak (2001).	3
1.2	Schematic of the system for turbulent channel flow with oscillating walls. Adapted from Ricco and Quadrio (2008).	5
1.3	Mean spanwise velocity profiles; different curves represent different instances in time during an oscillating period. Comparison between DNS (left) and analytical Stokes Layer (right). Adapted from Choi, Xu, and Sung (2002).	6
1.4	Schematic of the system for turbulent channel flow with streamwise travelling waves. κ_x and ω represent the spatial and temporal frequencies of the wave, while λ_x is the streamwise wavelength. Adapted from Quadrio, Ricco, and Viotti (2009).	8
1.5	Mean velocity profiles obtained in a channel flow at $Re_\tau = 200$. The solid line is the reference case and the other lines correspond to StTW yielding both drag reduction (positive shift) and drag increase (negative shift). Adapted from Gatti and Quadrio (2016).	10
2.1	Comparison of the pressure coefficient, with and without riblets, over a wing section of the CRM aircraft. Here, x/c is the non-dimensional chord-wise coordinate and c_p is the pressure coefficient. Taken from Mele, Tognaccini, and Catalano (2016).	21
2.2	Wing-body configuration of the DLR-F6 aircraft.	22

List of Figures

2.3 Sketch of the computational domain and the reference system. The aircraft is on the symmetry plane.	23
2.4 3D view of the DLR-F6 configuration. Colour plot of the friction coefficient c_f (left) and the pressure coefficient c_p (right).	26
2.5 3D view of the DLR-F6 configuration. Colour plot of the local friction reduction $r\%$ (left) and the local pressure reduction $\Delta p\%$ (right).	27
2.6 Comparison of pressure coefficient between reference (red) and controlled (blue) case over a wing section.	27
2.7 Comparison of drag coefficients as a function of AoA . First panel: reference (red) and controlled (blue) C_d ; second panel: computed $\Delta C_d\%$ (thick line) compared with the extrapolated one (thin line with symbols).	29
2.8 Pressure (lines with squares) and friction (lines with circles) drag components. Top: reference (red) and controlled (blue) cases; bottom: pressure and friction drag reduction $\Delta C_{d,p}$ and $\Delta C_{d,f}$, respectively.	30
2.9 Comparison of lift coefficient, between reference (red) and controlled (blue) cases.	31
2.10 Comparison of drag coefficients as a function of C_ℓ . Top reference (red) and controlled (blue) C_d ; bottom: computed $\Delta C_d\%$ compared with the extrapolated one (thin line with symbols).	32
2.11 Net power savings as a function of C_ℓ : computed P_{net} compared with the extrapolated one (thin line with symbols).	33
3.1 Sketch of the computational domain and the reference system. The bump is on the lower wall. The streamwise-periodic upstream domain (black) provides an inflow condition for the downstream one (blue).	39
3.2 Bump geometries G_1 (blue line) and G_2 (black dashed line); they are identical up to the bump tip. Both have height of $h_b = 0.0837$ (only a portion of the streamwise extent is shown; note the enlarged vertical axis). G_1 leads to a mildly separated flow, while G_2 produces an attached flow.	41
3.3 Isosurfaces of $\lambda_2^+ = -0.04$ for an instantaneous flow field in the reference case. Isosurfaces are colour-coded with the coordinate z	42

- 3.4 Colour plot of an instantaneous streamwise velocity field, in the plane $z = 0.08$ over the bump G_1 , for the reference case (top) and with StTW (bottom). Flow is from left to right, and the upstream periodic section ends at $x = 0$ 43
- 3.5 Colour plot of an instantaneous spanwise velocity field, in the plane $z = 0.08$ over the bump G_1 . Panels as in figure 3.4. 43
- 3.6 Colour plot of the mean vertical velocity $\langle w \rangle$ for the bump G_1 : top, reference case; bottom, StTW. Positive contours (continuous lines) are drawn for $\langle w \rangle = (0.05, 0.065, 0.08)$, and negative contours (dashed lines) are drawn for $\langle w \rangle = (-0.02, -0.015, -0.01)$. The thick black line indicates $\langle u \rangle = 0$ and marks the boundary of the separated region. 44
- 3.7 Colour map of the mean pressure $\langle p \rangle$ for the bump G_1 : top, reference case; bottom, StTW. Positive contours (continuous lines) are drawn for $\langle p \rangle = (0.05, 0.0525, 0.055)$, and negative contours (dashed lines) are drawn for $\langle p \rangle = (-0.05, -0.04, -0.03)$. 44
- 3.8 Skin-friction distribution $c_f(x)$ over the wall with the bump. Top: comparison between the reference case (red) and the controlled case (blue) for bump G_1 . Bottom: local skin-friction reduction rate $r(x)$ for G_1 (blue) and G_2 (black dashed). The thin profiles at the bottom of the plots draw the two bumps, in arbitrary vertical units. 46
- 3.9 Pressure distribution $c_p(x)$ over the wall with the bump. Top: comparison between the reference case (red) and the controlled case (blue) for bump G_1 . Bottom: local difference between pressure coefficients $\Delta c_p(x) = c_p(x) - c_{p,0}(x)$ for G_1 (blue) and G_2 (black dashed). The thin profiles at the bottom of the plots draw the two bumps, in arbitrary vertical units. 47
- 3.10 Changes in the skin-friction component of the total drag. Top: the computed $\Delta c_{d,f}$ (thick line) compared with the extrapolated $\Delta c_{d,f}^{(e)}$ (thin line with labels) for bump G_1 . Center: difference between computed and extrapolated friction drag reduction, for geometries G_1 (blue line) and G_2 (black dashed line). Bottom: difference between actual R_f and extrapolated integral budget $R_f^{(e)}$ for both geometries. The thin profiles at the bottom of the plot draw the two bumps, in arbitrary vertical units. 52
- 3.11 Colour plot of the turbulent kinetic energy, in outer units, for the bump G_1 (top) and G_2 (bottom), with and without StTW. 53

List of Figures

3.12 Colour plot of the production P of turbulent kinetic energy. The level $P = 0$ is indicated by the contour line. Panels as in figure 3.11.	55
3.13 Comparison of the contribution to pressure drag changes between G_1 (blue) and G_2 (black dashed). Top: $\Delta c_{d,p}(x)$; bottom: integral budget R_p for both geometries. The thin profiles at the bottom of the plot draw the two bump ge- ometries.	56
3.14 Contour of the probability γ_u of non-reverse flow, without (top) and with (bottom) StTW over the bump G_1 . Black lines identify contours of $\gamma_u = (0.50, 0.80, 0.99)$ involved in the definitions by Simpson, Chew, and Shivaprasad (1981).	58
3.15 Streamlines of the mean flow field, without (top) and with (bottom) StTW over the bump G_1 . Black lines identify con- tours of $\gamma_u = (0.50, 0.80, 0.99)$	58
3.16 Streamwise mean velocity profile in the periodic plane chan- nel. Comparison between reference flow (red) and actuated flow on the lower wall (blue).	60
4.1 Sketch of a weak (left) and strong (right) transonic SBLI. Taken from Babinsky and Harvey (2011).	65
4.2 Cross-section of the computational mesh, with the whole domain on the left and a zoom on the airfoil on the right. Adapted from Memmolo (2018).	66
4.3 Airfoil geometry V2C (blue) plotted together with the NACA0012 airfoil (gray, dotted). The red lines denote the location where forcing starts and ends.	66
4.4 Magnitude of the pressure gradient vector $ \nabla p $ of an in- stantaneous flow field around the airfoil in the controlled case.	68
4.5 Chord-wise velocity component over the suction side of the airfoil: uncontrolled (top) and controlled (bottom) case. The red lines denote the location where forcing starts and ends.	69
4.6 Mean pressure distribution around the airfoil. Top: refer- ence case. Bottom: controlled case.	70
4.7 Distribution of the mean Mach number around the con- trolled airfoil. Contour lines are drawn at $M = 1$ for the reference (white) and controlled (black) cases. The lower panel enlarges the portion of the flow field around the shock- waves.	71
4.8 Numerical Schlieren $\partial\langle\rho\rangle/\partial x$ around the airfoil. Top: refer- ence case; bottom: controlled case.	72

4.9 Comparison between reference (red) and controlled (blue) skin-friction distribution $c_f(x)$ over the airfoil. Top: c_f over the suction side; center: friction reduction rate $r(x)$ over the suction side; bottom: c_f over the pressure side.	73
4.10 Chord-wise velocity component over the suction side of the airfoil, coloured to detect attached (beige) and separated (burgundy) areas: uncontrolled (top) and controlled (bottom) case. The red lines denote the location where forcing starts and ends.	75
4.11 Comparison of pressure coefficient between reference (red) and controlled (blue) cases.	75
5.1 A schematic of the drag reduction mechanism: (a) control off; (b) control on. The transverse-travelling wave formed by the wall-based discrete actuators generates a layer of highly regularised streamwise vortices, which acts to weaken or even break the connection between the large-scale coherent structures and the wall. Taken from Bai et al. (2014).	83
5.2 Sketch of the computational domain and the reference system. The streamwise-periodic upstream domain (black) provides the inflow boundary condition for the downstream one (blue) which includes the actuator.	84
5.3 Sketch of non-uniform blowing actuator.	86
5.4 Colour plot of an instantaneous wall-normal velocity field, in the plane $x = 4.9$, passing through the actuator for the cases U-S (top) and NU-S (bottom). Contour lines (dotted) are drawn for $w = 0$	88
5.5 Isosurfaces of $\omega_x^+ = \pm 0.25$ (red and blue) that identify the regularised streamwise vortices and isosurfaces of $\lambda^+ = -0.02$ (colour-coded with the wall-distance z^+) for an instantaneous flow field of case U-S (top) and NU-S (bottom). The black lines denote the location where forcing starts and ends.	89
5.6 Colour plot of an instantaneous streamwise velocity field, in the plane $z = 0.05$, for the case U-S (top) and NU-S (bottom). Flow is from left to right, and the downstream non-periodic section starts at $x = 0$	90
5.7 Colour plot of the mean wall-normal velocity $\langle w \rangle$, for case U-S (top) and NU-S (bottom). The latter is shown over two planes: above the wall (second panel) and above the slit (third panel). Contour lines are drawn for $\langle w \rangle = (0.01, 0.028)$.	90

5.8 Skin-friction distribution $c_f(x)$: cases U-S (black) and NU-S (red) over the lower (solid lines) and upper (dashed lines) walls.	91
5.9 Colour plot of the turbulent kinetic energy, in outer units. Panels as in figure 5.7. Contour lines are drawn for $k = 0.018$	92
5.10 Temporal evolution of one period of the unsteady actuator U-NS (green). Four points underline the instants investigated in the following. The black dashed line denotes the steady forcing of case U-S.	93
5.11 Colour plot of the mean wall-normal velocity $\langle w \rangle$ for case U-NS in four moments of the period: zero W_w , acceleration, maximum W_w and deceleration respectively. Contour lines are drawn for $\langle w \rangle = (0.01, 0.028)$ for case U-NS (solid lines) and compared to the steady case U-S (dashed lines).	94
5.12 Skin-friction distribution $c_f(x)$: cases U-S (black) and U-NS (green) over the lower (solid lines) and upper (dashed lines) walls.	95
5.13 Colour plot of the production P of turbulent kinetic energy, for case U-S (top) and U-NS (bottom). The latter is shown in four instants of the forcing period, with panels as in figure 5.11. Contour lines are drawn for $P = (0.014)$	96
5.14 Colour plot of the mean wall-normal velocity $\langle w \rangle$, for case StW over two planes: above the wall (first panel) and above the slit (second panel). Contour lines are drawn for $\langle w \rangle = (0.01, 0.028)$ for case StW (solid lines) and compared to the steady case NU-S (dashed lines).	98
5.15 Skin-friction distribution $c_f(x)$: cases NU-S (red) and StW (blue) over the lower (solid lines) and upper (dashed lines) walls.	99
5.16 Colour plot of the turbulent kinetic energy, in outer units, for cases NU-S (top) and StW (bottom). Note the different colour-map scale. Contour lines are drawn at $k = 0.018$ for case NU-S and at $k = 0.009$ for case StW.	100
5.17 Colour plot of δk for case NU-S (top) and case StW (bottom).	100
6.1 Module of the transformed wall-slope $\mathbf{k}^+ \widehat{G_1^+} $ (black) and comparison between the asymptotic response function (6.2) (solid lines) and classical theory (Benjamin, 1959) (dashed lines): real (blue) and imaginary (red) components.	106

6.2 Wall-shear stress perturbation $\delta\tau$ for the five bumps $\frac{G_1}{a}$: $a = 1$ (blue), $a = 2$ (red), $a = 4$ (green), $a = 8$ (brown), $a = 16$ (cyan). Top: $\delta\tau$; bottom: $a\delta\tau$. The thin profiles at the bottom of the plot draw the five bump geometries.	107
6.3 Wall-shear stress perturbation $\delta\tau$: computed (thick colour line, colour-coded as in figure 6.1) and predicted (thin black lines) for the five geometries. Note the vertical scale that is multiplied by $1/a$	108
6.4 Bump geometries G_1 (blue), G_{1h} (red) and G_{1L} (green). . .	109
6.5 Wall-shear stress perturbation $\delta\tau$: computed (thick colour lines, colour-coded as in figure 6.4) and predicted via asymptotic (thin solid lines, black) and empirical (thin dashed lines, black) transfer functions. Top: G_1 ; centre: G_{1h} ; bottom: G_{1L}	110
6.6 Different bump geometries analysed by Mollicone et al. (2018), given by $y = -a(x - 4)^2 - 0.5$. $a = 0.15$ (blue), $a = 0.25$ (red) and $a = 0.5$ (green).	112
6.7 Wall-shear stress perturbation $\delta\tau$: computed (thick colour lines, colour-coded as in figure 6.6), and predicted via the asymptotic (thin solid lines, black) and empirical (thin dashed lines, black) transfer functions. First panel: $a = 0.5$; second panel: $a = 0.25$; third, fourth and fifth panels: $a = 0.15$ at $Re_\tau = 160 - 280 - 550$, respectively. DNS data taken from Mollicone et al. (2018)	113
6.8 Different bump geometries analysed by Wu and Squires (1998) and Matai and Durbin (2019): $h_b/\ell_b = 0.066$ (blue), $h_b/\ell_b = 0.137$ (red).	114
6.9 Wall-shear stress perturbation $\delta\tau$: computed (thick colour lines, colour-coded as in figure 6.8), and predicted via asymptotic transfer function 6.2 (black lines). First panel: $h_b/\ell_b = 0.066$ with $\ell_b^+ = 6200$; second panel: $h_b/\ell_b = 0.066$ with $\ell_b^+ = 8500$; third panel: $h_b/\ell_b = 0.137$ with $\ell_b^+ = 8500$. DNS data taken from Wu and Squires (1998) and Matai and Durbin (2019).	115

LIST OF TABLES

2.1	Comparison of the simulation setup between Mele, Tognacini, and Catalano (2016) and the present project.	25
2.2	Force coefficients. Here, $C_{d,f}$ and $C_{d,p}$ are the friction and pressure components respectively, with $C_d = C_{d,f} + C_{d,p}$. C_ℓ is the lift coefficient, while L/D represents the lift/drag ratio.	30
3.1	Drag coefficients for the bump G_1 . Here $C_{d,f}$ and $C_{d,p}$ are the friction and pressure components respectively, with $C_d = C_{d,f} + C_{d,p}$. Distributed losses are computed according to Eq. (3.8) in the planar geometry while concentrated losses introduced by the bump are evaluated via Eq.(3.9). Figures are for the lower wall only.	49
3.2	Drag coefficients for the bump G_2	50
3.3	Detachment and reattachment points for the reference and controlled cases, along with longitudinal extent deduced for specified values of the probability function γ_u	57
3.4	Power budget for the bump G_1 . Here, P_{tot} is the power required to overcome the total drag produced by the lower wall, P_{req} is the power required for actuation, and $P_{net} = P_{tot} - P_{req}$ represents the net balance. Figures are for the lower wall only.	59
3.5	Power budget for G_2 , as in table 3.4.	60
4.1	Force coefficients. Here $C_{d,f}$ and $C_{d,p}$ are the friction and pressure components of drag respectively, with the total drag $C_d = C_{d,f} + C_{d,p}$ and C_ℓ is the lift coefficient, while L/D represents the lift/drag ratio.	76

List of Tables

5.1 Details of the blowing strategy employed. Here S_j/S_{tot} represents the fraction of the spanwise width covered by jets (unitary for uniform blowing); f^+ is the forcing frequency of the unsteady cases, W_w^+ is the blowing wall-normal velocity. The case StW investigates the blowing actuator over a spanwise-controlled wall by a standing wave with parameters $(A^+, \kappa_x^+) = (12, 0.01)$	86
5.2 Power budget for the four cases. P_{sav} is the power saved thanks to the reduction of friction drag. P_{req} is the power required for actuation, and $P_{net} = P_{sav} - P_{req}$ represents the net balance. Figures are for the lower wall only and are expressed as a percentage of P_{tot} , which is the power required to overcome the drag produced by the lower wall.	97
6.1 Relative error for maximum (Δ_M) and minimum (Δ_m) of $\delta\tau$	109
6.2 Relative error of the analytical (6.2) and empirical (6.4) prediction, for the local minimum (Δ_{lm}), the maximum (Δ_M) and minimum (Δ_m) of $\delta\tau$. Error via empirical transfer function (6.4) is reported in parentheses.	111

CHAPTER 1

INTRODUCTION

People don't buy WHAT you do,
they buy WHY you do it.

SIMON SINEK

THE present work deals with turbulent skin-friction drag reduction techniques with a far-sighted eye pointed on the aeronautical field. This chapter provides an overview of the motivation, the background and the organization of the present Thesis.

1.1 Motivation

Skolstrejk för klimatet is a worldwide known slogan of the climate activist Greta Thunberg. Climate change is commonly considered the biggest challenge of this century.

In this context, transportation plays a role of primary importance, since, for example in Europe, it is responsible for approximately one-quarter of the total emissions (European Environment Agency, 2019). In the

aeronautical field, known to be associated to one of the most polluting way of travelling, turbulent skin-friction is responsible for almost one-half of the total emissions (Gad-el-Hak, 1994). Nowadays, reducing skin-friction turbulent drag is, in fact, the primary goal of a considerable number of researchers around the world.

1.2 Flow control techniques for viscous turbulent drag reduction

Turbulent friction reduction mainly derives from the physical understanding of turbulent coherent structures. In wall-bounded turbulent flows, streaks of high/low velocity and quasi-streamwise vortices play a key role in the near-wall region (Kline et al., 1967). These structures interact among each other in a self-sustaining cycle, known as the 'near-wall cycle' (Jiménez and Pinelli, 1999). This process is responsible for the increase of skin-friction in turbulent flows (Orlandi and Jiménez, 1994).

Many flow control techniques have targeted the near-wall cycle to reduce friction; a classification of these techniques has been proposed by Gad-el-Hak (2001) and illustrated in figure 1.1. The simplest approach concerns passive strategies that do not require actuation power and usually consists of modification of the wall shape. One of the most famous passive techniques is riblets (García-Mayoral and Jiménez, 2011), and derives from observation of the shark-skin grooves. By employing different shapes and configurations, riblets are capable of reducing friction up to 10% (Walsh and Lindemann, 1984), and represent one of the techniques with the highest Technical Readiness Level for practical applications (Spalart and McLean, 2011).

More complex strategies involve active approaches, requiring, for example, the movement of the bounding surface or injection of mass, and typically yield a more significant amount of friction reduction. Active wall manipulation in order to reduce turbulent friction has been introduced in several configurations, providing encouraging results. An effective example of in-plane motion has been proposed by Jung, Mangiavacchi, and Akhavan (1992) who imposed a periodic spanwise oscillation of the lower wall of a channel. They observed a strong influence of the oscillating period in the amount of friction drag, which is reduced up to 40%. Nakanishi, Mamori, and Fukagata (2012) provided an example of out-plane wall motions, obtaining a full relaminarization of the channel flow, by imposing travelling wave-like wall deformation, i.e. peristalsis. Active actuation of the wall, however, does not necessarily concern wall movements. In this context, Kametani and Fukagata (2012) studied the effect of uniform cooling and

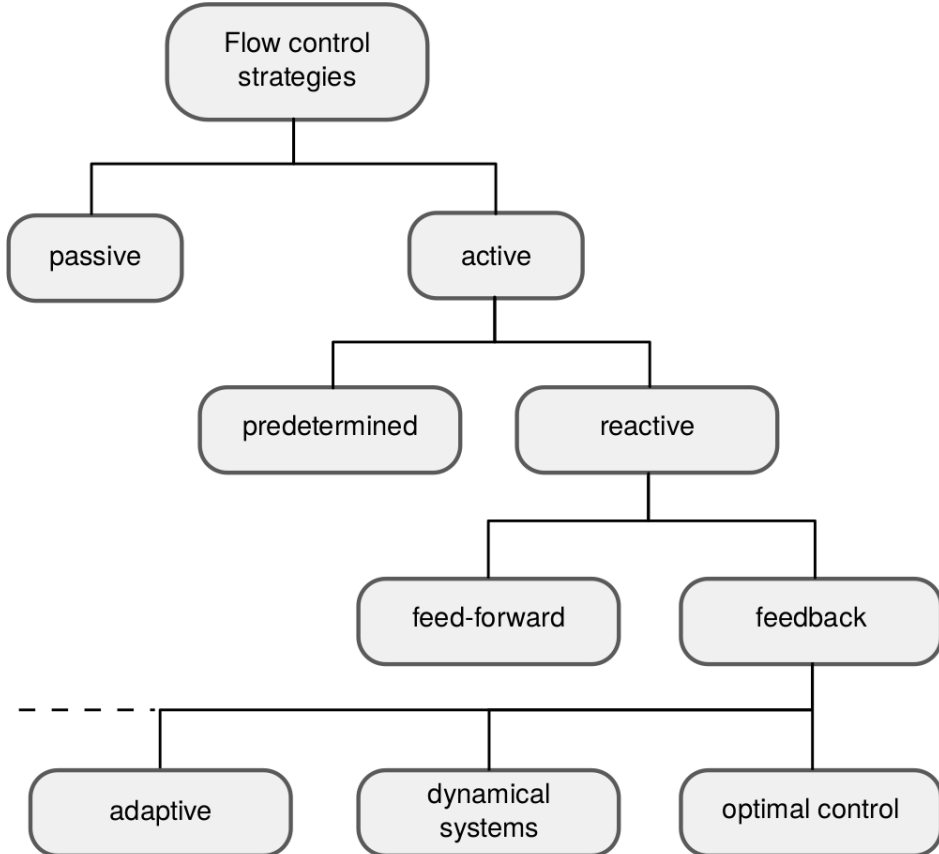


Figure 1.1: Classification of friction reduction techniques according to Gad-el-Hak (2001).

uniform heating over a spatially developing boundary layer. The heated plate is shown to increase friction drag, while uniform cooling provided a 65% of friction reduction. Berger et al. (2000) on the other hand, manipulated the near-wall flow via the application of plasma actuators, which rely on the Lorentz force. They observed a considerable amount of friction reduction, while noticing that the actuation power strongly decreases the overall performances. Another well-known friction reduction technique relies on the injection of flow mass which has been studied since the mid of the 20th century (Mickley et al., 1954).

Regardless of the employed flow control technique, the actuation law can be predetermined or can benefit from information of the flow field obtained via sensor measurements. An example of reactive strategy is the opposition control of blowing and suction, proposed by Choi, Moin, and Kim (1994) in their numerical investigation. Here the information of the

flow field over a plane parallel to the wall is used to detect the quasi-streamwise vortices. The blowing or suction velocity imposed at the wall is the opposite of the wall-normal velocity measured in the sensor plane, in order to suppress sweep and ejection events. Thanks to the successful implementation of this strategy they observed a friction reduction of 25%. A similar opposition control strategy has been then investigated via out-of-plane wall movement by Endo, Kasagi, and Suzuki (2000), which obtained a total drag reduction higher than 10%. However, the effectiveness of active flow control techniques is not addressed by the amount of friction reduction alone: the required actuation power must be taken into account.

Friction reduction techniques are often studied via Direct Numerical Simulations (DNS) in a simplified setup, e.g. the periodic channel flow. In such a configuration, since both streamwise and spanwise directions are homogeneous, after time average friction can be quantified by a single integral coefficient, namely C_f . For simplicity, the main quantities of interest are here introduced as integral coefficients. At the same time, it should be mentioned that local expressions should be employed when complex setups are considered, as we will see in the following chapters.

In the homogeneous settings of a channel flow, the actuator's efficiency is expressed via the relative change of C_f between the controlled and the reference flow, namely the friction reduction rate \mathcal{R} . The above non-dimensional values are defined as

$$C_f = \frac{2\tau}{\rho U_b^2}, \quad \mathcal{R} = 1 - \frac{C_f}{C_{f,0}}, \quad (1.1)$$

where τ is the wall-shear stress, ρ is the fluid density, U_b is the bulk velocity, and the subscript 0 indicates a quantity measured in the reference flow. Active strategies usually yield a higher amount of \mathcal{R} , however, they require actuation power P_{req} . According to Kasagi, Hasegawa, and Fukagata (2009), the net power savings P_{net} is defined as the budget between the saving and the actuation cost:

$$P_{net} = \frac{P_0 - P - P_{req}}{P_0} = \mathcal{R} - \frac{P_{req}}{P_0}, \quad (1.2)$$

where P is the total power required by the channel to drive the flow. Passive strategies do not require actuation power and P_{net} coincides with \mathcal{R} . Active strategies, on the other hand, usually require a high amount of P_{req} , and face the challenge to reduce friction while limiting their actuation cost.

1.3 Spanwise forcing

In terms of net power savings, the family of spanwise forcing techniques has shown attractive features. The first demonstration of the effectiveness of spanwise wall movement has been provided by Jung, Mangiavacchi, and Akhavan (1992). They introduced the oscillating wall strategy which is sketched in figure 1.2 and defined as

$$V_w(x, t) = A \sin(\omega t), \quad (1.3)$$

where V_w is the spanwise velocity at the wall, A is its maximum amplitude, and ω represents temporal frequency. An important step in order

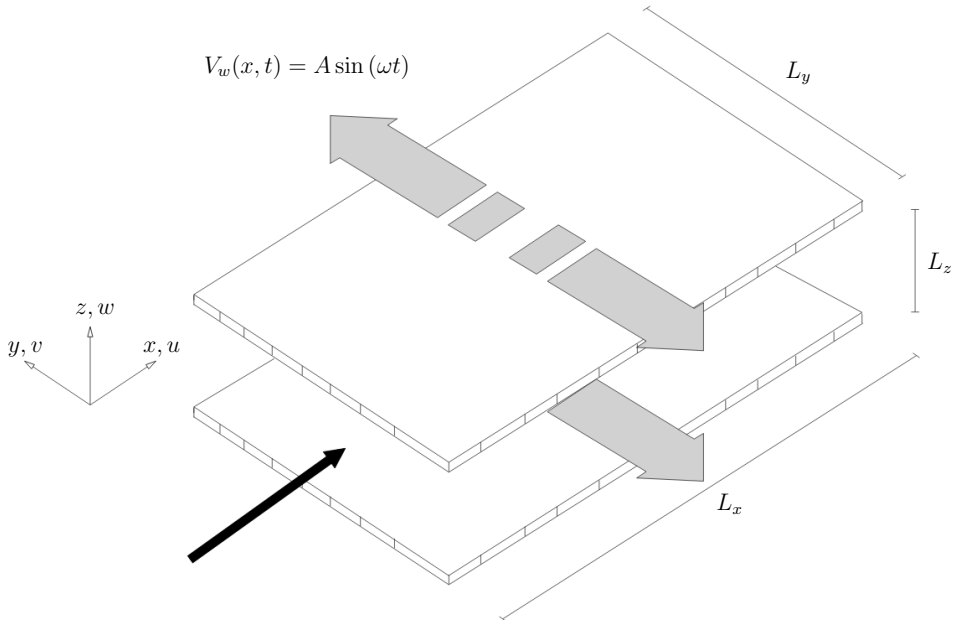


Figure 1.2: Schematic of the system for turbulent channel flow with oscillating walls. Adapted from Ricco and Quadrio (2008).

to understand the physical mechanism beyond spanwise forcing derives from observations of Quadrio and Sibilla (2000) and Choi, Xu, and Sung (2002), who suggested that the oscillations induce a spanwise alternating flow that, once space-averaged, follows the analytical solution of the laminar Stokes Layer (SL). A sketch of the spanwise velocity profile inside the SL is portrayed in picture 1.3, where the analytical solution is compared with DNS measurements performed by Choi, Xu, and Sung (2002). The thickness of the Stokes Layer is of the order of a few wall units, and its interaction with the near-wall turbulence induces a reduction of the friction

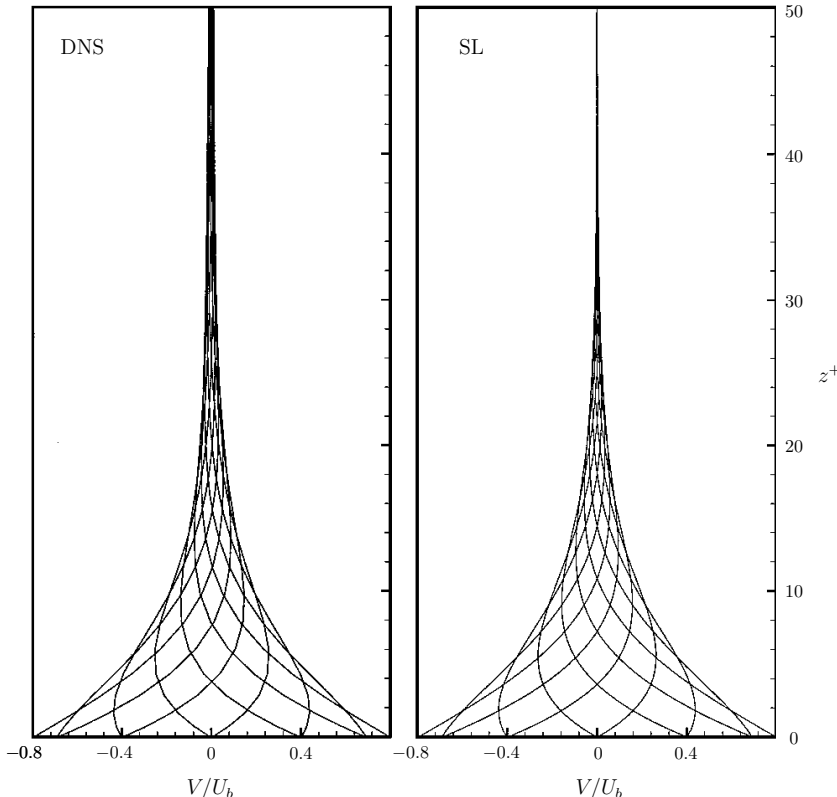


Figure 1.3: Mean spanwise velocity profiles; different curves represent different instances in time during an oscillating period. Comparison between DNS (left) and analytical Stokes Layer (right). Adapted from Choi, Xu, and Sung (2002).

drag. Moreover, Duggleby, Ball, and Paul (2007) observed that the peak of velocity fluctuations as well as the turbulent structures are pushed at higher distance from the wall by the Stokes layer.

Quadrio and Ricco (2004) extensively investigated the forcing parameters performing hundreds of DNS of a channel flow. They found that an optimal period of oscillation is present at constant A^+ , around $T_{opt}^+ \sim 100$. Moreover, they observed values of friction reduction up to 50%, while the high amount of power required to oscillate the wall drastically reduces its effectiveness, with a maximum $P_{net} \sim 10\%$.

Viotti, Quadrio, and Luchini (2009) reproduced via spatial oscillating forcing the effect of the temporal oscillation on the near-wall flow. Close to the wall, in fact, the convection becomes constant with a convection velocity of $\mathcal{U}^+ \sim 10$ (Kim and Hussain, 1993). The temporal forcing is then

translated into a spatially sinusoidal forcing, defined as

$$V_w(x, t) = A \sin(\kappa_x x), \quad (1.4)$$

where κ_x represents the spatial frequency. Viotti, Quadrio, and Luchini (2009) observed an almost perfect translation between temporal and spatial oscillation, and the optimal performances are obtained when the wavelength, defined as $\lambda_x = 2\pi/\kappa_x$, is tuned as $\lambda_{opt} \sim \mathcal{U}^+ T_{opt}$. Although the friction reduction is similar to the oscillating wall case, the stationary wave induces a net power saving up to 20%.

Spanwise forcing evolved then in the more efficient streamwise-travelling waves of spanwise velocity (StTW), introduced by Quadrio, Ricco, and Viotti (2009). The StTW yields significant net savings and has been selected for this Thesis since it enjoys large enough performances to make their accurate characterization relatively easy. The StTW corresponds to a non-homogeneous and unsteady boundary condition for the spanwise velocity component, depicted in figure 1.4 inside a channel flow, and it is defined as follows:

$$V_w(x, t) = A \sin(\kappa_x x - \omega t). \quad (1.5)$$

Quadrio, Ricco, and Viotti (2009) investigated via turbulent channel flow DNS several parameters of the StTW, observing a net power saving up to 30%. Later, Quadrio and Ricco (2011) observed that StTW induces a spanwise velocity profile within a small distance from the wall, called Generalized Stokes Layer, by studying StTW in laminar regime. The drag reducing effect of streamwise-travelling waves has been successfully demonstrated experimentally in a pipe flow by Auteri et al. (2010). Here the pipe is divided in thin longitudinal slabs that are actuated with different rotation rates. Moreover, several experimental studies reproduced the spanwise forcing strategies via novel technologies like plasma actuator (Choi, Jukes, and Whalley, 2011) or electroactive polymers (Gatti et al., 2015).

In addition, studies of turbulent boundary layers (Skote, 2011) demonstrated the efficiency of spanwise forcing even in external flows.

1.4 Towards practical applications

Although research on both passive and active approaches has achieved and is achieving interesting results, several obstacles still separate theory from practical applications. These hindrances are related to both practical

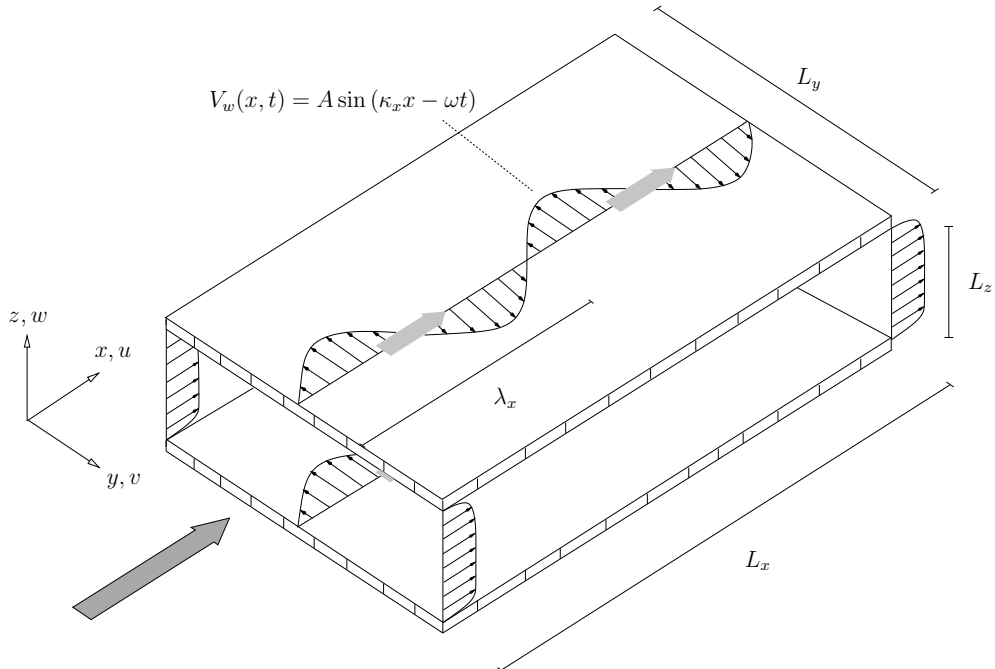


Figure 1.4: Schematic of the system for turbulent channel flow with streamwise travelling waves. κ_x and ω represent the spatial and temporal frequencies of the wave, while λ_x is the streamwise wavelength. Adapted from Quadrio, Ricco, and Viotti (2009).

issues and lack of theoretical understanding. With specific reference to the aeronautical field, where the length scale of turbulent structures is comparable to the thickness of a human hair, any control actuator needs to be consequently miniaturized. Simple passive strategies may be ready for this challenge, but the small scale mandates a substantial increase in manufacturing and maintenance costs. More advanced techniques, on the other hand, require high-frequency wall movements that are nowadays practically impossible to achieve over the external surface of a commercial aircraft. Practical issues, however, are not addressed in this Thesis, which is focused on the theoretical understanding.

Theoretical knowledge, which fundamental fluid mechanics is more concerned of, is still limited by the application of flow control mostly to simplified settings, which lack to represent the complexity of practical applications faithfully. Indeed, our knowledge of friction reduction strategies derives essentially from simulations or experiments performed in simple geometries, such as a channel flow, and at low values of the Reynolds number Re . However, practical applications present high Re and complex geometries, where friction is not the sole component at play to create

aerodynamic drag. In the case of a commercial aircraft, for example, the pressure component of drag is comparable to the frictional one, and lift plays, of course, a non-negligible role. Due to the simplistic setup in which friction reduction techniques are commonly investigated, the interaction between friction drag reduction and the other components is still almost unexplored. The increase of Reynolds number, on the other hand, makes it impossible, nowadays, to numerically reproduce friction reduction systems reliably, and only an estimation of its effect can be provided. Moreover, dealing with aircraft in cruise flight, the Mach numbers in play largely overcome the typical value assessed to delimit the incompressible regime. However, the effect of compressibility in the friction reduction effectiveness is marginally studied and still debated (Yao and Hussain, 2019). These limitations prevent us from estimating the true potential of skin-friction reduction in practical applications. Nowadays, we are still unable to reliably translate the percentage of \mathcal{R} measured in a lab experiment (or numerical simulation) into the global energy savings of an aircraft in cruise flight.

In the context of spanwise forcing (the main character of this Thesis), while the effect of wall curvature and the interaction with other components of forces remains to be explored, the effect of Re is known to degrade the friction reduction performances. Touber and Leschziner (2012) for example estimated a severe drop of the maximum achievable drag reduction as the Reynolds number increases, namely proportional to $Re^{-0.2}$. Obviously, with such a rapid drop one guesses that at flight-Reynolds-numbers there are no benefits left. However, Duque-Daza et al. (2012), by modelling the StTW via linearized Navier-Stokes equations, observed that the control effect on the near-wall streaks is almost independent of the Reynolds number.

More recently, Gatti and Quadrio (2016) investigated, via turbulent channel flow simulations, a wide range of StTW parameters at two different Reynolds numbers. They first linked the changes induced by StTW on the mean velocity profile, to skin-friction drag changes of a rough wall. The streamwise mean velocity profile $\langle u \rangle(z)$ over smooth walls presents first a thin near-wall region, called the viscous sublayer (Pope, 2000). If we consider the superscript $+$ to indicate viscous units, the viscous sublayer presents a mean velocity profile where $\langle u \rangle^+ = z^+$ and it is connected through the buffer region to the logarithmic layer, where the profile follows a logarithmic law:

$$\langle u \rangle^+ = \frac{1}{\kappa} \ln(z^+) + B, \quad (1.6)$$

where κ is the von Kármán constant and B is the near-wall intercept.

In case of rough walls, the statistical description of roughness-induced effects (Jiménez, 2004) is the negative change ΔB of the additive constant B : the logarithmic portion of the velocity profile is shifted downward. Gatti and Quadrio (2016) verified, in analogy with other friction reduction techniques like riblets (Choi, 1989), large-eddy breakup devices LEBU (Bandyopadhyay, 1986) and long-chain polymers (Lumley, 1973), that StTW produces an upward shift of the logarithmic portion of the mean velocity profile. ΔB presents a sign inversion when StTW is tuned to produce drag increase, as shown in figure 1.5.

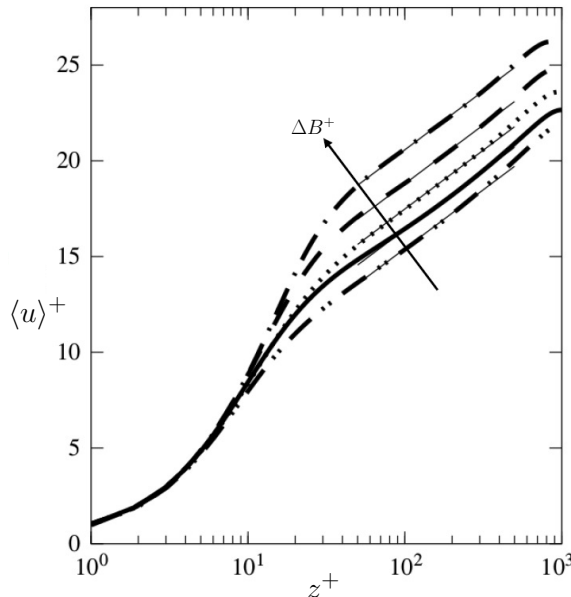


Figure 1.5: Mean velocity profiles obtained in a channel flow at $Re_\tau = 200$. The solid line is the reference case and the other lines correspond to StTW yielding both drag reduction (positive shift) and drag increase (negative shift). Adapted from Gatti and Quadrio (2016).

The vertical shift ΔB^+ is then observed to be linked to the friction-reduction-rate \mathcal{R} , via the equation:

$$\Delta B^+ = \sqrt{\frac{2}{C_{f,0}}}[(1 - \mathcal{R})^{-1/2} - 1] - \frac{1}{2\kappa} \ln(1 - \mathcal{R}). \quad (1.7)$$

Thanks to the Reynolds independence of ΔB^+ , when computed in (actual) wall units, the achievable \mathcal{R} over a plane channel at the desired Re can be measured at relatively low Re and then extrapolated via equation 1.7. Through this estimation, the performance degradation is observed

to be way less dramatic than previous works depicted. With a moderate amplitude of the StTW, a friction reduction higher than 20% can be obtained even at flight-Reynolds-numbers.

The vertical shift ΔB has been used in the past, in the context of simulations based on Reynolds-averaged-Navier-Stokes equations (RANS), to enforce the presence of roughness, by manipulating the boundary conditions of the employed turbulence model (Wilcox, 1998). A similar numerical strategy has been also used to simulate the presence of riblets (Aupoix, Pailhas, and Houdeville, 2012), leading to an estimate of the practical impact of using riblets via RANS-based simulations. Recently, Mele, Tognaccini, and Catalano (2016) used such a numerical strategy to model riblets over the external surface of a commercial transonic aircraft. They observed that friction reduction is not constant over the aircraft surface, and presents local values as large as 20%. The friction component of drag is reduced by around 11%, with total drag reduction of 4%. Riblets are observed to interact with the shock-wave, which is deflected downstream by the control and becomes more intense. This interaction induces a slight increase of pressure drag and a significant lift increase around 5%. When they compared the unactuated and the controlled aircraft at the same lift coefficient, they estimated a total drag reduction close to 10%, nearly doubling the expectation. This result, however, relies on RANS-based simulations where the effect of riblets is imposed via numerical modelling, and should be taken with a grain of salt. It suggests, however, that friction reduction interacts with the other components of forces significantly.

Results such as those obtained by Gatti and Quadrio (2016) and by Mele, Tognaccini, and Catalano (2016) open a glimpse of hope for the routine deployment of friction reduction techniques. Still, countless steps separate theory from the real world. The goal of this Thesis is to make a few steps along this direction and by investigating StTW we will try to answer to the question: what would be the true impact of a friction drag reduction technique when applied over the external surface of a commercial aircraft?

The numerical study of friction reduction is then extended to another flow control strategy based on blowing actuator. This study derives from my visiting experience at Harbin Institute of Technology in Shenzhen, China (HITSZ), where I had the opportunity to cooperate with Professor Zhou's team and to follow their experimental campaign of a relatively new concept of non-uniform blowing actuator.

The wall-normal injection of fluid is another drag-reducing option, studied since the mid of the 20th century (Mickley et al., 1954). In the past years, blowing and/or suction have been used in different configurations in order

to manipulate the flow field. Sumitani and Kasagi (1995) investigated uniform suction and uniform blowing via DNS inside a turbulent channel flow. They observed that blowing increases the near-wall turbulence and decreases friction, while suction induces the opposite effect. Park and Choi (1999) investigated via DNS of a turbulent boundary layer the effect of blowing applied over a spanwise slot, observing that friction reduction is followed by a mild overshooting. The same result has been confirmed by Pamiès et al. (2007). As already mentioned, Choi, Moin, and Kim (1994) achieved friction reduction via the opposition-control strategy; flow control with only blowing obtained a larger drag reduction than that with both blowing and suction. Kim and Sung (2003) studied via DNS the effect of a periodic blowing and observed that a steady actuator is more efficient than the unsteady one. By studying different forcing frequencies (Kim and Sung, 2006) observed that by increasing the jet's frequency, the efficiency of the steady case is recovered. Kametani et al. (2016) then investigated via Large Eddy Simulations (LES) the effect of streamwise spatially intermittent blowing, compared at constant mass injection. Friction is observed to be, on average, almost unaffected by the intermittency of the actuator, while the simplest uniform blowing is observed to be the most efficient in terms of net power savings. Stroh et al. (2016) went back to the uniform slot of constant blowing and observed that the overshooting downstream the control region is avoided when the streamwise extent of the actuator is sufficiently enlarged.

In this Thesis a relatively new concept of blowing actuator is numerically investigated in order to reproduce an ongoing experimental campaign at HITSZ where a spanwise non-uniform actuator is employed. This new blowing concept derives from the observation put forward by another experimental campaign conducted at HITSZ (Bai et al., 2014), where a spanwise-aligned array of piezo-ceramic actuators is employed to generate a transverse-travelling wave along the wall. Bai et al. (2014) measured a local friction reduction of 35% nearly 30 wall units downstream the actuator where they observed a vertical shift of the mean velocity profile of $\Delta B^+ \sim 4$. They put forward the hypothesis that a significant percentage of the measured friction reduction is due to a thin layer of highly regularised streamwise vortices located very close to the wall which interfere with the wall-cycle and contribute to reduce friction.

The same thin layer of highly regularised streamwise vortices is the main focus of the (yet unpublished) spanwise non-uniform blowing actuator that is being studied at HITSZ. They measured at the same downstream distance form the actuator, nearly 70% of friction reduction. They put forward the hypothesis that two different contributions produce the amount

of friction reduction obtained via non-uniform blowing. The first one is due to the wall-normal injection of null streamwise-momentum fluid; the second one is due to the layer of highly regularised streamwise vortices that interfere with the wall-cycle, as already observed by Bai et al. (2014). These hypotheses, however, require more in-depth analysis in order to be verified and to single out the impact of each contribution. Numerical simulations presented in this Thesis have been carried out to improve our understanding of the physical mechanisms at play.

Besides the study of friction manipulation, this Thesis also tackles another open problem that surrounds wall-shear stress: friction prediction, or, in other words, friction manipulation by shallow geometry changes. The problem of the flow field response to a smooth variation in bottom topography has been studied since the seminal work of Benjamin (1959) and still represents an open challenge.

When a smooth enough perturbation is employed at the wall, the response of the flow field is linear and the problem can be addressed in Fourier space (Charru, Andreotti, and Claudin, 2013). When the linearity condition is met, friction variation induced by the geometry change can be analytically predicted without the need of expensive numerical simulations. The Fourier-transformed friction perturbation, $\delta\tau = \tau/\tau_{flat} - 1$, where the subscript *flat* refers to the unperturbed flat wall, is therefore proportional to the Fourier-transformed wall slope via some complex transfer function \mathcal{T} . Recently, analytical expressions of the transfer function have been proposed by Luchini and Charru (2017) and Luchini and Charru (2019). Direct numerical simulations over curved wall of different shapes, in both laminar and turbulent regime have been performed in order to assess the accuracy of the proposed transfer functions.

1.5 Dissertation overview

The present dissertation is split into two sections. The main thread concerns the attempt to understand the potential impact of friction reduction on the aeronautical field is presented in the first part, whereas the second section describes our investigation on friction manipulation (via the blowing actuator) and prediction (via analytical transfer functions).

Part I. Towards drag reduction of a transonic transport aircraft

Chapter 2 presents a RANS-based preliminary work aimed to estimate the potential benefit of friction reduction strategies for a commercial airplane. The presence of StTW is enforced via modified wall-functions in order to

assess the achievable impact of friction reduction over complex geometries. The optimistic results observed by Mele, Tognaccini, and Catalano (2016) are confirmed in the present case, where StTW are applied. Both analyses, however, still rely on RANS-based simulations and numerical modelling of the friction reduction effects.

Motivated by the previous results, chapter 3 describes a first step made with proper and fully reliable tools. In the simple and well-known setting of an incompressible channel flow at low-Reynolds-number, a bump is introduced on the lower wall to study the effect of StTW over curved walls. Here, what is just suggested by previous RANS-based results becomes evident: modifying friction induces an effect on the pressure field that can bring extra benefits to the overall global power budget. RANS-based results presented in chapter 2, however, underline another fundamental aspect, which is absent in incompressible DNS: a key phenomenon is the interaction between shock waves and the friction reduction technique.

Transonic DNS simulations over a slab of a three-dimensional wing are thus presented, with and without StTW, in chapter 4. Here the interaction with the shock wave leads to a significant lift increase, with the consequent improvement of the wing performances. More in-depth investigations are, of course, needed in order to fully understand the physical mechanism beyond these effects and before taking them for granted. The present results, however, hint at a brighter future for friction reduction techniques in the aeronautical field.

Part II. Wall friction: manipulation and prediction

Another friction reduction technique is then investigated in chapter 5. Here numerical investigations aim to reproduce and enhance an on-going experimental research led by professor Yu Zhou at HITSZ. The work studies the effectiveness of a drag-reduction actuator, based on non-uniform and unsteady blowing, for spatially developing flows. The actuator is successfully described by our DNS, which perfectly captures the experimental measurements. A parametric investigation, however, suggests that the most efficient configuration is the (simpler) uniform and steady blowing.

In chapter 6, on the other hand, the problem of friction prediction over smoothly curved walls is assessed via comparison with numerical simulations. Here, the accuracy of the theory recently introduced by Luchini and Charru (2017) and Luchini and Charru (2019) is tested in both laminar and turbulent regime, and found to accurately predict friction even outside the linearity range.

1.6 Bibliography disclaimer

During the years of the doctoral research, snapshots of the work described in this Thesis have been presented at conferences and published in journals. In particular:

The research work described in chapter 2 has been presented in:

- A. Gadda, J. Banchetti, G. Romanelli, and M. Quadrio. “Drag reduction of a whole-aircraft configuration via spanwise forcing”. In: *16th EDRFCM, Monteporziocatone*. 2017

Work described in chapter 3 has been presented in a conference and published in a journal:

- J. Banchetti and M. Quadrio. “Turbulent drag reduction for a wall with a bump”. In: *European Turbulence Conference*, Turin, September 3–6 2019. 2019
- J. Banchetti, P. Luchini, and M. Quadrio. “Turbulent drag reduction over curved walls”. In: *J. Fluid Mech.* 896. (2020).

Work described in chapters 4 and 6 is contained in two journal papers which are now in preparation.

Part I

Towards drag reduction of a
transonic transport aircraft

CHAPTER 2

DRAG REDUCTION OF A WHOLE-AIRCRAFT CONFIGURATION

One coincidence is just a coincidence.

Two coincidences are a clue.

Three coincidences are a proof.

AGATHA CHRISTIE

THIS chapter aims to estimate the achievable impact of a friction drag reduction technique when applied over the external surface of a transport aircraft in transonic regime.

The global force budget is investigated via Reynolds-averaged-Navier-Stokes (RANS) simulations, performed with and without flow control. Friction drag reduction is achieved by applying streamwise-travelling waves of spanwise velocity (StTW); its effect on the mean velocity profile is modelled via modified wall-functions. The StTW is observed to influence the shock-wave position and to enhance both drag and lift of the transonic aircraft, thanks to indirect effects on pressure field.

The results reported in this chapter have already been presented by Gadda et al. (2017).

2.1 Introduction

Flow control represents an open challenge that could significantly influence the entire transport sector. Since our knowledge on the effectiveness of friction reduction systems at high-Reynolds-number (Re) and over complex geometry is still limited, their potential impact on practical applications is still uncertain.

The present work investigates the achievable impact of an active flow control technique, the streamwise-travelling waves of spanwise wall forcing (StTW), when applied over the external surface of a transport aircraft. The StTW, introduced by Quadrio, Ricco, and Viotti (2009), is known to yield significant energy savings when applied over flat walls at low-Reynolds-numbers.

Recently, Gatti and Quadrio (2016) observed that the vertical shift ΔB of the mean velocity profile, typical of rough walls (negative) and other friction reduction techniques (positive) like riblets (Choi, 1989), is produced by StTW too. Thanks to the Reynolds independence of the vertical shift when computed in wall units (ΔB^+), the achievable friction reduction over a plane channel at the desired Re can be analytically extrapolated. Through this link, they estimated that, at flight-Reynolds-numbers, a friction reduction higher than 20% can be obtained by applying StTW with moderate forcing amplitude.

In the context of Reynolds-averaged-Navier-Stokes simulations (RANS), it is possible to impose the vertical shift ΔB of the mean velocity profile by manipulating the boundary conditions of the employed turbulence model (Wilcox, 1998). Recently, Mele, Tognaccini, and Catalano (2016) used this numerical strategy to enforce the effect of riblets over the whole external surface of a transonic aircraft. They studied the NASA Common Research Model (CRM) in transonic regime with Mach number $M_\infty = 0.85$ and Reynolds number $Re_\infty = 5 \cdot 10^6$. They employed two different RANS solvers using the $k-\omega SST$ model in fully turbulent condition, obtaining a good agreement in the results. Even if riblets are known to reduce friction up to 10% (Walsh and Lindemann, 1984), they observed that friction reduction is not constant over the aircraft surface, and presents local values as large as 20%. The friction component of drag is reduced by around 11%, while the pressure component is slightly increased. The

combination of these two contributions leads to a total drag reduction of 4%.

However, the most interesting effect is the interaction between the controlled velocity profile and the shock-wave, located over the suction side of the wing, which is deferred downstream by riblets. Figure 2.1 plots the pressure coefficient over a wing section, with and without control, where the shock-wave is identified by the sharp recompression. This interaction induces a significant lift increase around 5%. When the two configurations (riblets off/on) are compared at the same lift coefficient, they observed a total drag reduction of 10%.

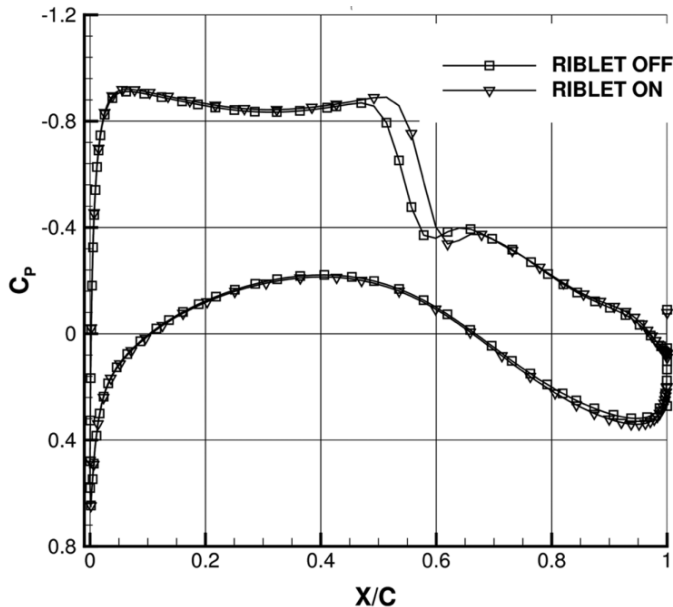


Figure 2.1: Comparison of the pressure coefficient, with and without riblets, over a wing section of the CRM aircraft. Here, x/c is the non-dimensional chord-wise coordinate and c_p is the pressure coefficient. Taken from Mele, Tognaccini, and Catalano (2016).

The preliminary work described in this chapter represents the motivation of this Thesis, and aims to estimate the achievable drag reduction when StTW is applied over the external surface of a transport aircraft. Moreover, it aims to verify how StTW interacts with the shock-wave and if the forcing positively interfere with other components of forces, as observed by Mele, Tognaccini, and Catalano (2016) even when a different setup is employed.

2.2 Simulations

Numerical simulations of the compressible Reynolds-averaged-Navier-Stokes equations are carried out for a whole-aircraft configuration in transonic regime.

The employed software is the general-purpose GPU-accelerated solver AeroX (Gadda et al., 2016). AeroX solves the RANS equations written in integral conservative form via the Cell-Centred Finite-Volume formulation, for a compressible, viscous and conductive fluid. Second-order centred flux accuracy is combined with the first order Roe's upwind flux; the blending strategy is automatically controlled by the Van Leer flux limiter. The viscous fluxes are assembled using a cell-limited Gauss algorithm for the evaluation of the velocity and temperature gradients. The pseudo-time advancement is performed via explicit Runge-Kutta schemes, employing local time step (LTS), along with multi-grid acceleration strategies.

The test case defined in the Second AIAA CFD Drag Prediction Workshop (Laflin et al., 2005) is considered to assess the impact of StTW on the aerodynamic forces. The considered aircraft is the complex wing-body configuration DLR-F6, specifically designed to check the capabilities of RANS solvers in the prediction of the flow around a typical aircraft, where both compressible and viscous effects are significant. Figure 2.2 portrays the studied aircraft configuration. In order to reduce computational effort,

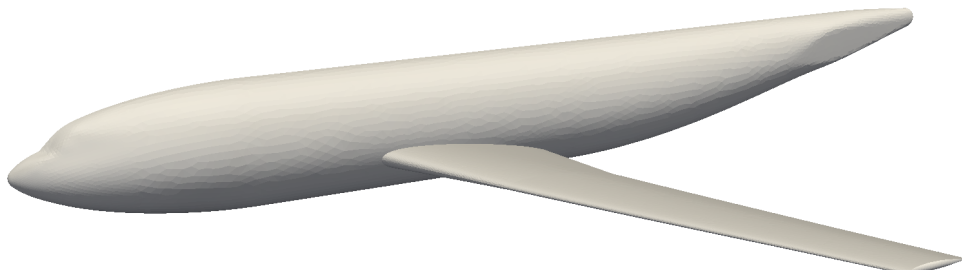


Figure 2.2: Wing-body configuration of the DLR-F6 aircraft.

only one half of the symmetric aircraft is studied. Both nacelles and

taileron have been removed, as well as windows and surface irregularities.

Simulations with and without actuation are carried out in transonic regime at Mach number $M_\infty = U_\infty/a_\infty = 0.75$ and Reynolds number $Re_\infty = U_\infty c_{ref}/\nu = 3 \cdot 10^6$. In the above definitions, c_{ref} is the wing reference chord, ν is the kinematic viscosity of the fluid, U_∞ is the free-stream velocity, whereas a_∞ represents the free-stream sound speed. In agreement with the workshop guidelines, a fully turbulent boundary layer is imposed over the external surface of the aircraft. The reference lift coefficient for the DLR-F6 is $C_\ell = 0.5$, obtained at a null angle of attack AoA in the uncontrolled case. The aerodynamic polar of the aircraft is studied via steady-state simulations, employing the Spalart–Allmaras turbulent model; for each angle of attack, two simulations are computed, with and without drag reduction.

The computational hybrid mesh, taken from the Second Drag Prediction Workshop website, is made by approximately $2 \cdot 10^6$ cells, composed by tetrahedrals (61%) and prisms (39%). The computational domain has dimensions of approximately $(L_x, L_y, L_z) = (42L_a, 17L_a, 17L_a)$ in the horizontal, spanwise and vertical directions respectively, where L_a is the aircraft length. Figure 2.3 portrays the sketch of the computational domain. Only one half of the aircraft is simulated, and over its middle plane,

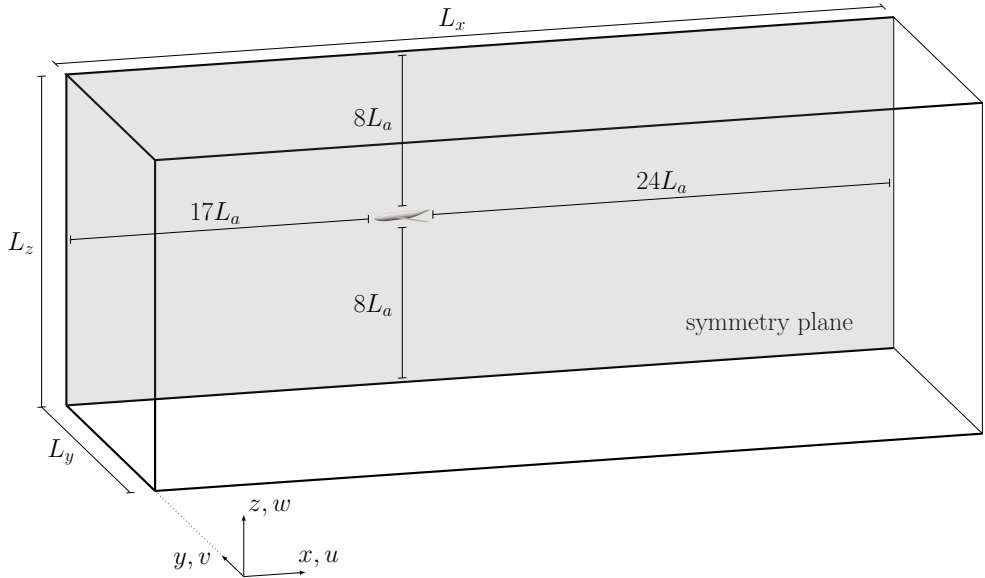


Figure 2.3: Sketch of the computational domain and the reference system. The aircraft is on the symmetry plane.

the symmetry boundary condition is applied. Far-field boundary condi-

tions are employed over the other edges of the domain. The boundary layer discretization is made to allow the use of wall-function boundary conditions over the aircraft surface and guarantees values of the first cell-size, expressed in wall units, always lower than 40. A validation of the employed setup has already been presented, for the uncontrolled case, by Gadda (2016).

Spanwise forcing is taken into account through modelling of its local effects via modified wall-functions. The wall-function is a type of wall treatment that avoids the expensive resolution up to the smallest turbulent scale, by imposing the law-of-the-wall around the solid body (Kalitzin et al., 2005). As observed by Gatti and Quadrio (2016), the spanwise-travelling waves produce an upward shift of the logarithmic portion of the mean velocity profile. The modified velocity profile imposed inside the wall-function implementation, mimics the drag reduction effects while avoiding the need for a detailed description of the small-scale, unsteady forcing technique. For simplicity, a constant vertical shift $\Delta B^+ = 5$ is imposed over the whole external surface of the aircraft, in order to reproduce the effect of moderate amplitude StTW. With the imposed velocity profile, the amount of extrapolated friction reduction at flight-Reynolds-numbers, following Gatti and Quadrio (2016), is around 23%. It is worth noticing that Mele, Tognaccini, and Catalano (2016) employed a finer mesh without the need of wall function boundary conditions. The drag reducing effect is therefore enforced by imposing a proper value of ω , the turbulence frequency, as a wall boundary condition of the $k - \omega$ SST turbulence model.

In the employed numerical manipulation, StTW is supposed to modify the mean velocity profile around the whole aircraft by the amount they would in a plane channel. This simplification ignores several phenomena that could drastically change the actuator's efficiency, like pressure gradient and/or curvature, transition and practical issues. The influence of non-uniform pressure gradient as well as wall curvature on friction reduction techniques is still almost unexplored due to measurements issues or prohibitive computational power required. Moreover, StTW is known to need a transitory distance to obtain its nominal value of friction reduction (Yudhistira and Skote, 2011), while the vertical shift is imposed everywhere, even on the aircraft nose. In addition, in this work, practical issues due to the installation of the actuator are completely neglected, and StTW is applied even over the aircraft windows.

Despite these simplifications this preliminary study provides an overview of the possible impact of StTW on the transport sector and motivates the present doctoral research. Moreover, a different numerical setup is employed to verify if the phenomena observed by Mele, Tognaccini, and

Catalano (2016) are case-dependent or rely on the interaction between friction drag reduction and shock-waves. To ease the comparison, table 2.1 reports the main differences between the two RANS-based works.

	Mele et al. (2016)	Present
Aircraft	NASA-CRM	DLR-F6
Re_∞	$5 \cdot 10^6$	$3 \cdot 10^6$
M_∞	0.85	0.75
Solver	UZEN / FLOWer	AeroX
Turbulence model	$k-\omega$ SST	Spalart-Allmaras
Friction reduction	Riblets	StTW
Forcing formulation	ω at the wall	ΔB in the wall-function

Table 2.1: Comparison of the simulation setup between Mele, Tognaccini, and Catalano (2016) and the present project.

2.3 Friction and pressure coefficients

In agreement with the Second Drag Prediction Workshop, contribution to forces are examined separately for friction and pressure: their local stresses are expressed by non-dimensional coefficients. The friction coefficient is

$$c_f(\mathbf{x}) = \frac{2\tau(\mathbf{x})}{\rho_\infty U_\infty^2}, \quad (2.1)$$

where ρ_∞ is the free-stream fluid density and $\tau = \mu \hat{\mathbf{t}} \cdot \partial \mathbf{u} / \partial n$, with $\hat{\mathbf{t}}$ the tangential unit vector, μ the viscosity of the fluid and $\partial / \partial n$ the derivative in wall-normal direction. The friction coefficient $c_f(\mathbf{x})$ is locally defined over the whole aircraft geometry. The pressure coefficient is

$$c_p(\mathbf{x}) = \frac{2(p(\mathbf{x}) - p_\infty)}{\rho_\infty U_\infty^2}, \quad (2.2)$$

where p_∞ is the free-stream pressure. In order to globally visualize stress distributions, figure 2.4 portrays in a compact view c_f and c_p over the upper side of the uncontrolled aircraft, for $AoA = 0$. Pressure increases over the aircraft nose and the leading edge of the wing. The supersonic bubble is detected over the suction side of the wing by the low-pressure area, where c_p shows values lower than -1 . This area ends with the shock-wave-related sharp recompression around one-quarter of chord downstream the leading edge. Over the fuselage, on the other hand, c_p presents almost negligible variations. Friction coefficient, portrayed on the left side of the picture, reaches the maximum values on the nose of the aircraft and over

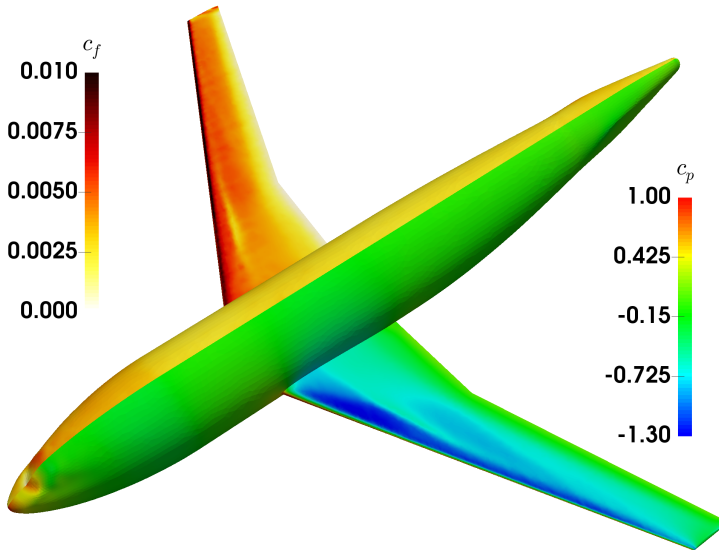


Figure 2.4: 3D view of the DLR-F6 configuration. Colour plot of the friction coefficient c_f (left) and the pressure coefficient c_p (right).

the suction side of the wing. Here, c_f sharply drops when the shock-wave occurs. Downstream the nose, friction remains nearly constant over the whole fuselage.

When StTW is applied, changes in friction and pressure are quantified by non-dimensional coefficients:

$$r(\mathbf{x}) = 1 - \frac{c_f(\mathbf{x})}{c_{f,0}(\mathbf{x})}; \quad \Delta p(\mathbf{x}) = 1 - \frac{c_p(\mathbf{x})}{c_{p,0}(\mathbf{x})}, \quad (2.3)$$

where subscript 0 is for the uncontrolled flow. Figure 2.5 portrays the distribution of r and Δp over the aircraft surface. Friction reduction is close to the expected value over almost the entire aircraft, with values of r ranging from 20% to 30%. A local maximum above 30% is reached on the aircraft nose, whereas significant variations can be appreciated over the suction side of the wing. Over the fuselage, downstream the nose, r presents nearly constant values, while Δp appears to be negligible. Over the upper wing, on the other hand, sharp variations are detected for Δp too.

This behaviour is further investigated in figure 2.6, where the pressure coefficient over a wing section, located at one third of the wing-span, is plotted for reference and controlled cases at $AoA = 0$. The streamwise

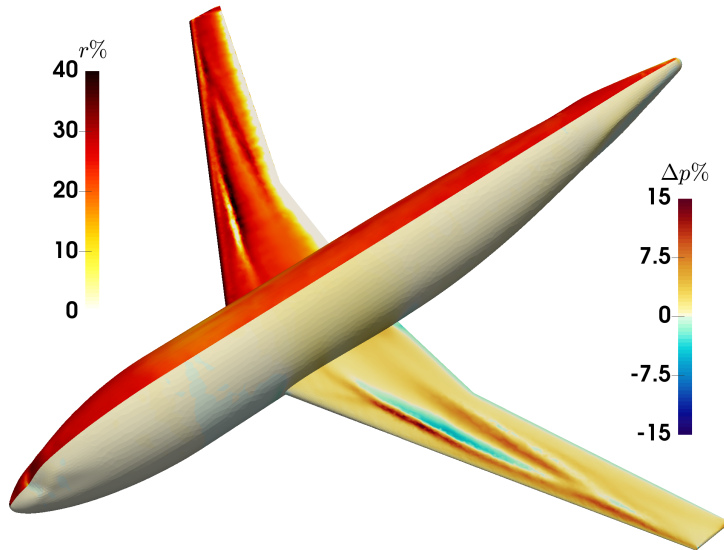


Figure 2.5: 3D view of the DLR-F6 configuration. Colour plot of the local friction reduction $r\%$ (left) and the local pressure reduction $\Delta p\%$ (right).

coordinate is made dimensionless by using the chord extent at this spanwise position c . In the reference case (red), a low-pressure area takes place

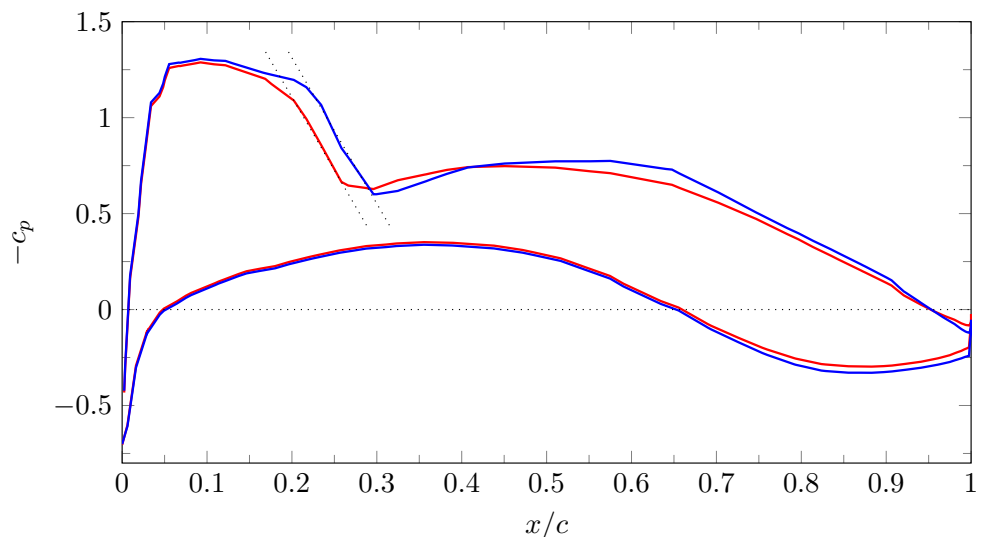


Figure 2.6: Comparison of pressure coefficient between reference (red) and controlled (blue) case over a wing section.

on the suction side downstream the leading edge, ending with the sharp recompression around $x/c = 0.25$ caused by the shock-wave. When StTW is applied (blue), the shock-wave is deferred downstream, in agreement with figure 2.1 (Mele, Tognaccini, and Catalano, 2016). A different position of shock-related recompression induces the sharp variations in both r and Δp over the suction side of the wing, observed in the context of figure 2.5. The agreement between the two RANS-based works hints that the interaction between friction reduction and the shock-wave position does not depend on the specific numerical implementation, and should be more in-depth investigated.

2.4 Aerodynamic forces

This project aims to understand whether the control-induced changes on the mean velocity profile, that StTW is known to produce over the indefinite plane wall, interacts with other components of the aerodynamic force. These indirect effects, that are not present in studies concerning simple geometries, are here singled out, by comparing drag changes induced by StTW with the 'extrapolated scenario', indicated with an (e) superscript. In this plot, StTW is assumed to simply reduce the friction component by 23%, the amount it would reduce in a plane channel at the employed Reynolds number, without interacting with the pressure field, supposed unchanged.

The overall drag coefficient C_d , accounting for both pressure and friction components, is shown in the first panel of figure 2.7. In the reference case (red), in the range of angles of attack considered, drag monotonically increases with AoA . When StTW is applied (blue), the behaviour of $C_d(AoA)$ is qualitatively similar, but quantitative changes are introduced. To quantify such changes, the total drag reduction ΔC_d is plotted in the lower panel. The computed drag reduction is above 20% at $AoA = -4$. However, ΔC_d is observed to significantly decrease with AoA , in such a way that the total drag of the aircraft is increased by StTW for $AoA > 2$. The extrapolated drag reduction (thin line with symbol), namely ΔC_d^e , shows a less steep slope, and it is higher than the computed one for $AoA > -1$.

A careful scrutiny of the two drag components due to friction and pressure, namely $C_{d,f}$ and $C_{d,p}$ respectively, is shown in the first panel of figure 2.8. In the reference case, friction drag (red line with circles) appears to be nearly constant, while pressure drag (red line with squares) drastically increases with AoA . Moreover, the friction component decreases with

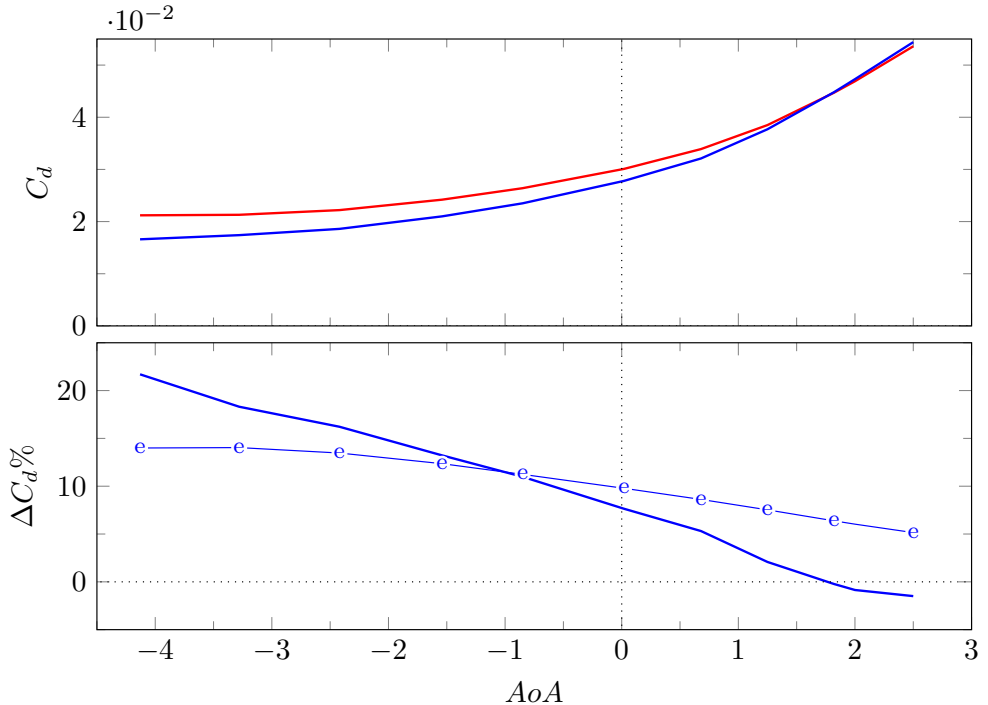


Figure 2.7: Comparison of drag coefficients as a function of AoA. First panel: reference (red) and controlled (blue) C_d ; second panel: computed $\Delta C_d\%$ (thick line) compared with the extrapolated one (thin line with symbols).

AoA and corresponds to 50% of the total drag for $AoA \sim -1$. With a decreasing impact of friction, the expected total drag reduction due to the friction reduction technique consequently diminishes, as observed in the lower panel of figure 2.7. The StTW induces quantitative changes in the friction drag (blue line with circles), and qualitatively affects the pressure drag (blue line with squares). The lower panel of figure 2.8 plots the spanwise forcing-induced relative changes on both drag components. The amount of friction reduction almost coincide with the expected amount of approximately 23%. Differently from the extrapolated scenario, pressure drag is strongly affected by StTW. The modified shock-wave position, observed in the context of figure 2.6, increases the extent of low-pressure area on the suction side of the wing, whose contribution to drag varies with AoA . Because of StTW, pressure drag reduction up to 20% is observed at low angles of attack. For $AoA > -1$, however, the drag component due to pressure significantly increases.

The delay of the shock-wave affects drag, as well as lift. Figure 2.9 plots the lift coefficient C_ℓ as a function of the angle of attack. In the reference case, lift is positive even at $AoA = -4$ and increases with constant slope

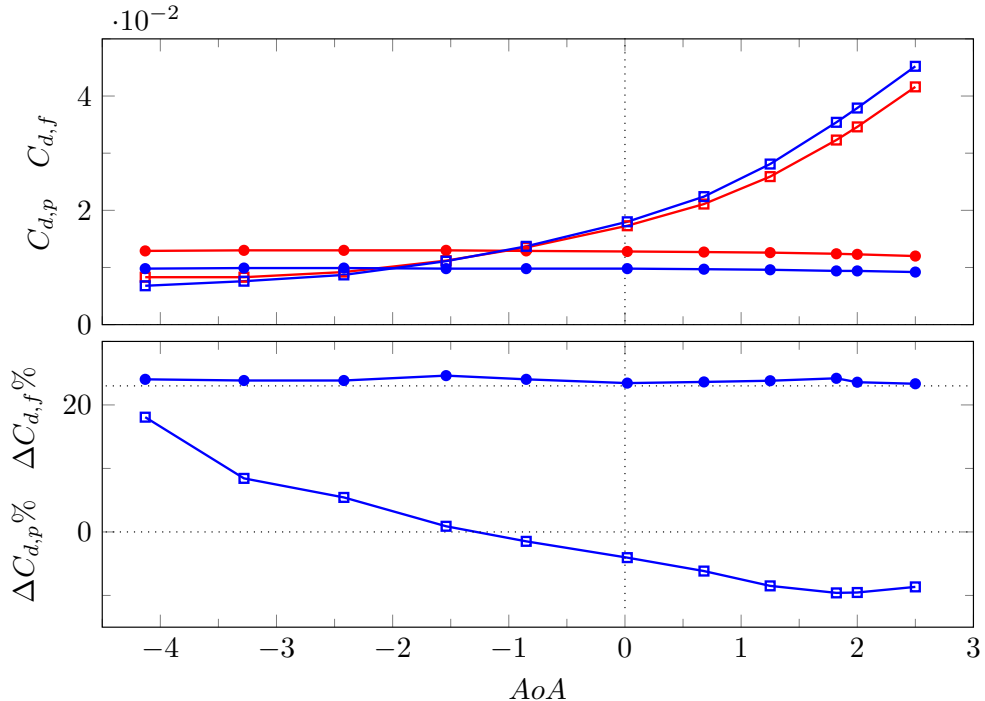


Figure 2.8: Pressure (lines with squares) and friction (lines with circles) drag components. Top: reference (red) and controlled (blue) cases; bottom: pressure and friction drag reduction $\Delta C_{d,p}$ and $\Delta C_{d,f}$, respectively.

up to $AoA = 2$, where the stall begins. The recompression delay due to StTW positively affects lift; C_ℓ is upward shifted, and the slope of the curve is slightly increased too. Moreover, the stall is observed to begin at the same angle of attack, but it occurs at higher lift coefficient.

Table 2.2 reports lift and drag coefficients, for both reference and controlled case at $AoA = 0$. The third column underlines the relative changes due to StTW.

	Ref	StTW	Δ	e
$C_{d,f}$	0.013	0.010	-23.4%	-23%
$C_{d,p}$	0.017	0.018	+4.0%	-
C_d	0.030	0.028	-7.6%	-10%
C_ℓ	0.52	0.57	+10.1%	-
L/D	17.5	20.9	+19.2%	+11.1%

Table 2.2: Force coefficients. Here, $C_{d,f}$ and $C_{d,p}$ are the friction and pressure components respectively, with $C_d = C_{d,f} + C_{d,p}$. C_ℓ is the lift coefficient, while L/D represents the lift/drag ratio.

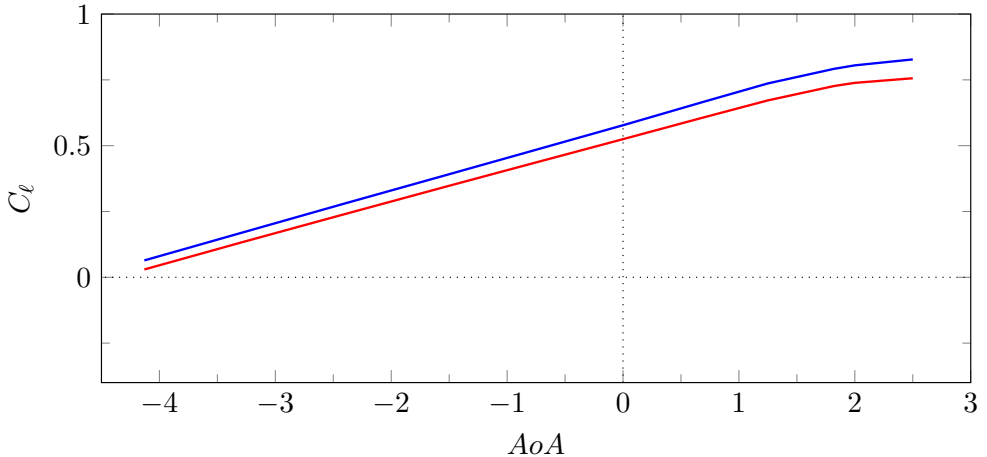


Figure 2.9: Comparison of lift coefficient, between reference (red) and controlled (blue) cases.

The StTW is observed to reduce friction drag by an amount of 23%, as expected. The influence of the wall-forcing over the suction side of the wing produces a relative pressure drag increase of 4%. The combination of the two components provide a total drag reduction around 8%. However, the most significant effect caused by the shock-delay is the substantial lift increase of 10%. The aircraft efficiency, defined by the lift/drag ratio L/D , is therefore increased by 19%. The fourth column, namely e , reports the extrapolated scenario. As observed in the context of figure 2.7, the extrapolated drag reduction is slightly higher than the computed one. Because of the significant increase of lift, however, the increase in lift/drag ratio due to StTW is nearly twice the extrapolated one.

Since C_ℓ actually is the main project requirement in aircraft design, drag coefficient is now compared at constant lift coefficient in figure 2.10. Differently from what figure 2.7 depicted, the StTW reduces drag for the entire range of lift coefficient considered. In addition, the total drag reduction, plotted in the lower panel, shows that changes due to StTW always overcome the extrapolated scenario by at least 5%. Overall, for the entire range of positive lift coefficient, drag reduction is higher than the extrapolated one with a relative increase of performance that spans from 40% at negligible lift, to 70% at $C_\ell = 0.6$. A sharp increase of ΔC_d , observed for $C_\ell > 0.6$, is due to the comparison between the reference aircraft, where the stall is already started, and the controlled case, where the stall begins at higher values of lift coefficient.

Moreover, the increase of L/D due to StTW strongly influences the aircraft range too. The range of an aircraft is usually described via the Breguet

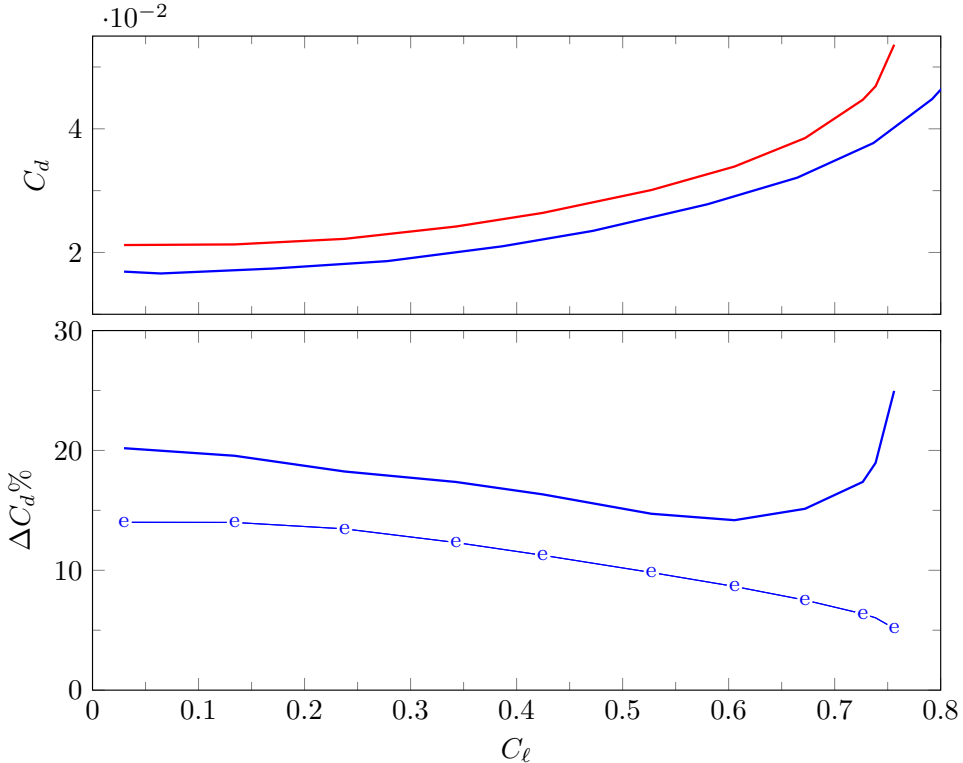


Figure 2.10: Comparison of drag coefficients as a function of C_l . Top reference (red) and controlled (blue) C_d ; bottom: computed $\Delta C_d \%$ compared with the extrapolated one (thin line with symbols).

Range Equation:

$$Range = \frac{U_\infty}{g SFC} \ln \left(\frac{\mathcal{W}_{initial}}{\mathcal{W}_{final}} \right) \frac{L}{D}, \quad (2.4)$$

where g is the gravitational constant, SFC is the specific fuel consumption of the engines, and $\mathcal{W}_{initial}$ and \mathcal{W}_{final} are the initial and final weight of the aircraft. In this context, the medium haul transonic model DLR-F6 can be compared with the Airbus A320, whose maximum range is 6300km (Airbus, 2020). By supposing a negligible impact of StTW in the aircraft weight, the increase of efficiency reported in table 2.2 linearly increases the aircraft range up to nearly 7500km.

2.5 Global power budget

The StTW, however, is an active flow control technique, and hence power consumption P_{req} should be taken into account in order to understand

the potential benefit in term of net power savings P_{net} . The actuation power is here estimated, since the numerical model employed to impose the presence of StTW does not allow a direct evaluation of P_{req} . Gatti and Quadrio (2016) estimated that inside a plane channel, P_{net} decreases with Reynolds number as fast as the power saved P_{sav} due to the friction reduction r , or at a slower rate. With this prediction, over a flat plate at flight-Reynolds number, the amount of P_{net} is around 10%. The amount of power required to generate the StTW is therefore estimated to be around 13% of the power spent due to friction drag. With this estimation, at the reference lift coefficient $C_\ell = 0.5$, the actuation power is lower than 6% of the power spent due to the total drag, since the friction drag is nearly the 43% of the total drag, as reported in table 2.2. The amount of net power savings is plotted in figure 2.11, and compared with the extrapolated behaviour. The net power savings is always higher than 10%, and it nearly doubles the theoretical prediction.

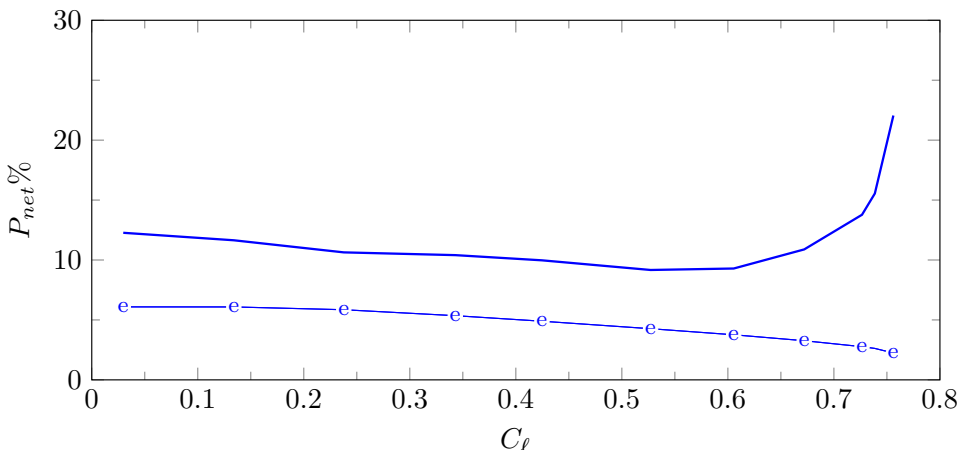


Figure 2.11: Net power savings as a function of C_ℓ : computed P_{net} compared with the extrapolated one (thin line with symbols).

Despite the differences in the setup of the two RANS-based works, the effects on the shock-wave position and the consequent increase of lift agree with Mele, Tognaccini, and Catalano (2016). Present results confirm that the direct effect of friction reduction strategies induces indirect changes in the pressure field, that drastically increase the aircraft performances.

2.6 Conclusions

The RANS-based simulations of a transonic whole-aircraft configuration have been carried out to understand how skin-friction drag reduction affects the overall aerodynamic forces. Several angles of attack are considered to study the aerodynamic polar of the two cases, without and with flow control. The effect of StTW is imposed via a modified wall boundary condition that reproduces the upward shift in the velocity profile over the external surface of the aircraft. The analysis on lift and drag leads to the same conclusions already put forward by Mele, Tognaccini, and Catalano (2016), despite the differences in the simulation setup. The friction reduction technique interacts with the pressure component of the aerodynamic force, enhancing the aircraft efficiency. Both works indicate that friction reduction techniques studied at low-Reynolds-numbers in planar geometries and incompressible flows might still conceal further significant benefits, that only appear in complex configurations. This study demonstrates that the direct effect of StTW on the velocity profile induces indirect changes on pressure field that affects the overall aerodynamic budget.

The study, however, makes a number of delicate assumptions that make doubting the final result legitimate. Indeed, the indirect way StTW are accounted for implies that the effect of pressure gradients and/or curvature, on the actuator's efficiency is neglected. Moreover, the imposed vertical shift is estimated from incompressible DNS data, without taking into account the effect of compressibility and the shock-wave boundary layer interaction is not explicitly resolved. In addition, in several areas of the aircraft, like the leading edge, the nominal efficiency of the actuator cannot be reached due to the required transition distance.

Despite these doubts, both RANS-based works hint that friction reduction techniques could induce game-changer effects, that usually tend to be ignored.

CHAPTER 3

TURBULENT DRAG REDUCTION OVER CURVED WALLS

Dream big, start small.
But most of all, START.

SIMON SINEK

T

HE work presented in this chapter studies the effects of skin-friction drag reduction in a turbulent flow over a curved wall, with a view to understanding the relationship between the reduction of friction and changes to the total aerodynamic drag. Direct numerical simulations (DNS) are carried out for an incompressible turbulent flow in a channel where one wall has a small bump; two bump geometries are considered, that produce mildly separated and attached flows. Friction drag reduction is achieved by applying streamwise-travelling waves of spanwise velocity (StTW).

The local friction reduction produced by the StTW is found to vary along the curved wall, leading to a global friction reduction that, for the cases studied, is up to 10% larger than that obtained in the plane-wall case. Moreover, the modified skin friction induces non-negligible changes of pres-

sure drag, which is favourably affected by StTW and globally reduces by up to 10%. The net power saving, accounting for the power required to create the StTW, is positive and, for the cases studied, is one half larger than the net saving of the planar case. The study suggests that reducing friction at the surface of a body of complex shape induces further effects, a simplistic evaluation of which might lead to underestimating the total drag reduction.

The results shown in this chapter have already been presented by Banchetti and Quadrio (2019) and published in a journal (Banchetti, Luchini, and Quadrio, 2020), which is here reported with minimal changes.

3.1 Introduction

Flow control aimed at reducing the skin-friction drag on a solid body immersed in a moving fluid is an active research area, motivated by its potential for significant energy savings and reduced emissions in the transport sector. Techniques for turbulent skin-friction drag reduction span from simple passive strategies to active approaches. The present work focuses on the latter group, since it generally produces larger effects which are easier to identify, and in particular considers the streamwise-travelling waves (StTW) of spanwise wall forcing, introduced by Quadrio, Ricco, and Viotti (2009), a technique capable of delivering substantial net savings.

The existing proofs of concept for skin-friction drag reduction are mostly limited to (i) low-Reynolds-number turbulent flows, and (ii) elementary geometries, such as flat plates and straight ducts. One naturally wonders whether the established benefits scale up when limitations (i) and (ii) are relaxed. Recently, limitation (i) has been shown not to hinder large drag reductions by spanwise forcing at high Re . For example Gatti and Quadrio (2016) estimated that a skin-friction reduction of around 23% is still possible with moderate-amplitude StTW at flight-Reynolds-number.

Owing to issue (ii), though, how to assess drag reduction in practical applications, often characterized by curved walls and/or non-uniform pressure gradients, remains an interesting open problem. For example, Atzori et al. (2018) recently applied drag reduction (via uniform blowing and body-force damping of near-wall turbulent fluctuations) to a finite wing slab studied by DNS/LES. Because of the complexity of the flow, however, the influence of curvature on the drag reduction effectiveness could not be singled out, as concurrent flow phenomena (like transition and separation) prevent a direct and quantitative comparison with flat-plate boundary layer or plane channel flow. Moreover, since transition was obtained by

tripping the flow shortly downstream of the leading edge, the actuation was applied in regions where the wall is almost flat.

The present work aims at understanding the interaction between skin-friction reduction (produced by StTW) and the overall aerodynamic drag in the simpler setting of a channel flow, where one wall has a bump. The turbulent flow over a plane wall with a bump has been considered several times in the past, both experimentally and numerically, as a representative case of wall-bounded flow with localized wall curvature. The experimental work by Almeida, Durao, and Heitor (1993) evolved into the ERCOFTAC C.18 and C.81 test cases, dealing with the flow over two-dimensional periodic hills (polynomial-shaped obstacles) with recirculation in their wake (Temmerman and Leschziner, 2001). Over the years, such geometry has been employed for validation of various numerical methods, LES subgrid models, and RANS simulations. Breuer et al. (2009) successfully compared the experimental information with results from two different DNS, one of which using the immersed-boundary method, and explored the effect of the Reynolds number. A periodic-hill experiment was designed by Rapp and Manhart (2011) to reproduce the configuration often used in numerical simulations, and Khaler, Scharnowski, and Cierpka (2016) used the same setup with high-resolution particle-image and particle-tracking velocimetry. Their results emphasized the importance of adequate near-wall spatial resolution in the surroundings of the bump. Wu and Squires (1998) studied with LES the adverse-pressure-gradient boundary layer created by a bump with a circular arc shape, in an attempt to reproduce the previous experimental study by Webster, Degraaff, and Eaton (1996). Their results showed that a coarse LES does not provide an entirely accurate description of the experimentally observed small-scale vortical structures in the near-wall region.

Marquillie, Laval, and Dolganov (2008), inspired by Bernard et al. (2003), designed a bump with a fore/aft asymmetry to qualitatively resemble an airfoil. They studied via DNS the budget equations for turbulent kinetic energy. A strong blockage is present in their case, where the flow almost separates over the upper flat wall; a long streamwise distance is required to recover the undisturbed conditions downstream of the bump. In a follow-up study, Marquillie, Ehrenstein, and Laval (2011) increased the value of the Reynolds number and extended the analysis to the vorticity and streaks dynamics, discussing the role of near-wall streaks in the kinetic energy production. More recently Mollicone et al. (2017) and Mollicone et al. (2018) returned to the arc-shaped symmetric bump to numerically study the process of turbulent separation. Different bulge geometries and Reynolds numbers were considered, and the production,

transfer and dissipation of turbulent kinetic energy were analysed via the generalized Kolmogorov equation. In Mollicone et al. (2019) a similar setup, with a smooth bump defined by a cosine function, was used to study particle-laden flows at finite values of the Stokes number.

The bump flow has also been used to investigate via numerical simulations the effectiveness of flow control applied over complex geometries. In particular, separation control has been addressed by Fournier et al. (2010) via pulsed and continuous jets, and by Yakeno et al. (2015) via plasma actuators. Active flow control is the background of the present chapter too. Aided by the simplicity of the bumped-wall geometry in the confined setting of a channel flow, we aim at understanding how the skin-friction drag reduction enforced by StTW alters the turbulent flow, its global aerodynamic loads and the power budget.

3.2 Simulations

The present work deals with a non-planar incompressible turbulent channel flow, studied via Direct Numerical Simulations (DNS). One of the channel walls is flat, and the other has a relatively small two-dimensional bump. Two bump profiles with the same height are considered, to produce an attached and a separated flow. Streamwise-travelling waves for the reduction of frictional drag are imposed at the lower non-planar wall, and their effect on the total drag is measured.

The DNS code, introduced by Luchini (2016), solves the incompressible Navier–Stokes equations written in primitive variables on a staggered Cartesian grid. Second-order finite differences are used in every direction. The momentum equations are advanced in time by a fractional time-stepping method using a third-order Runge–Kutta scheme. The Poisson equation for the pressure is solved by an iterative SOR algorithm. The non-planar wall is dealt with via an implicit immersed-boundary method, implemented in staggered variables to be continuous with respect to boundary crossing and numerically stable at all distances from the boundary (Luchini, 2013; Luchini, 2016).

The computational domain (a sketch is shown in figure 3.1, with the bump on the lower wall) is made by two streamwise-adjacent portions of similar length: the upstream volume with planar walls is streamwise-periodic, and feeds the downstream one where inflow and outflow conditions are used. Periodic conditions are used everywhere for the spanwise direction, and no-slip and no-penetration are enforced on the walls. The outflow

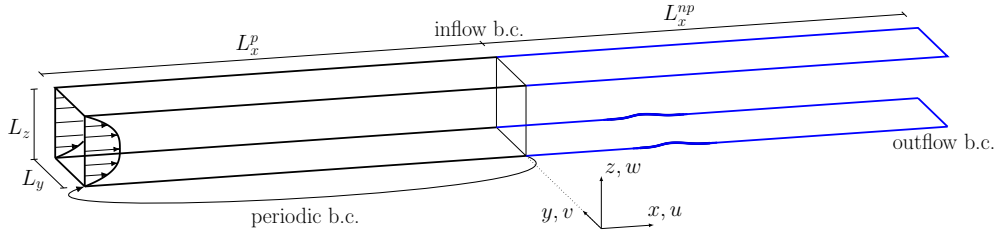


Figure 3.1: Sketch of the computational domain and the reference system. The bump is on the lower wall. The streamwise-periodic upstream domain (black) provides an inflow condition for the downstream one (blue).

condition extrapolates the velocity components according to:

$$\frac{\partial u_i}{\partial t} + U_c \frac{\partial u_i}{\partial x} = 0, \quad i = 1, 2, 3 \quad (3.1)$$

where $U_c(z)$ is the profile of the mean convection velocity of turbulent fluctuations defined as in Quadrio and Luchini (2003), and implemented as the mean velocity profile of the plane channel flow, modified in the near-wall region to have $U_c^+(z) \geq 10$. Alternative outflow conditions have been tested, finding negligible differences in the results.

The simulations are carried out at a bulk Reynolds number $Re_b = U_b h / \nu = 3173$ which in the reference case corresponds to a friction Reynolds number of $Re_\tau = u_\tau h / \nu = 200$ in the plane channel. In their definitions, ν is the kinematic viscosity of the fluid, the length scale is h , half the distance between the plane walls, whereas the velocity scale is the bulk velocity U_b in the former case and the friction velocity u_τ in the latter. Unless otherwise noted (e.g. with the plus notation indicating viscous units), in the following, quantities are made dimensionless with h and U_b .

The size of the computational domain is $(L_x^p + L_x^{np}, L_y, L_z) = (24.56, \pi, 2)$ in the streamwise, spanwise and wall-normal directions, respectively. The flat walls are placed at $z = 0$ and $z = 2$. The upstream periodic portion, with streamwise length of $L_x^p = 4\pi$, runs a standard channel flow DNS where the Constant Flow Rate (CFR) condition is imposed (Quadrio, Frohnapfel, and Hasegawa, 2016), and has a spatial resolution of $(n_x, n_y, n_z) = (360, 312, 241)$ discretization points. The downstream portion of the computational domain starts at $x = 0$ with a length of $L_x^{np} = 12$, over which 800 discretization points are non-uniformly distributed; grid and domain sizes in the spanwise and wall-normal directions are the same of the upstream domain, to avoid interpolation.

The grid is tuned for optimal use of computational resources while providing the necessary spatial resolution and smooth description of the bump

geometry via the immersed-boundary method. The spanwise grid spacing is uniform at $\Delta y = 0.01$; it corresponds to $\Delta y^+ = 2$ based on the inlet u_τ , and to $\Delta y^+ = 4$ close to the bump tip, where friction velocity is maximum. Streamwise resolution is uniform at $\Delta x = 0.04$ or $\Delta x^+ = 8$ in the periodic part, but increases as the bump is approached, reaching up to $\Delta x^+ = 2$ (based on local u_τ). The wall-normal spacing is neither constant in z nor symmetrical with respect to the centreline, since the bump is present on one wall only. A constant $\Delta z = 0.001$ is adopted from the lower wall to $z = h_b$, where h_b is the maximum bump height, and corresponds to $\Delta z^+ = 0.2$, based on the inlet u_τ . Then Δz gradually increases until, at the centreline, the maximum value of $\Delta z = 0.02$ is reached. The spacing then decreases again in the upper half of the channel, to reach $\Delta z = 0.004$ at the upper wall. Overall, the largest streamwise spacing is 6 times the local Kolmogorov length η , and the wall-normal and spanwise spacings are everywhere less than 2η . Near the bump the resolution is even higher; in the recirculation zone, the smallest dissipative scales are well resolved, with spacing in every direction equal to or lower than η .

The geometry of the bump, which is located on the lower wall, is two-dimensional and similar to the one considered by Marquillie, Laval, and Dolganov (2008), but with significantly smaller size, to reduce blockage and produce nearly undisturbed flow at the inlet and outlet sections. To enable reproducibility, the bump is analytically specified as the sum of two overlapping Gaussian curves, resulting in a smooth profile described by six parameters:

$$G_1(x) = a \exp \left[- \left(\frac{x - b}{c} \right)^2 \right] + a' \exp \left[- \left(\frac{x - b'}{c'} \right)^2 \right]. \quad (3.2)$$

The parameters values chosen for the geometry G_1 are $a = 0.0505$, $b = 4$, $c = 0.2922$ and $a' = 0.060425$, $b' = 4.36$, $c' = 0.3847$; they produce a bump with height $h_b = 0.0837$. A second geometry G_2 is identical to G_1 in the fore part up to the tip, but a streamwise expansion factor of 2.5 is applied to the rear part. Both G_1 and G_2 are shown in figure 3.2, with the former geometry producing a mildly separated flow, and the latter a fully attached flow.

In terms of computational procedures, after reaching statistical equilibrium flow statistics are accumulated over a simulation time of $T = 1000$. The time step is set at $\Delta t = 1.5 \cdot 10^{-3}$, corresponding to an average CFL number of approximately 0.5. Simulations are carried out with and without StTW for the reduction of skin friction. This specific drag reduction technique, introduced by Quadrio, Ricco, and Viotti (2009), has been

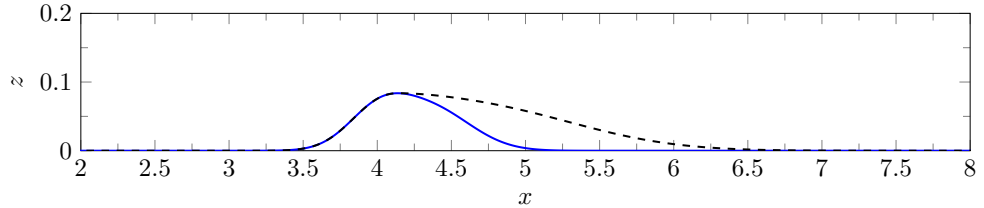


Figure 3.2: Bump geometries G_1 (blue line) and G_2 (black dashed line); they are identical up to the bump tip. Both have height of $h_b = 0.0837$ (only a portion of the streamwise extent is shown; note the enlarged vertical axis). G_1 leads to a mildly separated flow, while G_2 produces an attached flow.

selected because of its interesting energetic properties, its large effect on the turbulent friction and the availability of successful experimental implementations starting from Auteri et al. (2010). It should also be mentioned that a preliminary version of this project employed another spanwise forcing technique made by stationary waves, and the main findings were the same. The StTW is applied at the lower wall only, but including the periodic upstream part. The forcing translates into a non-homogeneous boundary condition for the spanwise velocity component at the wall as follows:

$$V_w(x, t) = A \sin(\kappa_x x - \omega t). \quad (3.3)$$

where V_w is the spanwise velocity at the wall, A is its maximum amplitude, and κ_x and ω represent the spatial and temporal frequencies of the wave. The wall forcing produces a sinusoidal distribution of spanwise velocity which travels in the streamwise direction. The numerical values of the forcing parameters are chosen, based on existing information (e.g. Gatti and Quadrio, 2016), to guarantee large amounts of skin-friction drag reduction in the plane channel. The selected values $A = 0.75$, which corresponds to $A^+ = 12$ when expressed in viscous units by using the inlet u_τ of the non-actuated case $\omega = \pi/10$ and $\kappa_x = 2$ yield 46% of drag reduction in a plane channel at $Re_\tau = 200$. Owing to the rather large actuator intensity, the total power budget is only mildly positive, with 11% of net power savings.

3.3 Instantaneous and mean flow fields

To begin with a qualitative picture of the flow, figure 3.3 portrays the appearance of turbulent vortical structures over the shorter bump G_1 , that will be the focus of this section. The figure is for the reference simulation without StTW, and plots isosurfaces of the intermediate eigen-

value λ_2^+ of the velocity gradient tensor (Jeong and Hussain, 1995), non-dimensionalised by using the inlet u_τ , and colour-coded with the coordinate z^+ . Even though the height of the bump is quite limited, the localized increase of turbulent activity immediately downstream of the bump is readily appreciated.

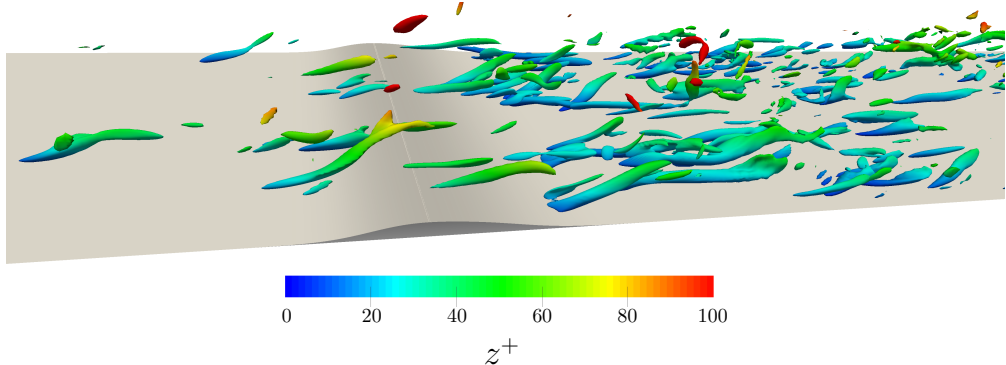


Figure 3.3: Isosurfaces of $\lambda_2^+ = -0.04$ for an instantaneous flow field in the reference case. Isosurfaces are colour-coded with the coordinate z .

Figures 3.4 and 3.5 show instantaneous colour plots of the streamwise and spanwise velocity components in the plane $z = 0.08$, which lies just below the bump tip, and corresponds to $z^+ = 16$ when expressed in viscous units by using the inlet u_τ of the non-actuated case. Every figure compares the flow with (bottom) and without (top) StTW; the white vertical band shows the intersection of the cut plane with the bump. In figure 3.4, the elongated streaks of high/low streamwise momentum are clearly visible for the reference simulation upstream of the bump and immediately downstream.

In the StTW case, by comparison, the overall velocity level is lower, and the range of fluctuations more limited overall, with a less evident streaky pattern. On the other hand, the streamwise modulation induced by StTW is noticed, particularly just upstream and downstream of the bump tip, where the distance between the wall and the cut plane is small.

In figure 3.5, the spanwise velocity over the same z plane is plotted. In the reference simulation the flow organization in turbulent structures can be appreciated, whereas a different picture emerges in the wall-forced case, where the spanwise forcing creates alternating bands of positive and negative spanwise velocity.

Moving on to the analysis of the mean flow field, for which the operator $\langle \cdot \rangle$ implies averaging over time and the homogeneous spanwise direction,

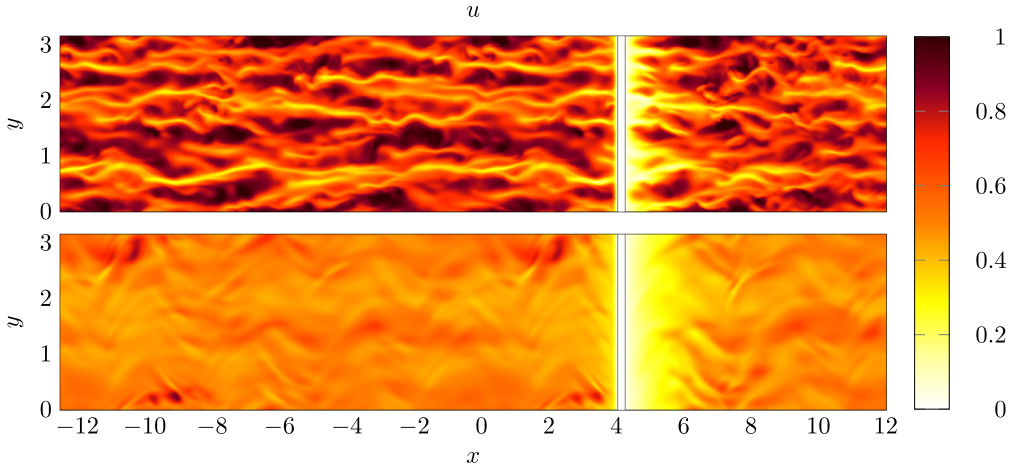


Figure 3.4: Colour plot of an instantaneous streamwise velocity field, in the plane $z = 0.08$ over the bump G_1 , for the reference case (top) and with $StTW$ (bottom). Flow is from left to right, and the upstream periodic section ends at $x = 0$.

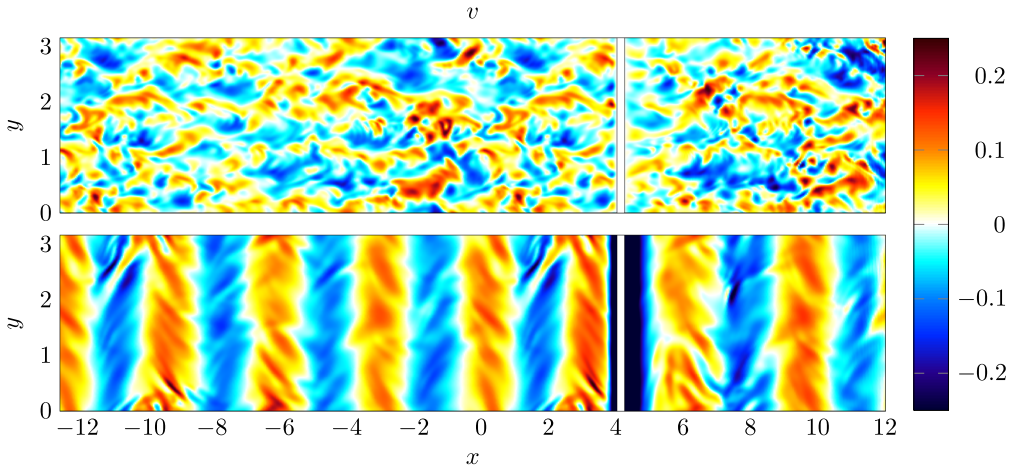


Figure 3.5: Colour plot of an instantaneous spanwise velocity field, in the plane $z = 0.08$ over the bump G_1 . Panels as in figure 3.4.

figure 3.6 plots a vertical plane with a colour map of the vertical velocity component $\langle w \rangle$, for a localized portion of the domain which includes the bump, namely $2.5 \leq x \leq 7$. The plot shows that the peak of w just ahead of the bump is decreased because of $StTW$. The thick contour line corresponds to $\langle u \rangle = 0$ and visualizes the separated region with a recirculation bubble after the bump; the separated region is very small for the reference case with G_1 , but the wall forcing somewhat increases its extension.

The mean pressure distribution $\langle p \rangle$ is shown in figure 3.7; to ease comparison, the pressure levels of the two cases are offset such that they coincide

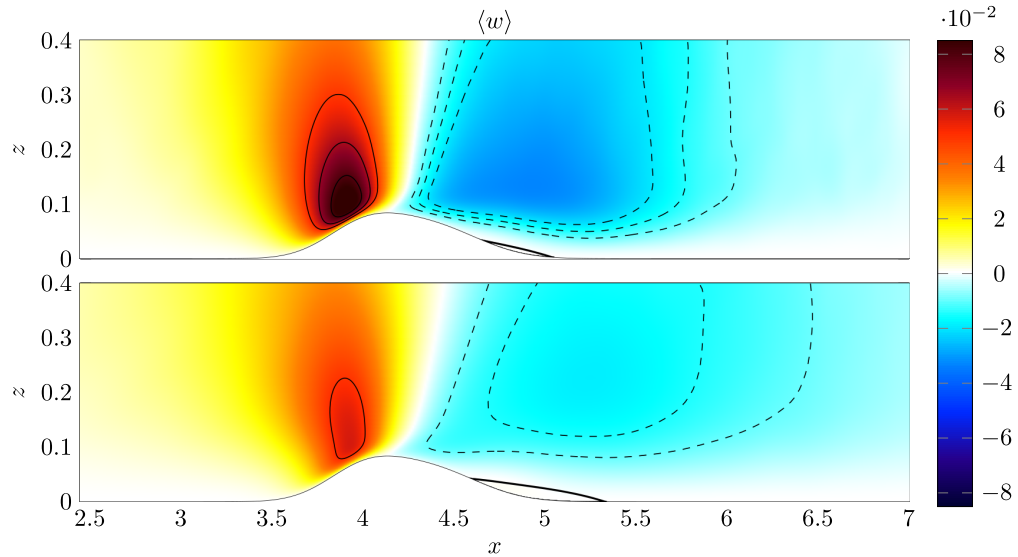


Figure 3.6: Colour plot of the mean vertical velocity $\langle w \rangle$ for the bump G_1 : top, reference case; bottom, StTW. Positive contours (continuous lines) are drawn for $\langle w \rangle = (0.05, 0.065, 0.08)$, and negative contours (dashed lines) are drawn for $\langle w \rangle = (-0.02, -0.015, -0.01)$. The thick black line indicates $\langle u \rangle = 0$ and marks the boundary of the separated region.

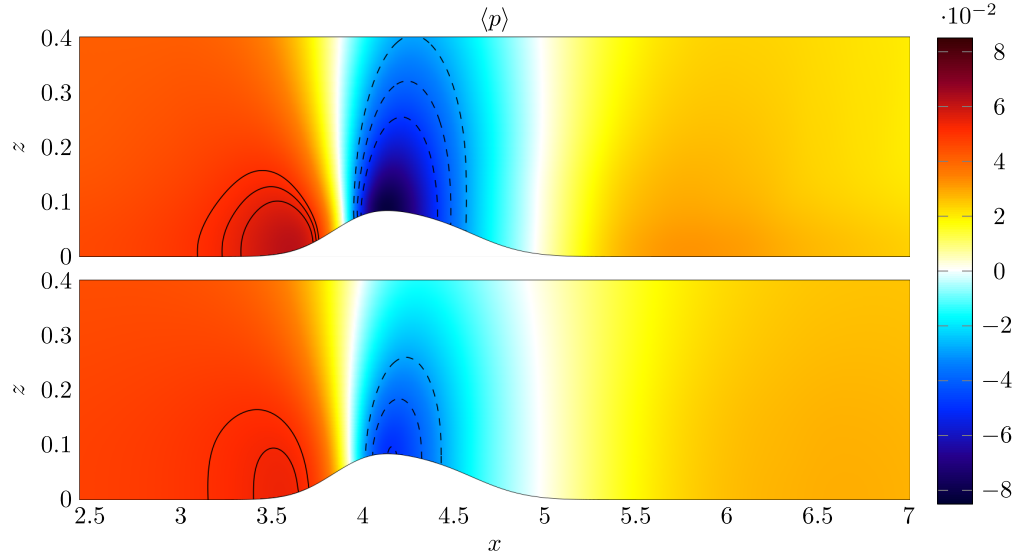


Figure 3.7: Colour map of the mean pressure $\langle p \rangle$ for the bump G_1 : top, reference case; bottom, StTW. Positive contours (continuous lines) are drawn for $\langle p \rangle = (0.05, 0.0525, 0.055)$, and negative contours (dashed lines) are drawn for $\langle p \rangle = (-0.05, -0.04, -0.03)$.

at $x = 0$. Pressure locally increases over the anterior part of the bump, while a local minimum appears shortly after the tip because of the negative wall curvature. In the StTW case, the local maximum before the bump is decreased, and similarly the local minimum at the bump tip shows lesser intensity.

3.4 Skin friction and pressure at the wall

The aerodynamic force includes contributions from friction and pressure. Friction and pressure at the wall are often expressed by local dimensionless coefficients, although their integral contribution is not straightforwardly related to the drag force. The friction coefficient is

$$c_f(x) = \frac{2\langle\tau\rangle(x)}{\rho U_b^2}, \quad (3.4)$$

and the pressure coefficient is

$$c_p(x) = \frac{2\langle p \rangle(x)}{\rho U_b^2}. \quad (3.5)$$

In definition (3.4), ρ is the fluid density and $\tau = \mu \hat{\mathbf{t}} \cdot \partial \mathbf{u} / \partial n$, with μ the viscosity of the fluid, $\hat{\mathbf{t}}$ the tangential unit vector and $\partial / \partial n$ the derivative in wall-normal direction. In definition (3.5), the pressure value $p(x)$, which can be arbitrarily shifted in an incompressible flow, is set to have $\langle p \rangle = 0$ at the outlet section.

The quantity $c_f(x)$ is considered in figure 3.8 for the reference and controlled cases. Only the lower wall of the non-periodic portion $0 \leq x \leq 12$ of the computational domain is shown. Indeed, the presence of the bump is felt on the c_f distribution at the opposite wall too; however, owing to the small blockage this effect is minimal and therefore not shown here. The top panel plots the distribution of $c_f(x)$ itself, comparing the reference and the actuated flows for the bump G_1 . In the reference simulation the friction coefficient decreases just before the bump, and then quickly grows to reach its maximum close to the bump tip. The maximum value is approximately 3 times that of the flat wall. Downstream of the tip, c_f quickly drops towards zero. The flow separation (already discussed in figure 3.6), produces a locally negative c_f . After reattachment the friction distribution presents a mild overshooting, followed by a slow recovery towards the undisturbed planar-wall value. When StTW is applied, the behaviour of $c_f(x)$ is qualitatively similar, but quantitative changes are introduced, as friction is reduced everywhere by StTW. To quantify such

changes, a local skin-friction reduction rate $r(x)$ is plotted in the lower panel for both bumps. Here, r is defined as the relative change of $c_f(x)$ between the controlled and the reference flow:

$$r(x) = 1 - \frac{c_f(x)}{c_{f,0}(x)}, \quad (3.6)$$

where $c_{f,0}(x)$ is for the reference flow. Way upstream of the bump G_1 , where the wall is flat, r equals the value typical of StTW in the indefinite plane channel flow, namely $r = 46\%$ at the present Re and for the employed parameter values (see for example Gatti and Quadrio, 2016). When the bump is approached, r at first increases slightly above 50%

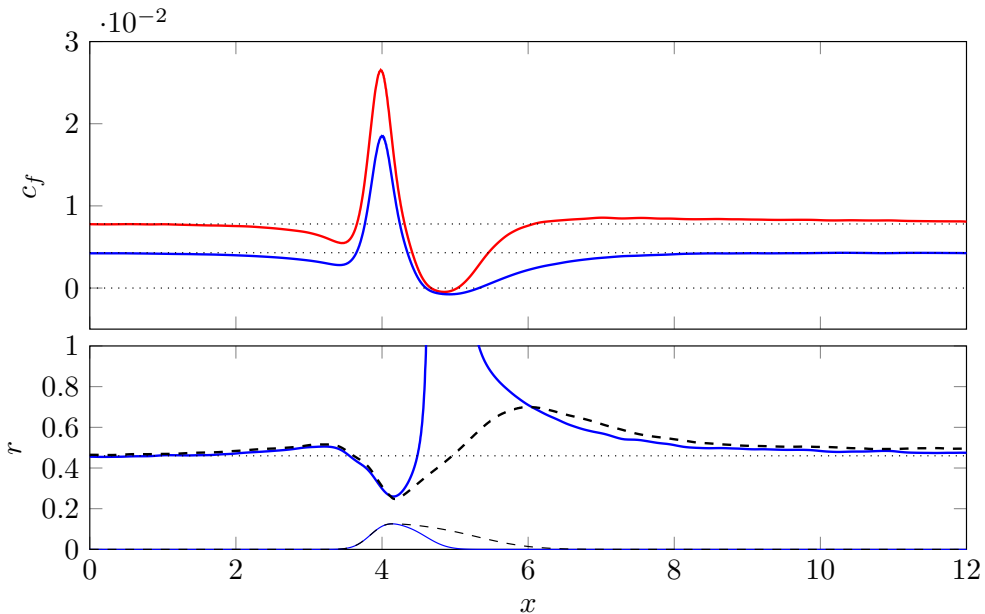


Figure 3.8: Skin-friction distribution $c_f(x)$ over the wall with the bump. Top: comparison between the reference case (red) and the controlled case (blue) for bump G_1 . Bottom: local skin-friction reduction rate $r(x)$ for G_1 (blue) and G_2 (black dashed). The thin profiles at the bottom of the plots draw the two bumps, in arbitrary vertical units.

immediately upstream of the bump, and then decreases to 25% over the anterior part of the bump. After the tip, when flow separation takes place, the quantity r becomes meaningless; for example, the extrema of the separation bubble in the unforced case, identified by the zero points for $c_{f,0}$, correspond to points where r diverges to infinity. There StTW is observed to cause an increase of both intensity and length of the separation bubble. After the reattachment point, differently from the reference case, no overshooting occurs for friction over StTW.

The longer bump G_2 , though very similar, does not lead to flow separation. Here r (black dashed line) is nearly identical to that for G_1 up to the bump tip, and then increases towards a local maximum of 70% near $x = 6$. Once again, the recovery towards the planar-wall value is quite slow, and the local drag reduction remains higher than the planar value in most of the computational domain after the bump tip.

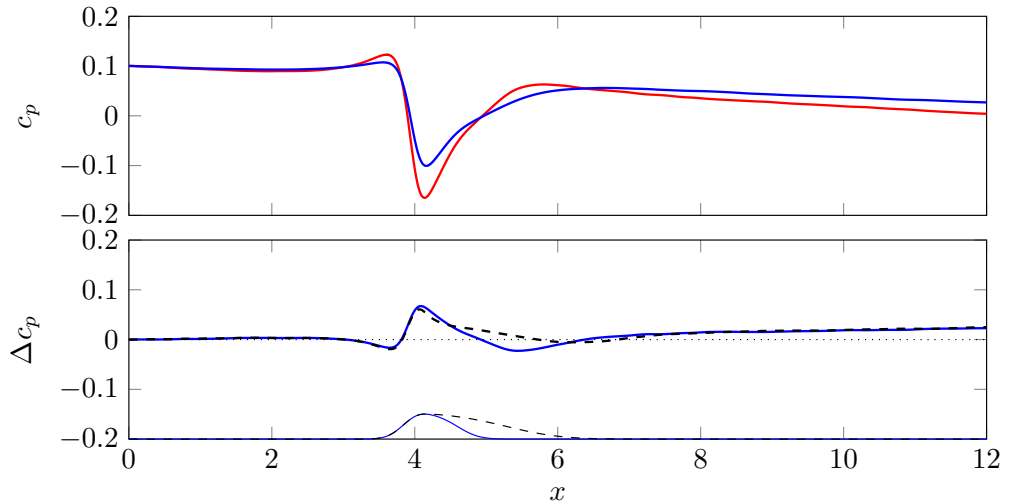


Figure 3.9: Pressure distribution $c_p(x)$ over the wall with the bump. Top: comparison between the reference case (red) and the controlled case (blue) for bump G_1 . Bottom: local difference between pressure coefficients $\Delta c_p(x) = c_p(x) - c_{p,0}(x)$ for G_1 (blue) and G_2 (black dashed). The thin profiles at the bottom of the plots draw the two bumps, in arbitrary vertical units.

Figure 3.9 plots the streamwise distribution of $c_p(x)$; the pressure levels of the two cases, which by definition coincide at the outlet section where the mean pressure is set at zero, have been adjusted such that they coincide at $x = 0$ instead, as done already in figure 3.7. In the reference case, the local pressure increases before the bump, and so does the pressure coefficient. An evident minimum of c_p is reached at the bump tip, followed by a relatively fast recompression. In the inlet and outlet portions of the computational domain, i.e. far enough from the bump, $c_p(x)$ presents the linear decrease (i.e. uniform mean pressure gradient) that is expected for a plane channel flow. As already commented upon for c_f , the bump affects the pressure coefficient on the opposite planar wall too, but this is not shown here as the changes are minimal.

The action of StTW at the inlet, where the local drag is friction-dominated, simply translates into a milder negative slope of the $c_p(x)$ curve, owing to the lower friction drag. More downstream, the positive pressure peak

before the bump is noticeably reduced by StTW, thus anticipating that the pressure drag contribution associated to the anterior part of the bump will be reduced (see later 3.4.2.2). The minimum of c_p near the bump tip is also decreased by StTW, so that the pressure jump between the two local extrema is reduced by around 20%. After the bump, say for $x > 7$, the flow is not affected by the presence of the bump, and again only a reduced pressure gradient is visible.

In order to quantify changes in pressure distribution due to StTW, a local pressure reduction rate, in analogy with friction, cannot be used; in incompressible flows, pressure values can be shifted by a constant, making a ratio meaningless. For this reason we simply study the difference introduced by StTW as

$$\Delta c_p(x) = c_p(x) - c_{p,0}(x). \quad (3.7)$$

Figure 3.9 (bottom panel) plots $\Delta c_p(x)$ for both geometries showing a very similar behaviour; the two curves almost coincide up to the bump tip, then for G_2 the milder slope in the aft part creates a slower recompression. The agreement of $\Delta c_p(x)$ up to the bump tip for the two geometries indicates that the effect of StTW on the pressure distribution is not dictated by the presence of a separation bubble.

3.4.1 Drag coefficients

To assess how StTW interacts with the curved wall, simply comparing the drag force per unit area between the plane geometry and the one with the bump is not the best choice, because the bump introduces concentrated losses. In fact, in the limit of very large streamwise extent L_x^{np} of the computational domain that includes the bump, concentrated losses become negligible and the same drag of the planar case is obtained.

Drag is usually quantified in two ways. The first one, meant to evaluate distributed losses C_d^d , uses the streamwise length of the domain under consideration as the reference length, and leads to the definitions below for friction and pressure contributions:

$$C_{d,f}^d = \frac{2}{\rho U_b^2 L_x} \hat{\mathbf{x}} \cdot \int_0^{L_x} \mu (\nabla \mathbf{u} + \nabla \mathbf{u}^T) \cdot \mathbf{n} \, d\ell; \\ C_{d,p}^d = \frac{2}{\rho U_b^2 L_x} \hat{\mathbf{x}} \cdot \int_0^{L_x} \langle p \rangle \mathbf{n} \, d\ell, \quad (3.8)$$

where $\hat{\mathbf{x}}$ is the unit vector in the x direction. Obviously, in the flat channel only the friction contribution is present. (In the above definitions, note the

use of capital letters to indicate global force coefficients, whereas lowercase was used above for local coefficients.)

To evaluate concentrated losses C_d^c , on the other hand, the obstacle contribution to drag is singled out computing the drag variation with respect to the planar case. Using the frontal area of the obstacle as a reference surface, or in this case the bump height h_b , which is nearly 140 times smaller than L_x^{np} , as the reference length, C_d^c becomes independent from the domain length:

$$C_{d,f}^c = \frac{L_x^{np}}{h_b} \left(\tilde{C}_{d,f}^d - \bar{C}_{d,f}^d \right); \quad C_{d,p}^c = \frac{L_x^{np}}{h_b} \left(\tilde{C}_{d,p}^d - \bar{C}_{d,p}^d \right), \quad (3.9)$$

where \tilde{C}_d^d and \bar{C}_d^d indicate drag coefficients computed for the non-planar and planar wall, respectively. Obviously, when concentrated losses C_d^c are evaluated for the controlled case, both \tilde{C}_d^d and \bar{C}_d^d are computed in presence of StTW.

In table 3.1, drag coefficients are reported for the bump G_1 , computed over the lower wall only. Distributed losses are evaluated in the flat periodic domain while concentrated losses are computed in the non-periodic domain that includes the bump. In the planar case StTW reduce friction drag by 46%, as expected, and no pressure drag is present. The friction component of the concentrated losses due to the bump is globally nearly zero in the reference case, implying that the friction coefficient computed over the entire wall with the bump almost coincides with that over the flat wall. This is non-obvious, as the bump has been observed (cf. Figure 3.8) to introduce significant local variations. The pressure component, on the other hand, generates a considerable additional contribution to drag.

	Distributed losses			Concentrated losses		
	Ref	StTW	Δ	Ref	StTW	Δ
$C_{d,f} \times 10^{-2}$	0.777	0.424	-45.5%	-0.004	-4.671	
$C_{d,p} \times 10^{-2}$	0	0	0	9.891	8.887	-10.3%
$C_d \times 10^{-2}$	0.777	0.424	-45.5%	9.887	4.197	-57.5%

Table 3.1: Drag coefficients for the bump G_1 . Here $C_{d,f}$ and $C_{d,p}$ are the friction and pressure components respectively, with $C_d = C_{d,f} + C_{d,p}$. Distributed losses are computed according to Eq. (3.8) in the planar geometry while concentrated losses introduced by the bump are evaluated via Eq.(3.9). Figures are for the lower wall only.

When StTW is applied, concentrated friction losses become negative, implying that the mean friction over the wall with the bump is lower than the friction over a controlled plane wall. This benefit, absent without flow

	Distributed losses			Concentrated losses		
	Ref	StTW	Δ	Ref	StTW	Δ
$C_{d,f} \times 10^{-2}$	0.781	0.418	-46.5%	-0.158	-2.904	
$C_{d,p} \times 10^{-2}$	0	0	0	7.083	6.843	-3.4%
$C_d \times 10^{-2}$	0.781	0.418	-46.5%	6.925	3.940	-43.1%

Table 3.2: Drag coefficients for the bump G_2 .

control, is due to the slower downstream recovery of friction to its planar value and the lack of overshooting after the bump, as shown in figure 3.8. However, quantifying this benefit in terms of the percentage change of $C_{d,f}^e$ (not shown in table 3.1) would be meaningless, since the reference value is close to zero. The bump is responsible for a considerable pressure drag, and it is interesting to observe that StTW reduces this component too, by an amount of approximately 10%. Overall, control by StTW leads to reduction of total concentrated losses by around 57%.

Table 3.2 provides the same quantities for the milder bump G_2 . The distributed losses in the planar case are obviously the same as G_1 (the small difference is attributed to the finite averaging time). Since G_2 is less steep after the tip, the concentrated losses decrease. The concentrated friction losses are clearly negative; pressure recovery is more effective and thus pressure losses are lower in both reference and controlled case. The presence of StTW also induces a pressure drag reduction, which is, however, less pronounced than in G_1 . The overall outcome is a reduction of approximately 43% in the concentrated losses.

It is noted explicitly that the reduction of concentrated losses reported in the rightmost column of tables 3.1 and 3.2 must be added to the distributed drag reduction to assess the global saving. This is discussed in the following paragraph.

3.4.2 Changes in friction and pressure drag over the curved wall

Drag changes induced by StTW are now assessed against the scenario in which StTW is assumed to simply reduce the friction component by the amount they would in a plane channel. We name this the "extrapolated amount", and indicate it with an (e) superscript.

The simulation for G_1 shows that the friction drag over the entire non-periodic portion is 92% of the overall drag. Combining changes in distributed and concentrated losses, StTW reduces friction drag by 49.6%, i.e. approximately 4% more than the planar case. The pressure drag,

representing 8% of the total drag, is reduced by a relative 10.3%. Bump G_2 , albeit separation-free, shows a similar behaviour. With friction drag accounting for 94% of the total, StTW reduces friction component by 3% more than the planar value, and the pressure component, too, is reduced by a further 3%.

A physical explanation of the interrelation between friction and pressure drag reduction requires quantifying the influence of local stresses on the global drag budget. A local drag reduction coefficient $\Delta c_d(x)$ is defined as the difference of local contributions to drag coefficients, i.e. the integrands in Eqns.(3.8), between the reference and the controlled case:

$$\Delta c_d(x) = c_{d,0}(x) - c_d(x), \quad (3.10)$$

where the subscript 0 indicates the reference case. It should be noted that a sign inversion is adopted here in comparison to Eq. (3.7), for drag benefits to yield positive $\Delta c_d(x)$. To weigh the local contribution on the integral budget, a global drag reduction rate $R(x)$ is further introduced as in Stroh et al. (2016): $R(x)$ is defined as the integral of $\Delta c_d(x)$ up to location x , expressed as a percentage of the drag calculated over the entire domain in the reference case:

$$R(x) = \frac{\int_0^x \Delta c_d(x') dx'}{\int_0^{L_x} c_{d,0}(x') dx'}. \quad (3.11)$$

3.4.2.1 Friction drag reduction

The friction component of Δc_d , namely $\Delta c_{d,f}$, is plotted in the upper panel of figure 3.10, together with the extrapolated value $\Delta c_{d,f}^{(e)}$ obtained by assuming that the planar friction reduction rate carries over to the non-planar geometry G_1 . Obviously, the two curves tend to coincide far from the bump, while immediately upstream and over a large downstream extent the true friction drag reduction is larger than the extrapolated one. On the other hand, over the anterior part of the bump, where r in figure 3.8 shows a local minimum, the true friction drag reduction is smaller than $\Delta c_{d,f}^{(e)}$.

To understand which area is specifically responsible for the extra friction drag reduction, the local difference between actual and extrapolated values is shown in the center panel of figure 3.10, for both bump geometries, to demonstrate that the qualitative behaviour is the same, regardless of the presence of flow separation. The two curves coincide, as expected, at the inlet and in the fore part of the bump, whereas the lack of separation in G_2 makes the two curves quantitatively differ in the decelerating region

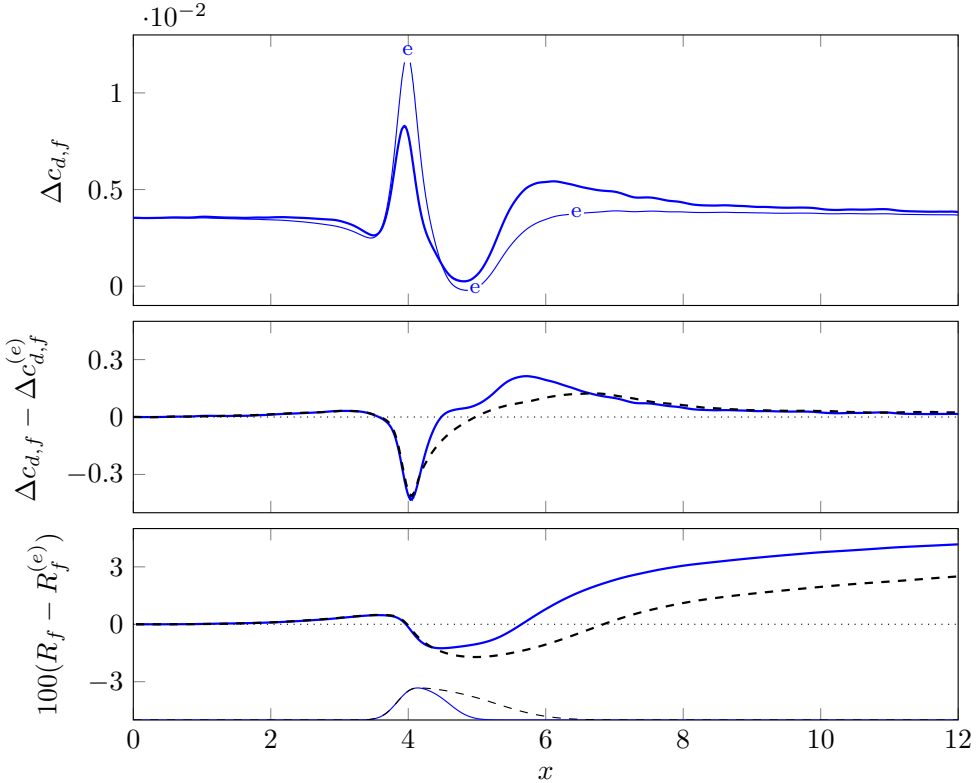


Figure 3.10: Changes in the skin-friction component of the total drag. Top: the computed $\Delta c_{d,f}$ (thick line) compared with the extrapolated $\Delta c_{d,f}^{(e)}$ (thin line with labels) for bump G_1 . Center: difference between computed and extrapolated friction drag reduction, for geometries G_1 (blue line) and G_2 (black dashed line). Bottom: difference between actual R_f and extrapolated integral budget $R_f^{(e)}$ for both geometries. The thin profiles at the bottom of the plot draw the two bumps, in arbitrary vertical units.

after the bump tip. The integral budget R_f , i.e. the friction component of the integrated drag reduction introduced by Eq.(3.11), is plotted in the lower panel of figure 3.10 as a difference with respect to the extrapolated value $R_f^{(e)}$. For both bumps, the larger friction drag reduction after the bump tip, and its slower recovery of the planar value, already discussed in the context of figure 3.8, translate into a global friction drag reduction approximately 3% larger than the value extrapolated from the planar case.

Figure 3.11 links the differences in friction drag reduction observed after the bump tip, including where the wall is flat again, to the distribution of the turbulent kinetic energy $k = 1/2\langle u'_i u'_i \rangle$. Its production P is shown later in figure 3.12. It is worth mentioning that the fluctuating velocity field u'_i

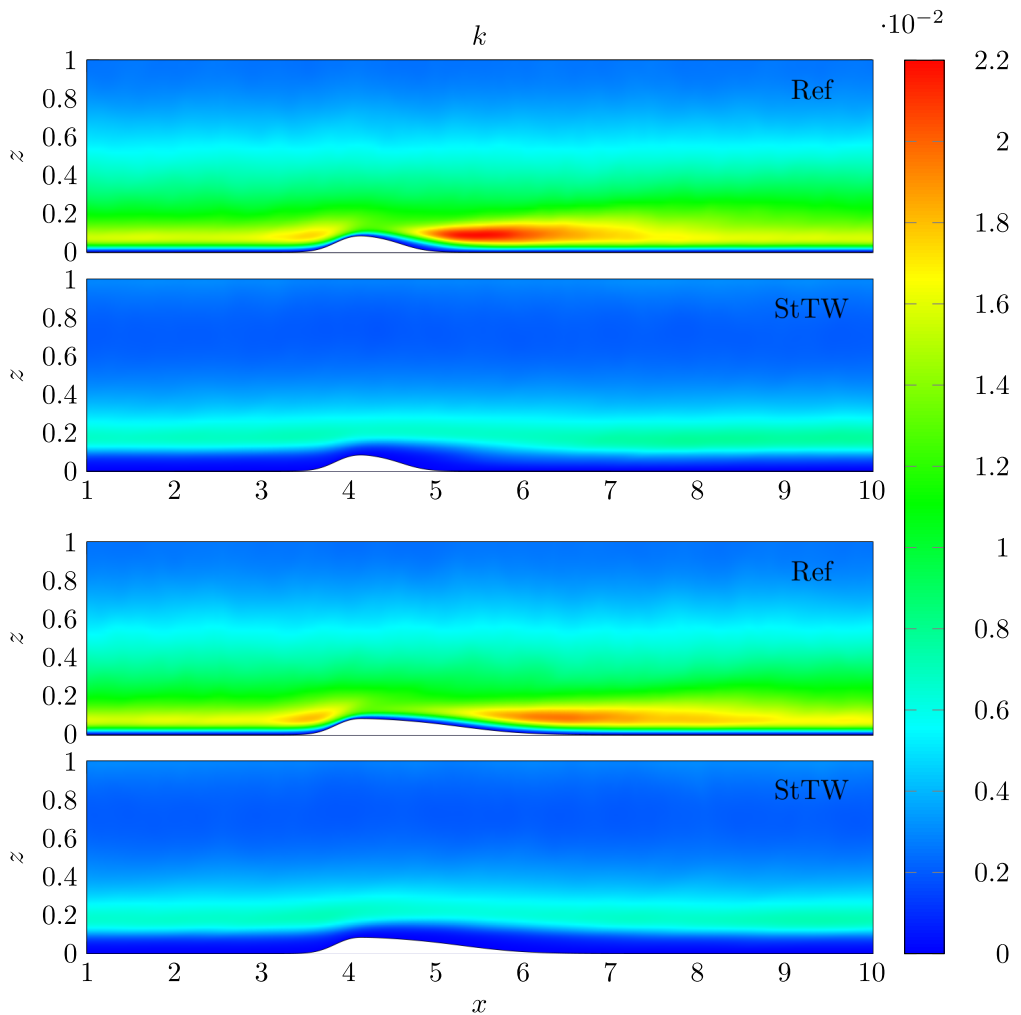


Figure 3.11: Colour plot of the turbulent kinetic energy, in outer units, for the bump G_1 (top) and G_2 (bottom), with and without StTW.

is defined by subtracting the local mean field and, for the StTW case, by employing a phase average to additionally remove the contribution of the spanwise Stokes layer.

In agreement with literature, for the reference cases figure 3.11 shows two areas of high k : one just ahead of the bump, and the other, more intense, immediately after the bump tip, extending approximately one bump length and related to the strong adverse pressure gradient (Wu and Squires, 1998). Marquillie, Ehrenstein, and Laval (2011) discuss a similar picture based on the streamwise distribution of the maximum of turbulent kinetic energy. For the milder bump G_2 the strong peak after the tip is weakened, whereas the local maximum before the tip is unchanged.

The controlled cases show both quantitative and qualitative differences. At the inlet, in agreement with the observations by Quadrio and Ricco (2011) for the flat wall, the maximum value of k (measured in outer units) is reduced by StTW and displaced at larger wall distances, and small values of k are observed within the Stokes layer. The interaction with the bump appears to be minimal, with the peak value of k remaining nearly constant along the streamwise coordinate, suggesting that the Stokes layer effectively hinders the propagation of the geometrical perturbation made by the bump into the buffer layer and above. There appears to be no substantial difference between G_1 and G_2 .

In figure 3.12 the turbulent production P of turbulent kinetic energy:

$$P = -\langle u'_i u'_j \rangle \frac{\partial \langle u_i \rangle}{\partial x_j} \quad (3.12)$$

is plotted to show that the spatial distribution of k is consistent with that of its production: even for P , the strong streamwise variation of the reference case is significantly altered by the StTW. Over the bump without actuation, as already observed by Mollicone et al. (2017), the turbulent production increases slightly before the bump and then drops to slightly negative values in the accelerated region just before the bump tip. A large positive peak of turbulent production follows, beginning at the bump tip. The intensity of the local maxima is lower for G_2 . When StTW is applied, the two cases show a similar behaviour: streamwise changes of P are strongly inhibited, and only a local slightly negative minimum in the accelerating region can be detected, though both the extension and the absolute value of the minimum are considerably reduced. In addition, careful scrutiny of the various contributions to P (not shown) reveals that the major cause for the difference between the uncontrolled and controlled flows rests with the field of the Reynolds stresses, while the gradients of the mean flow are much less affected.

The increase of turbulent activity is related to the friction increase producing the overshoot in the c_f curves of figure 3.8 downstream of the bump. Figures 3.11 and 3.12 confirm that, with StTW, turbulent activity is inhibited and no overshooting is found in the friction distribution. It is the area immediately downstream the bump tip (see figure 3.10) that is associated with the extra friction reduction.

3.4.2.2 Pressure drag reduction

A similar analysis is now carried out for pressure drag, for which simple extrapolation from the planar case would indicate no reduction at all. Figure

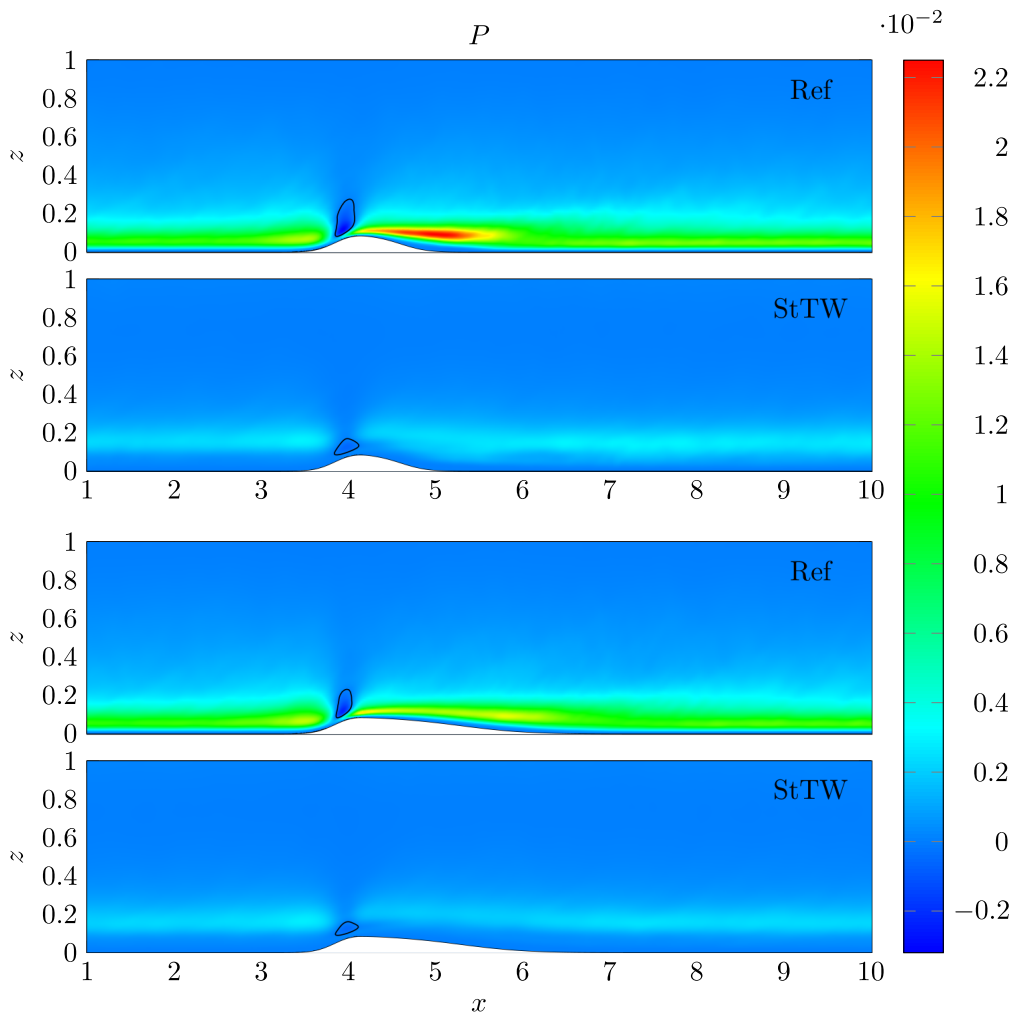


Figure 3.12: Colour plot of the production P of turbulent kinetic energy. The level $P = 0$ is indicated by the contour line. Panels as in figure 3.11.

3.13 examines first the streamwise distribution of $\Delta c_{d,p}(x)$, the pressure component of (3.10). The upper panel plots $\Delta c_{d,p}(x)$ for both bumps, and the lower panel shows $R_p(x)$, the pressure component of (3.11).

As already shown in figure 3.9, StTW reduces the positive pressure peak upstream of the bump, as well as the negative one near the bump tip. In terms of drag, the reduction of the first peak is beneficial, and translates into a local drag reduction and a positive $\Delta c_{d,p}(x)$ with a similar (albeit not identical) local maximum for both geometries, located at the same streamwise coordinate. Such agreement between the two geometries implies that the reduction of pressure drag in the anterior part of the bump is not related to the changes in the separation bubble. The attenuation of

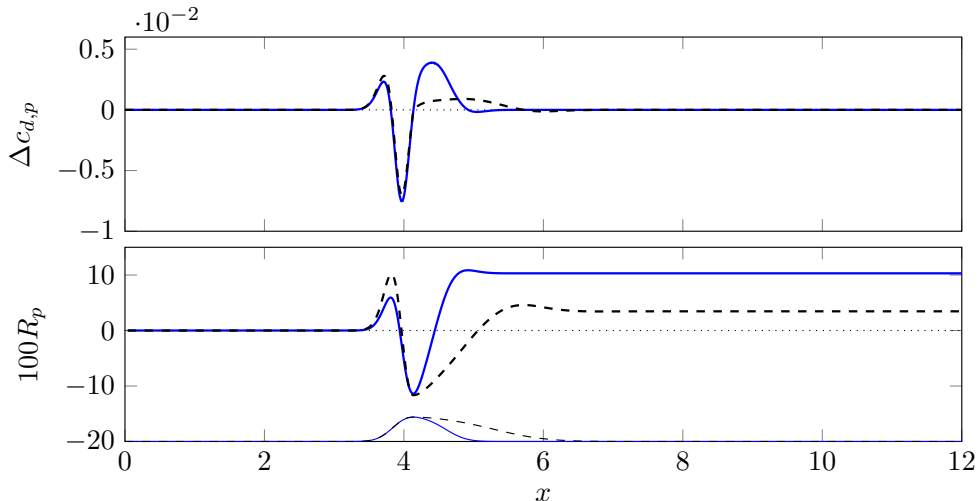


Figure 3.13: Comparison of the contribution to pressure drag changes between G_1 (blue) and G_2 (black dashed). Top: $\Delta c_{d,p}(x)$; bottom: integral budget R_p for both geometries. The thin profiles at the bottom of the plot draw the two bump geometries.

the first pressure peak alone produces 6% of pressure drag reduction for the geometry G_1 and 10% for G_2 . The reduction in the intensity of the second, negative pressure peak starts upstream of the bump tip, and extends downstream. Because of the orientation of the surface normal, before the tip such changes are detrimental to drag reduction, and become beneficial after the tip. The negative peak of $\Delta c_{d,p}(x)$ is essentially identical for both geometries up to the bump tip; however, in the region downstream of the tip, the different local slope of the wall implies a different projection of wall-normal force in the horizontal direction. For this reason, the milder bump G_2 only partially benefits from the increased pressure recovery in the aft part of the bump. The global effect is therefore a 10% pressure drag reduction for G_1 , and only 3% for G_2 , as already shown in tables 3.1 and 3.2.

Pressure drag reduction has been shown to be unrelated to changes in the separation bubble produced by G_1 . However, it is interesting to explore such changes, although they produce no significant effect in the global drag budget. The streamwise extent of the separated region is determined by looking at the zeroes of the skin-friction distribution shown in figure 3.8. The detached region starts at $x_{d,0} = 4.67$ for the reference case and at $x_d = 4.6$ for the one with StTW: two detachment points are very close to each other, with the spanwise forcing that mildly anticipates the detachment point. The two reattachment points are at $x_{r,0} = 5.03$ and

$x_r = 5.32$ respectively. Overall, the StTW produces a longer separated region, with length $L_s = 0.72$, twice the length of the reference case $L_{s,0} = 0.36$. Equivalent information was already available from figure 3.6, where the spatial extent of the recirculating region was determined from the zero of the streamwise component of the velocity. The intensity of the recirculating flow, in terms of largest negative wall shear stress, increases by 60% with StTW.

The inner structure of the separation bubble is further investigated, following Simpson, Chew, and Shivaprasad (1981), by locally computing the probability γ_u that $u > 0$. Incipient detachment is conventionally associated to $\gamma_u = 0.99$, i.e. backflow is observed only for 1% of the time; intermittent transitory detachment takes place when $\gamma_u = 0.80$, transitory detachment when $\gamma_u = 0.50$, and full detachment when $\langle \tau \rangle = 0$. Figure 3.14 is a colour plot of γ_u , along with the contour lines corresponding to the three values of γ_u mentioned above. Moreover, table 3.3 contains quantitative information regarding the detachment and reattachment points, as well as the spatial extent of the separated region.

	$x_{d,0}$	x_d	$x_{r,0}$	x_r	$L_{b,0}$	L_b
$\langle \tau \rangle = 0$	4.67	4.60	5.03	5.32	0.36	0.72
$\gamma_u = 0.5$	4.65	4.59	5.04	5.33	0.39	0.74
$\gamma_u = 0.80$	4.64	4.59	5.06	5.34	0.42	0.75
$\gamma_u = 0.99$	4.58	4.58	5.18	5.40	0.60	0.82

Table 3.3: Detachment and reattachment points for the reference and controlled cases, along with longitudinal extent deduced for specified values of the probability function γ_u .

The plot confirms that a longer separation bubble is created by StTW, but adds the information that the recirculating region also undergoes qualitative changes. The reference flow presents a diffused interface between the core of the recirculation, where γ_u is closed to 0, and the attached flow, where $\gamma_u = 1$, whereas the case with control shows a sharper interface, hinting at a separation bubble that is almost steady and does not undergo temporal oscillations.

The separation bubble over the bump G_1 is further investigated in figure 3.15, where the streamlines of the mean flow field are plotted along with the contour lines of γ_u , already shown in the context of figure 3.14.

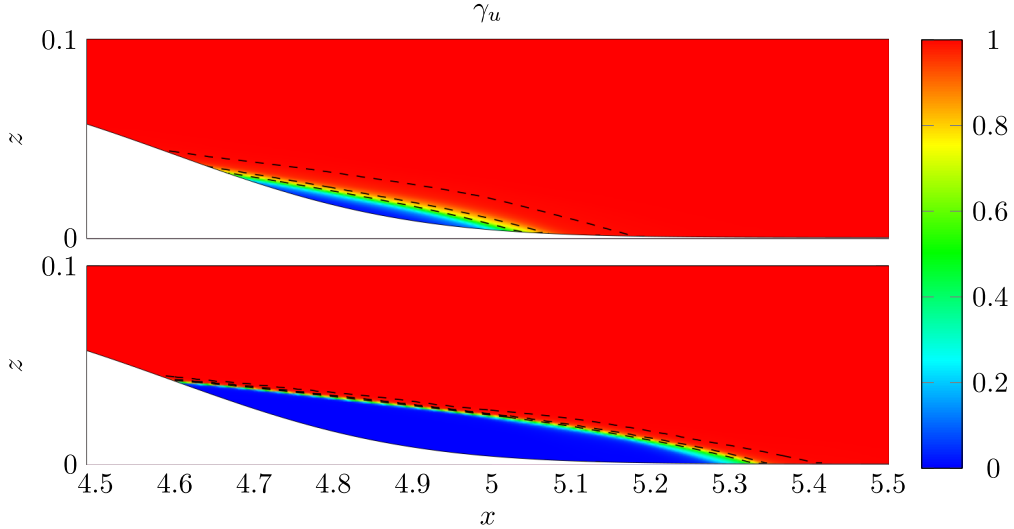


Figure 3.14: Contour of the probability γ_u of non-reverse flow, without (top) and with (bottom) StTW over the bump G_1 . Black lines identify contours of $\gamma_u = (0.50, 0.80, 0.99)$ involved in the definitions by Simpson, Chew, and Shivaprasad (1981).

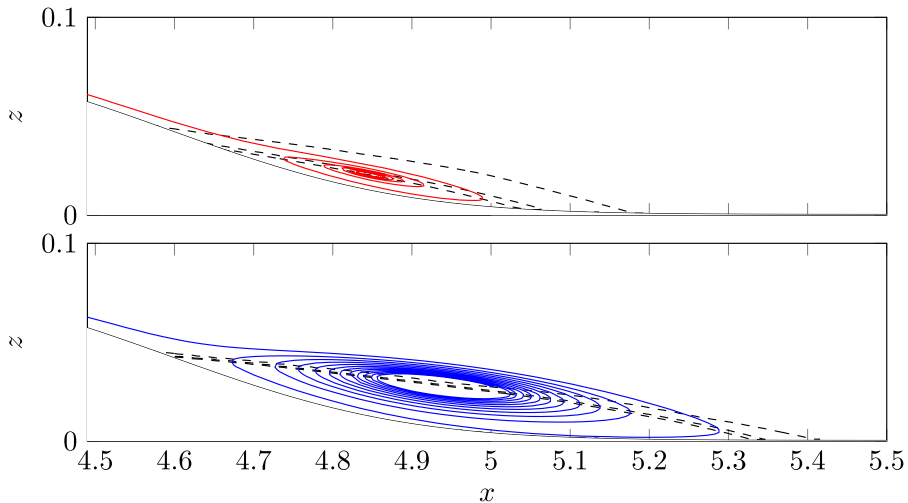


Figure 3.15: Streamlines of the mean flow field, without (top) and with (bottom) StTW over the bump G_1 . Black lines identify contours of $\gamma_u = (0.50, 0.80, 0.99)$.

3.5 Global power budget

The StTW is an active flow control technique, which requires actuation power and is capable to favourably altering the power budget in a turbulent plane channel flow (Quadrio, Ricco, and Viotti, 2009). The power

budget related to the lower wall is now computed separately for the plane wall (i.e. the periodic simulation that feeds the portion of the channel with the bump) and the bumped wall, and reported in table 3.4 for the bump G_1 . Figures are normalized with the power P_{tot} due to the total drag of the non-actuated case.

	Plane			Bump			
	Ref	StTW	Δ	Ref	StTW	Δ	Extrapolated
P_{tot}	1	0.545	-0.455	1	0.535	-0.465	-0.418
P_{req}	-	0.340	+0.340	-	0.312	+0.312	+0.313
P_{net}	-	-	-0.115	-	-	-0.153	-0.105

Table 3.4: Power budget for the bump G_1 . Here, P_{tot} is the power required to overcome the total drag produced by the lower wall, P_{req} is the power required for actuation, and $P_{net} = P_{tot} - P_{req}$ represents the net balance. Figures are for the lower wall only.

In the plane geometry, where no pressure drag is present, results agree with those by Gatti and Quadrio (2016). The percentage reduction of pumping power is by definition identical to the change $\Delta C_{d,f}$ of the distributed losses already reported in table 3.1. The net power saving is positive but amounts to only 11.5% of the reference total power, since in the present study StTW is made to work to maximize its drag-reducing effect, hence the required actuation power P_{req} is quite large, namely 34% of the total power.

Over the curved wall, StTW reduces friction drag by an amount that exceeds that of the plane wall, and decrease pressure drag too. To quantify its extra benefit, an additional column in table 3.4 reports the "extrapolated" power budget, obtained via the assumption (already discussed in §3.4.1) that the planar friction reduction carries over to the frictional drag component, with no effect on the pressure component. In table 3.4, the total power is reduced by 46.5% instead of 41.8%, with a 10% relative improvement. Since actuation power is almost unchanged, the net savings become 15.3% instead of 10.5%, with a relative increment of almost one-half. These specific figures obviously depend on the ratio between friction and pressure drag, i.e. on the bump geometry and the relative extent of the planar surface; a larger difference between actual and extrapolated net power saving can be expected for a larger bump.

The power budget for the bump G_2 is reported in table 3.5.

The plane wall obviously shows the same figures as the previous case, the minor differences being due to finite averaging time. The non-planar wall is qualitatively similar too, with a total drag reduction of 46.3% instead of

	Plane			Bump			
	Ref	StTW	Δ	Ref	StTW	Δ	Extrapolated
P_{tot}	1	0.535	-0.465	1	0.538	-0.463	-0.437
P_{req}	-	0.336	+0.336	-	0.312	+0.312	+0.317
P_{net}	-	-	-0.129	-	-	-0.151	-0.120

Table 3.5: Power budget for G_2 , as in table 3.4.

43.7%. The net power saving is 15.1% of the total power, i.e. larger than the extrapolated value of 12%. Hence, for both attached and separated flow, StTW produces extra benefits when applied over curved walls.

A final comment is about the power budget discussed above, which concerns only the lower wall with the bump. Indeed, additional benefits appear once the upper, flat wall is included. Even though the upper wall has no actuation, StTW applied on the lower wall induces an asymmetry in the mean streamwise velocity profile, so that friction is reduced by 4% on the upper wall too. This asymmetry, which is also present in the planar case, is explained by the displacement of momentum towards the wall with lower friction. Figure 3.16 plots the two mean streamwise velocity profiles, with and without StTW, for the planar case: the velocity maximum is displaced towards the lower actuated wall. This extra benefit on

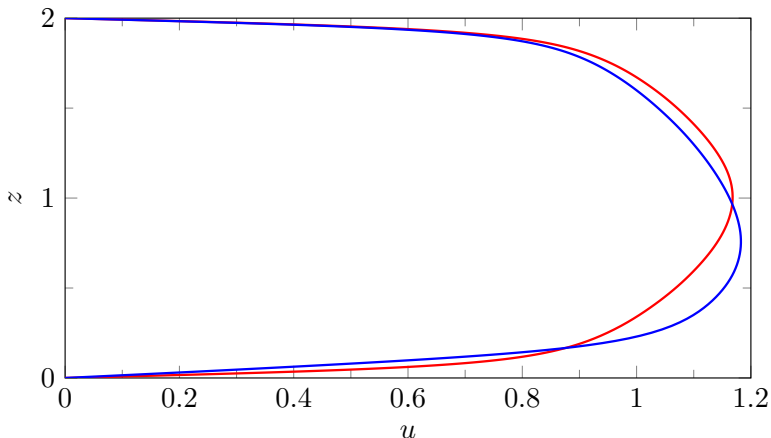


Figure 3.16: Streamwise mean velocity profile in the periodic plane channel. Comparison between reference flow (red) and actuated flow on the lower wall (blue).

the upper wall, obtained with no additional power, brings the global drag reduction for the whole channel containing the bump G_1 to 26%, 4% more than the extrapolated value, and a net power savings of 10%, i.e. nearly doubling the extrapolated value.

3.6 Conclusions

Direct Numerical Simulations of an incompressible turbulent channel flow with a curved wall have been carried out to understand how skin-friction drag reduction affects the total drag. One of the channel walls has a small bump that generates a pressure contribution to the total drag. Two bump geometries are considered, to study cases with and without separation. The flow is modified by a spanwise-forcing technique (streamwise-travelling waves of spanwise wall velocity, or StTW) known to reduce friction drag. Parameters of StTW are tuned to yield a large skin-friction drag reduction of 46% in the plane case. Friction and pressure distributions over the entire domain length are studied to quantify changes to drag and to the global power budget. The study demonstrates that, for both bumps, the actual power saving obtained by StTW is larger than the extrapolated value obtained by carrying the planar friction reduction over to the friction component of the total aerodynamic drag, while assuming no effect on the pressure component.

In the flow without actuation, friction locally increases in the anterior part of the bump; a local minimum is observed just downstream of the bump tip, with negative values in case of flow separation. The friction then re-increases to reach values slightly larger than the planar one, and eventually recovers slowly, so that a long downstream distance is required to attain the planar value again. When StTW are used, their efficiency varies along the streamwise coordinate, and in particular there is no friction overshooting after the bump, so that a wide region exists where the local friction reduction rate is higher than that of the planar case.

The pressure distribution is modified by changes in friction. The StTW induces a considerable reduction of pressure drag, which amounts to more than 10% for the cases studied. We have established that pressure drag reduction is not directly linked to flow separation, as it is observed with both bump geometries. When present, however, the separation bubble is significantly affected by the StTW. Indeed, the separated region becomes larger, but at the same time strongly stabilized, almost lacking temporal oscillations.

The combined effect of the StTW upon friction and pressure drag generates a considerable improvement of the global energy-saving performance of StTW. In the simulations described in our study, the amount of net power savings is about one-half larger than in the plane channel alone. If the modifications induced by StTW onto the opposite, non-actuated plane wall are accounted for, the net power savings are increased by 100%.

At any rate, such significant improvements still are underestimates, since these figures strongly depend upon the bump geometry, which has been chosen here without prior knowledge.

It is not immediate to generalize these results to different geometries, or to different drag reduction techniques. Based on preliminary studies, we can at least vouch for the general picture to remain unchanged when variants of spanwise forcing are employed. However, the main point made by the present work is simply to establish, albeit in a specific case, a concept that sometimes tends to be overlooked: altering the frictional component of the aerodynamic drag in a complex configuration leads to changes in the pressure drag too. This confirms the fundamental idea of recent works (see e.g. Mele, Tognaccini, and Catalano, 2016) where a RANS-based estimate of the reduction in the overall drag of a modern commercial aircraft covered by riblets was made. Such an estimate has a limited reliability (because of the RANS approach, and because riblets were accounted for indirectly via a modification of the turbulence model at the wall). However, the results seem to indicate that skin-friction drag reduction applied to a body of complex shape provides extra benefits compared to the plane case. This is in agreement with the present DNS-based study, and motivates further research efforts in this direction. In particular, it is intriguing to notice how Mele, Tognaccini, and Catalano (2016) found that the largest beneficial indirect effect from riblets descend from the interaction between the modified skin-friction and the shock wave on the airplane wing. This effect is obviously absent in the present, incompressible flow.

CHAPTER 4

DRAG REDUCTION FOR A TRANSONIC WING SLAB

Yes, we can.

BARACK HUSSEIN OBAMA II

THIS chapter deals with turbulent skin-friction drag reduction applied over an airfoil in transonic regime. Direct numerical simulations are carried out with and without actuation, in order to investigate its effect on the aerodynamic forces. Friction drag reduction is achieved by applying streamwise-travelling waves of spanwise velocity (StTW) at the wall.

The StTW is observed to reduce friction and to modify the shock-wave position in agreement with previous RANS-based works. The consequent influence on pressure distribution provides a substantial lift increase of 10%. The present work, albeit represents a preliminary investigation, assesses that friction reduction techniques can be applied locally to produce a global benefit.

The results reported in this chapter represent the introductory study of

an on-going collaboration with Sergio Pirozzoli (Università La Sapienza) and Antonio Memmolo (CINECA).

4.1 Introduction

The flow field around an airfoil has always been considered a first step to understand and enhance the aircraft wing performances. Despite its practical importance, only a few structure-resolved numerical studies have been performed around an airfoil in the past years. Jansen (1996) performed Large-Eddy Simulations (LES) around the NACA4412 airfoil at Reynolds number $Re_\infty = 1.6 \cdot 10^6$ in order to enhance the available experimental campaigns. Shan, Jiang, and Liu (2005) employed Direct Numerical Simulation (DNS) to study the flow around the symmetric NACA0012 wing profile at $Re_\infty = 1 \cdot 10^5$. More recently, Hosseini et al. (2016) increased the Reynolds number up to $Re_\infty = 4 \cdot 10^5$, investigating the flow around the NACA4412 wing section. In its follow up work, Atzori et al. (2018) applied drag reduction via uniform blowing and body-force damping of near-wall turbulent fluctuations to observe the impact of the pressure gradient on the actuator efficiency. This analysis, however, was performed in incompressible regime and did not capture the whole complexity of the flow field around an aircraft wing in transonic cruise flight.

The present work aims at investigating the effect of friction reduction techniques applied over an airfoil in transonic regime. Previous RANS-based works performed over a whole-aircraft in transonic regime hint that friction reduction techniques interact with the shock-wave position, drastically improving the overall wing performances (Mele, Tognaccini, and Catalano, 2016; Gadda et al., 2017). The DNS are carried out to investigate via more reliable tools, the influence of StTW on the already complex shock-wave boundary layer interaction (SBLI) (Delery, 1983). A shock-wave imposes a strong adverse pressure gradient on the boundary layer, which may cause its thickening and flow separation. The shock-wave effect can propagate even upstream of its region, since the inner part of the boundary layer is always subsonic and the upstream propagation of disturbances is not inhibited. The compression waves caused by the boundary layer thickening can coalesce and bring another shock. If the shock is not strong enough to cause separation, the flow structure is relatively simple, predominantly inviscid. A simple sketch is reported in the left panel of figure 4.1. On the other hand, if the shock is strong enough to cause separation, as shown in the right panel of figure 4.1, the entire flow-field may be affected, with the formation of intense vortices or intricate shock patterns (Babinsky and Harvey, 2011). Transonic buffet, a periodic motion with a

consequent low-frequency unsteadiness that involves the entire flow field, is a possible consequence of a strong shock-wave (Memmolo, Bernardini, and Pirozzoli, 2018).

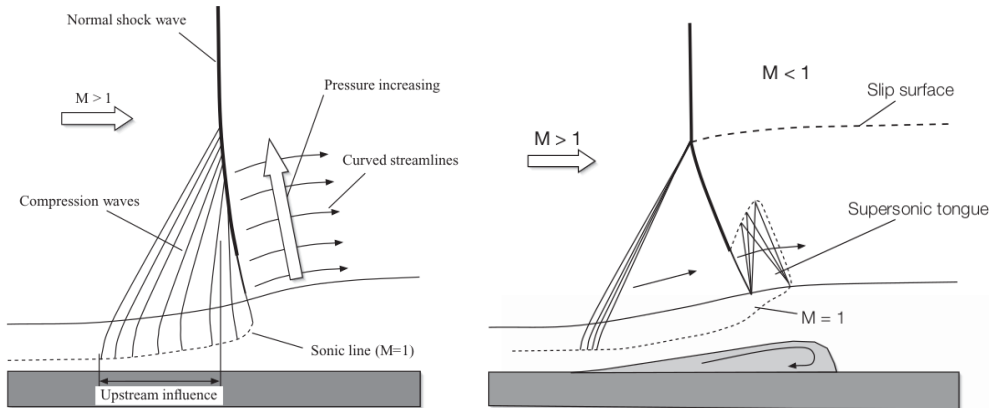


Figure 4.1: Sketch of a weak (left) and strong (right) transonic SBLI. Taken from Babinsky and Harvey (2011).

4.2 Simulations

Direct Numerical Simulations are carried out for a wing slab in transonic regime. Streamwise-travelling waves for the reduction of friction drag are imposed over the suction side of the airfoil, and their effect on the aerodynamic forces is measured.

The DNS code solves the compressible Navier–Stokes equations for calorically perfect gas in integral form, already validated for transonic applications (Memmolo, Bernardini, and Pirozzoli, 2018). The second-order finite volume approach is employed to solve the equations; a modified Ducros sensor (Ducros et al., 1999) is employed to switch the discretization scheme to third-order weighted essentially non-oscillatory (WENO) near discontinuities. The gradients normal to the cell faces are evaluated through second-order central-difference approximations. The far-field numerical boundary conditions rely on characteristic decomposition to identify waves entering and leaving the domain (Poinsot and Lele, 1992). Time advancement is carried out through the low-storage third-order Runge–Kutta algorithm (Orlandi, 2006).

Simulations with and without actuation are carried out in transonic regime at Mach number of $M_\infty = U_\infty/a_\infty = 0.7$ and Reynolds number of $Re_\infty = U_\infty c/\nu = 3 \cdot 10^5$. In their definitions, c is the airfoil chord, ν is the

kinematic viscosity of the fluid, U_∞ is the free-stream velocity, whereas a_∞ represents the free-stream sound speed. In the following, quantities are made dimensionless with c and U_∞ .

The computational domain has dimensions of $(L_x, L_y, L_z) = (100, 0.1, 100)$ in the chord-wise, spanwise and vertical directions respectively. The computational mesh is made by approximately $5 \cdot 10^8$ grid points with $(n_x, n_y, n_z) = (4096, 256, 512)$, that respects at the wall the limit of $\Delta x^+ < 10$, $\Delta y^+ < 5$, $\Delta z^+ < 0.5$ (Memmolo, 2018). Figure 4.2 portrays a sample of the computational mesh employed.

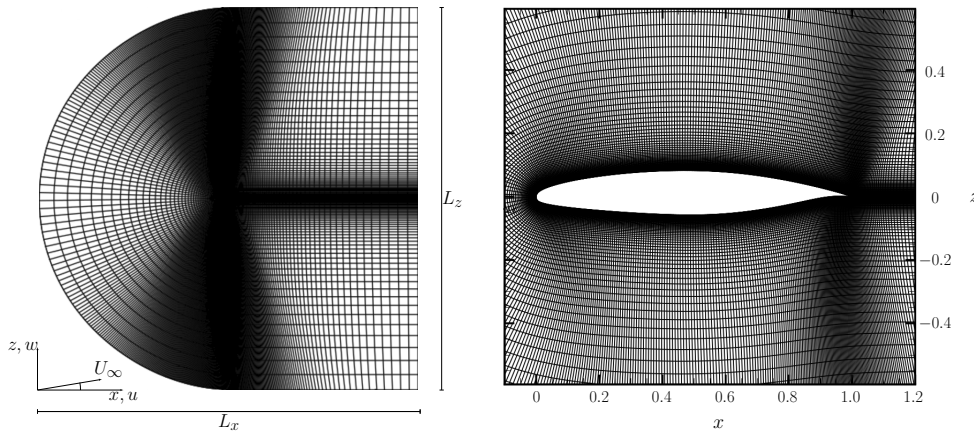


Figure 4.2: Cross-section of the computational mesh, with the whole domain on the left and a zoom on the airfoil on the right. Adapted from Memmolo (2018).

The flow field around a wing slab based on the supercritical V2C airfoil (designed by Dassault Aviation to investigate the SBLI) is studied at angle of attack of $AoA = 4^\circ$. Figure 4.3 plots the V2C airfoil shape compared with the widespread NACA0012 airfoil. In both pressure and suction side

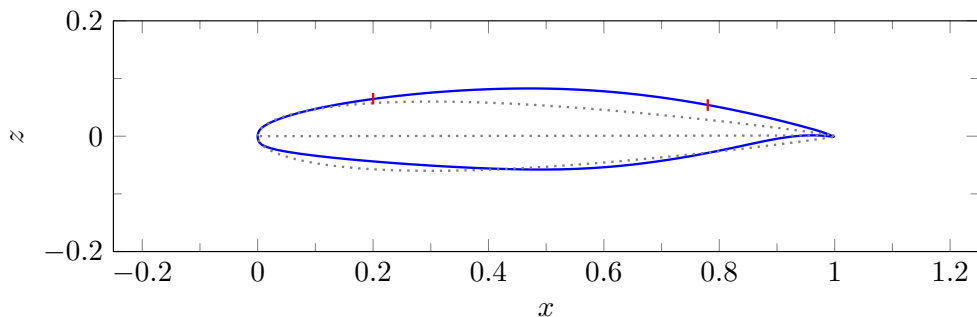


Figure 4.3: Airfoil geometry V2C (blue) plotted together with the NACA0012 airfoil (gray, dotted). The red lines denote the location where forcing starts and ends.

of the airfoil, transition to turbulence is forced via volume force (Schlatter and Örlü, 2012), located at $x = 0.1$, downstream the leading edge. Alternative tripping strategies have been tested and reported by Memmolo (2018). In the uncontrolled case, already investigated by Memmolo (2018), no transonic buffet occurs, and one normal steady shock-wave is present over the suction side of the V2C airfoil.

The considered skin-friction reduction technique is the streamwise-travelling wave (StTW) of spanwise velocity; it is applied over the suction side only from $x_{start} = 0.2$ to $x_{end} = 0.78$. The imposed spanwise velocity is damped at the two extremes via the filter function $f(x)$, already employed in this context by Yudhistira and Skote (2011), to avoid discontinuity in the spanwise wall velocity. Equal rise and fall distances are imposed at $\Delta x_{rise} = \Delta x_{fall} = 0.05$. The spanwise velocity imposed at the wall by StTW is defined as follows:

$$V_w(x, t) = f(x) \cdot A \sin(\kappa_x x - \omega t). \quad (4.1)$$

where V_w is the spanwise velocity at the wall, A is its maximum amplitude, and κ_x and ω represent the spatial and temporal frequencies of the wave. Optimal tuning of the StTW over external surfaces is not an easy task, since friction velocity changes along the airfoil. For simplicity, the forcing parameters are kept constant over the entire controlled surface and are tuned by using available information on the non-actuated case. The average friction velocity, namely u'_τ , computed over the portion from $x = 0.2$ to $x = 0.4$ of the suction side of the uncontrolled airfoil, is employed to estimate the optimal tuning. The selected values $A = 0.684$, $\omega = 11.3$ and $\kappa_x = 161$ are chosen after a parametric study performed with a coarser mesh, and correspond to $A^+ = 9$, $\omega^+ = 0.06$ and $\kappa_x^+ = 0.013$ when nondimensionalized by using u'_τ . Assessing the expected friction reduction, however, is not trivial, since Re_τ cannot be defined as in channel flows and the boundary layer is not fully turbulent. The selected parameters yield around 35% of drag reduction in a turbulent plane channel flow at $Re_\tau = 200$.

Flow statistics are accumulated, after reaching statistical equilibrium, for a time interval of $T = 5$ with a constant time step $\Delta t = 1.5 \cdot 10^{-4}$. The accumulation time of the controlled case is therefore six times lower than the one of the reference simulation. Unfortunately, owing to an unexpected architecture update, the employed computational platform at CINECA was discontinued and it was not allowed to continue the simulation further. Luckily, a careful examination of the time history of the flow statistics and, in particular, of the force coefficients allows to be confident that the results are converged from a qualitative viewpoint, although care should

be exercised in their precise quantification until a larger simulation time is possible.

The results shown in this chapter represent a preliminary investigation on friction reduction techniques applied over transonic airfoil. Because of the limited Reynolds number, numerical tripping does not lead to a fully turbulent boundary layer, as shown by Memmolo (2018). The StTW efficiency could strongly depend on the boundary layer state. In this context, the distance between the tripping point and the actuator represents a critical parameter that could affect the overall picture.

Notwithstanding these intricacies, this introductory investigation hints encouraging outcomes.

4.3 Instantaneous and mean flow fields

To begin with a qualitative picture, figure 4.4 portrays the complexity of the flow around the actuated airfoil.

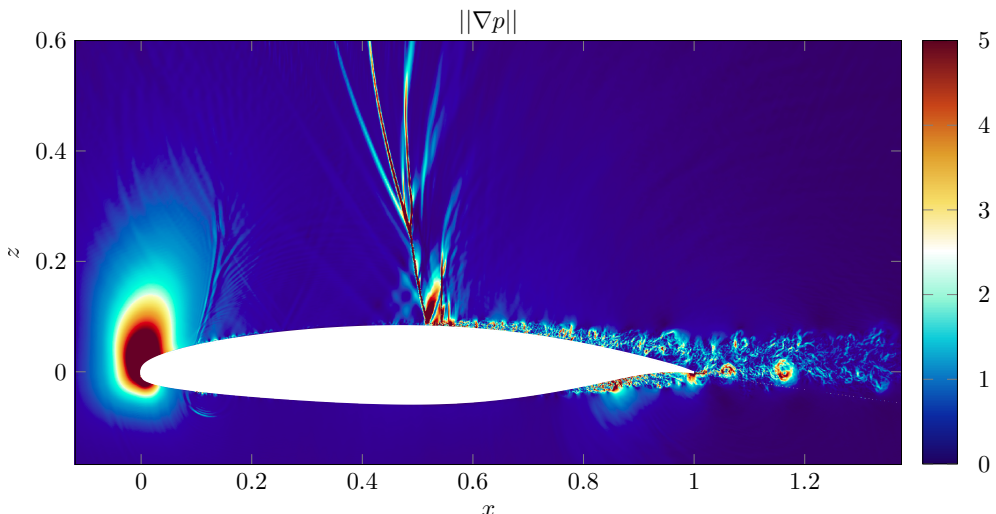


Figure 4.4: Magnitude of the pressure gradient vector $||\nabla p||$ of an instantaneous flow field around the airfoil in the controlled case.

The figure is for the controlled simulation and plots the magnitude of the pressure gradient vector $||\nabla p||$ for a vertical slice of an instantaneous flow field. The presence of at least one normal shock-wave is detected over the airfoil suction side close to the half-chord position, followed by a substantial increase of turbulent activity. Downstream of the leading

edge the strong pressure gradient is followed, over the upper side, by compression waves inside the supersonic bubble.

In order to observe the boundary layer development around the suction side of the airfoil, figure 4.5 portrays the instantaneous chord-wise velocity component over a surface at a very small distance, $3 \cdot 10^{-5}$, from the wall. In the uncontrolled case (upper), one can recognize first the tripping

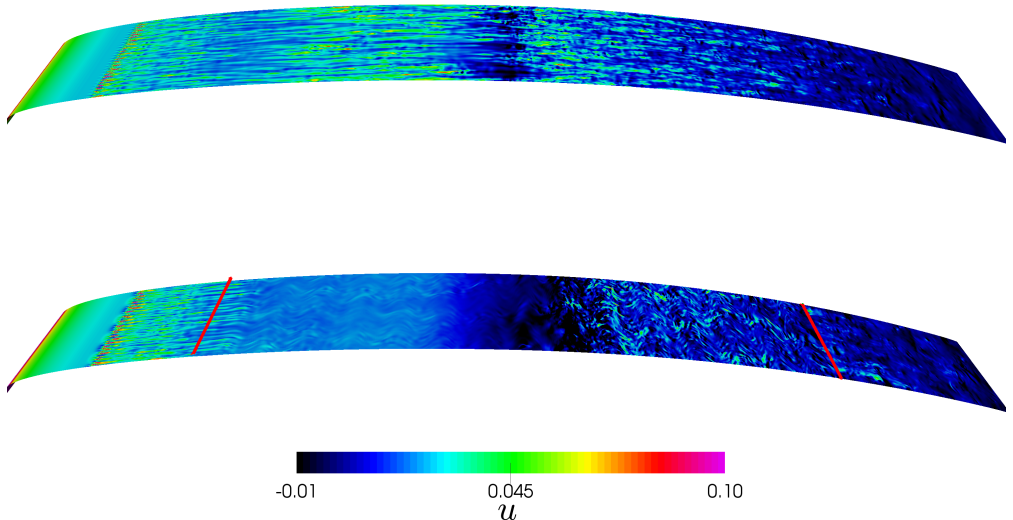


Figure 4.5: Chord-wise velocity component over the suction side of the airfoil: uncontrolled (top) and controlled (bottom) case. The red lines denote the location where forcing starts and ends.

process, then transition to turbulence with the characteristic elongated streaks, and finally, at around $x = 0.45$, a sharp decrease of fluctuations related to the shock-wave. When control is applied (lower), the spatially-oscillating behaviour of the StTW is detected, causing a substantial reduction of turbulent activity, in such a way that when shock occurs, the flow appears to be laminar. Moreover, after the shock-wave, a wider area of low/negative chord-wise velocity compared to the reference case is present, suggesting the presence of a recirculation bubble.

Moving on to the analysis of the mean flow field, for which the operator $\langle \cdot \rangle$ implies averaging over time and the homogeneous spanwise direction, figure 4.6 shows the mean pressure field $\langle p \rangle$ normalized using the free-stream pressure p_∞ , for a localized portion of the domain around the airfoil. Over the non-actuated wing slab, pressure reaches its maximum at the stagnation point, while a low-pressure area is present over the suction side, for $x < 0.5$. The sharp end of this area is followed by smooth recompression. Over the lower side, a favourable pressure gradient is present up to

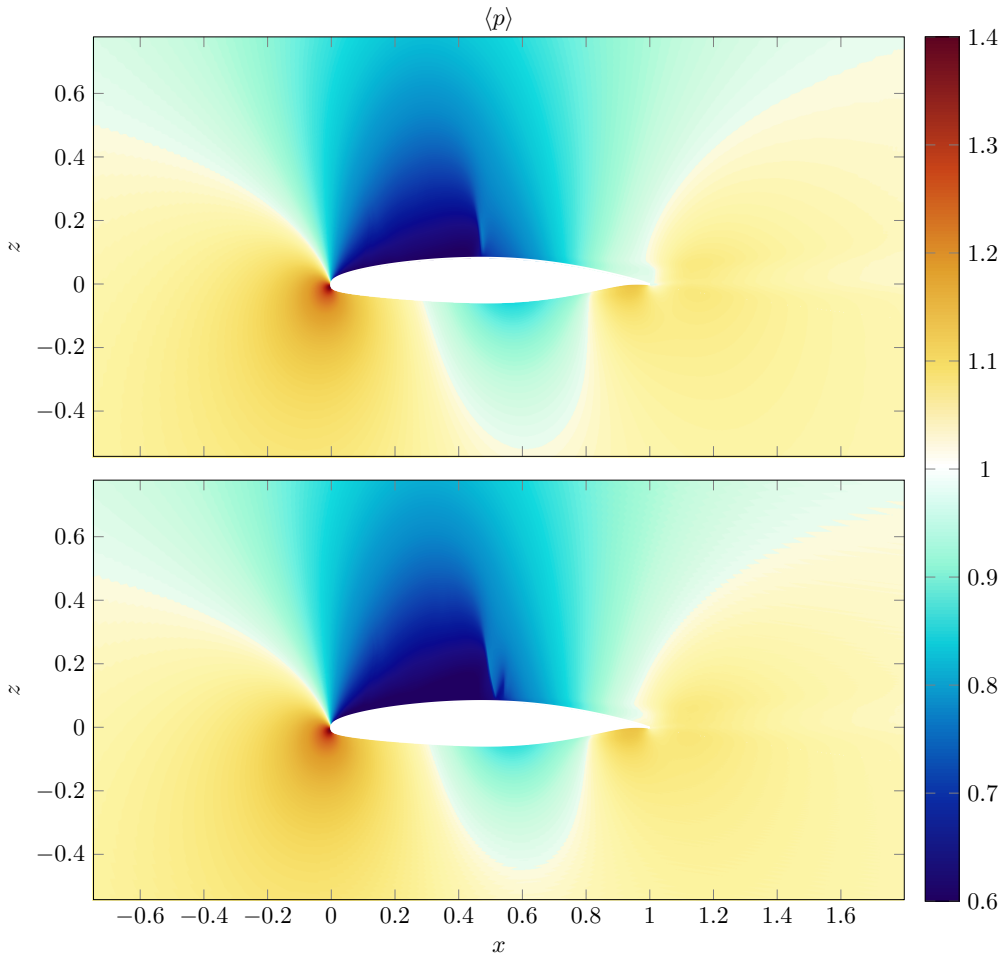


Figure 4.6: Mean pressure distribution around the airfoil. Top: reference case.
Bottom: controlled case.

$x = 0.6$, where a mild recompression takes place. When StTW is applied, the flow field far from the airfoil and over its pressure side appears to be unaffected by the control; however, the low-pressure area on the suction side ends with a different shape.

Figure 4.7 links the differences in the low-pressure area to the mean Mach distribution around the airfoil. Only the controlled case is portrayed, while contour lines denote the unitary Mach region for both reference (white) and controlled (black) cases. In the uncontrolled case, a single shock-wave is detected at the end of the supersonic area. This region terminates with a small ball, representing a local increase of speed due to the boundary layer thickening, caused by the shock-related adverse pressure gradient. In the controlled case, two supersonic areas are detected. The StTW enlarges

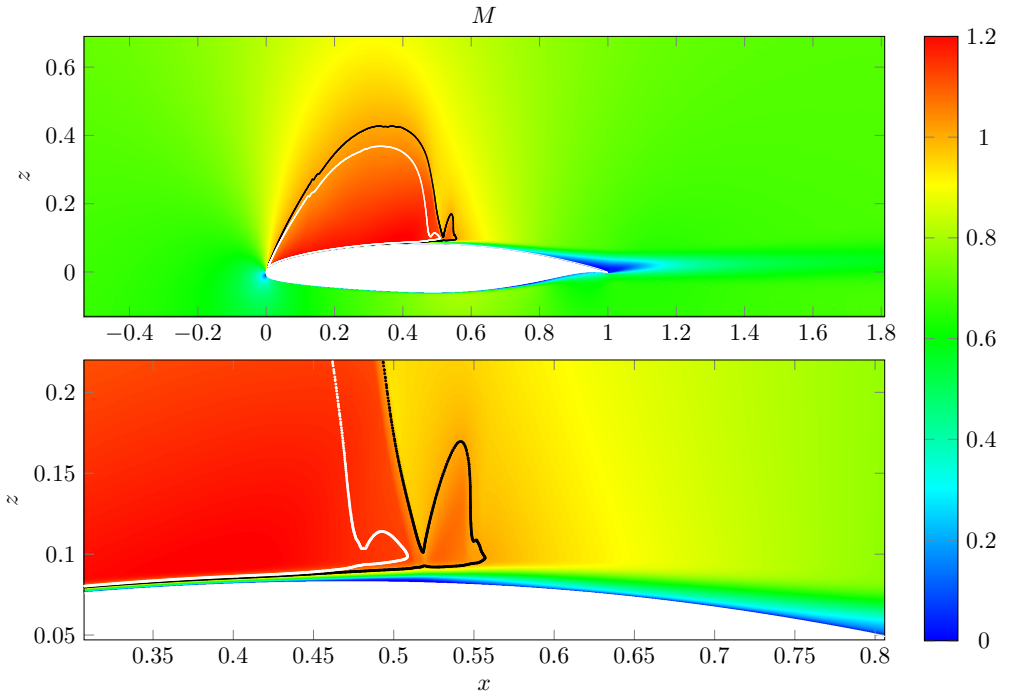


Figure 4.7: Distribution of the mean Mach number around the controlled airfoil. Contour lines are drawn at $M = 1$ for the reference (white) and controlled (black) cases. The lower panel enlarges the portion of the flow field around the shock-waves.

the chord-wise and vertical extents of the first supersonic bubble, with the related shock-wave deferred downstream. Furthermore, a second smaller supersonic area follows the first shock-wave, implying that the flow field accelerates again to the supersonic regime.

In order to better investigate how StTW influences the shock-wave properties, figure 4.8 shows the numerical Schlieren of the mean flow field, i.e. the chord-wise partial derivative of the mean density field $\partial \langle \rho \rangle / \partial x$ of a limited portion around the suction side of the airfoil. With no actuation, a single shock occurs, identified by the localized high density gradient around $x = 0.45$. When StTW is applied, two shock-waves occur, as portrayed by the Mach distribution in figure 4.7. Actuation visibly delays the first stronger shock-wave, in agreement with previous RANS-based works. Close to the leading edge, around $x = 0.1$, compression waves are visible in both cases. Over the actuated airfoil, however, the waves show a different shape, in agreement with the enlarged vertical extent of the supersonic bubble.

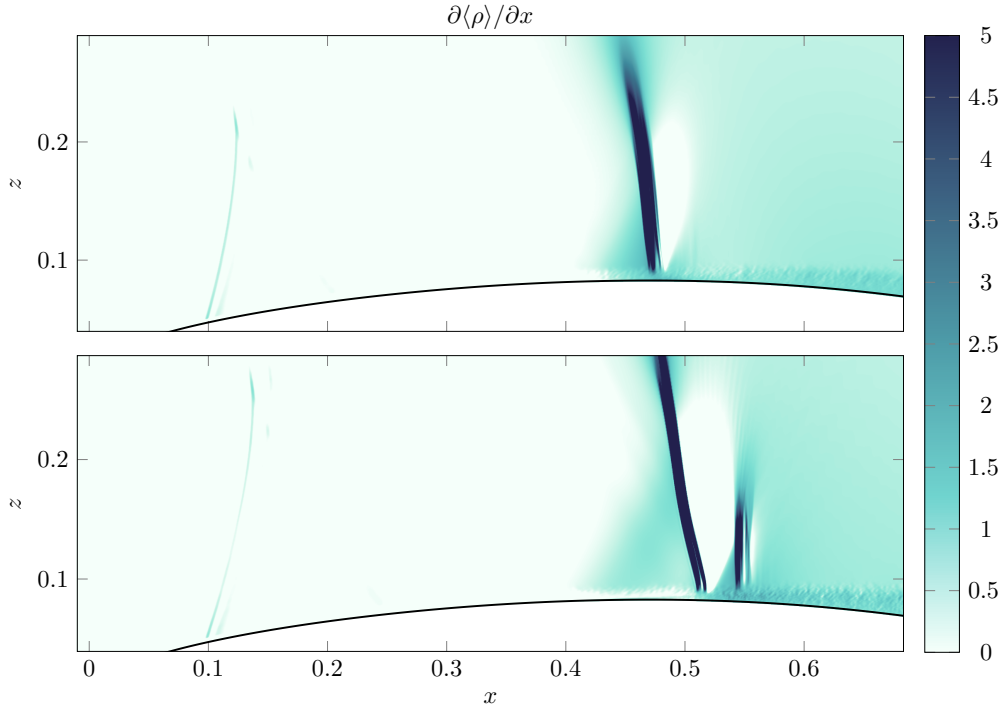


Figure 4.8: Numerical Schlieren $\partial\langle\rho\rangle/\partial x$ around the airfoil. Top: reference case; bottom: controlled case.

4.4 Friction and pressure coefficients

This analysis aims to understand the effect of friction reduction techniques on the overall aerodynamic forces of complex bodies in transonic regime. In analogy with previous chapters, contribution to forces are examined separately for friction and pressure: their local stresses are reported via non-dimensional coefficients. The friction coefficient is

$$c_f(x) = \frac{2\tau(x)}{\rho_\infty U_\infty^2}, \quad (4.2)$$

where ρ_∞ is the free-stream fluid density and $\tau = \mu \hat{\mathbf{t}} \cdot \partial \mathbf{u} / \partial n$, with $\hat{\mathbf{t}}$ the tangential unit vector, μ the viscosity of the fluid, and $\partial/\partial n$ the derivative in wall-normal direction. The pressure coefficient is

$$c_p(x) = \frac{2(p(x) - p_\infty)}{\rho_\infty U_\infty^2}. \quad (4.3)$$

Figure 4.9 compares the friction coefficient distribution over the airfoil, with and without StTW.

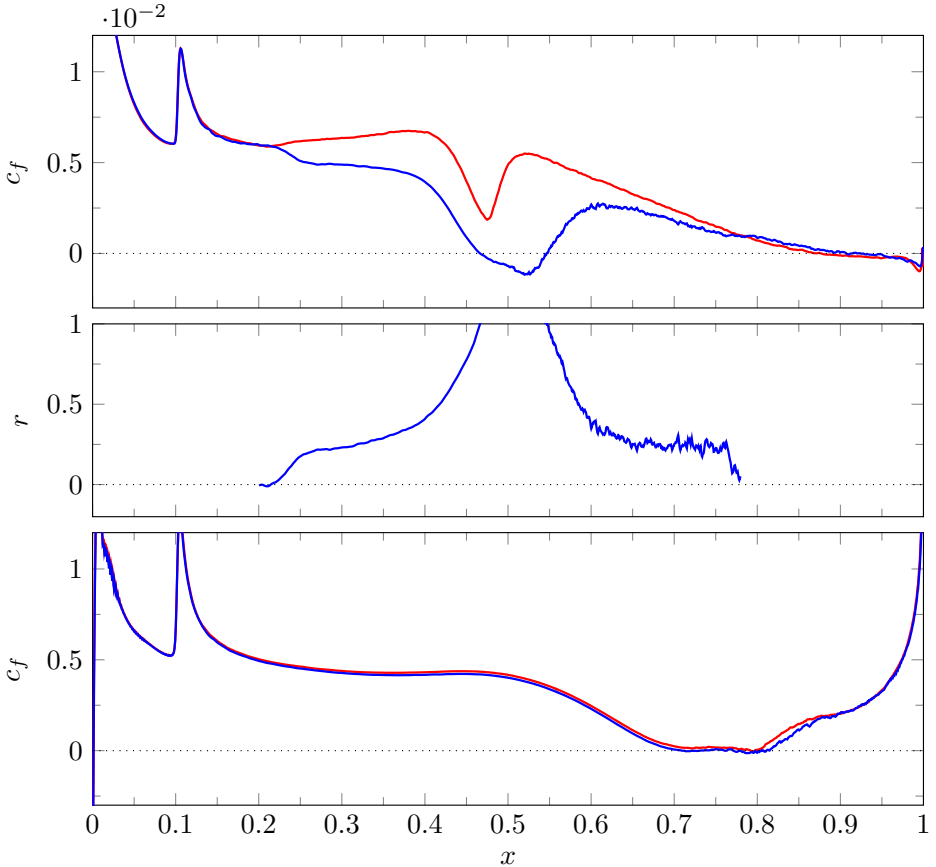


Figure 4.9: Comparison between reference (red) and controlled (blue) skin-friction distribution $c_f(x)$ over the airfoil. Top: c_f over the suction side; center: friction reduction rate $r(x)$ over the suction side; bottom: c_f over the pressure side.

The top panel plots the c_f distributions over the suction side. In the reference case (red), after the numerical tripping, whose effect is visible at $x = 0.1$, the friction coefficient first recovers its natural value, then the transition to turbulence induces a progressive increase. When the shock-wave occurs, the sharp recompression drastically lowers c_f . Downstream the shock-wave, for $x > 0.5$, the smooth adverse pressure gradient slowly decreases c_f up to the trailing edge. In the controlled case (blue), friction is reduced starting from the actuator origin, at $x = 0.2$. The interaction between the modified velocity profile and the shock-wave leads to flow recirculation; the separation bubble, identified by negative c_f , covers 10% of airfoil chord. Downstream of the actuator, for $x > 0.78$, the difference between the two curves tends to disappear. In order to quantify changes due to StTW, the local skin-friction reduction rate $r(x)$ above the actuator is plotted in the centre panel; r is defined as the relative change of $c_f(x)$

between the controlled and the reference flow:

$$r(x) = 1 - \frac{c_f(x)}{c_{f,0}(x)} \quad (4.4)$$

where the subscript 0 indicates the uncontrolled case. A first transitory phase seems to end at $r = 25\%$, around $x = 0.3$. The friction reduction rate, however, keeps increasing; the shock-wave then leads to flow separation, and r becomes meaningless. Downstream the reattachment point, r oscillates around the mean value $r = 25\%$.

The lower panel plots the friction distribution over the pressure side, where no actuation is present in both cases. As already observed over the suction side, the numerical tripping causes a local increase of friction. Downstream the recovery, c_f remains nearly constant up to $x = 0.55$, where the mild adverse pressure gradient takes place. The two curves almost coincide up to $x = 0.8$ where a small difference is observed, probably due to a limited averaging time.

The instantaneous chord-wise component of the velocity vector over a surface at a very small distance, $3 \cdot 10^{-5}$, from the wall, is portrayed in figure 4.10 to investigate the nature of the separation bubble on the suction side of the airfoil. Differently from figure 4.5, the colour map is tuned to detect attached (beige) and separated (burgundy) regions only. The first panel shows that even in the reference case, where the friction coefficient is always positive, reverse-flow partially occurs after the shock-wave. The separation is not strong enough to spread over the entire width, maintaining the mean friction coefficient always above zero. When StTW is applied, on the other hand, a wide separation bubble occurs, as already assessed by the sign inversion of the friction coefficient. Furthermore, intermittent detachment is present even way downstream of the shock-wave in both cases, due to the smooth adverse pressure gradient. Here the intermittent detachment is slightly enhanced by StTW.

The pressure coefficient over both sides of the airfoil is plotted in figure 4.11. In the reference case, a local minimum is reached on the suction side, close to the leading edge; this pressure value remains almost constant up to shock-wave recompression at $x = 0.45$. After the shock, a smooth adverse pressure gradient is present, causing the intermittent detachment observed in the context of figure 4.10. When StTW is applied, the minimum pressure value is enhanced even upstream the actuator. Moreover, a smooth adverse pressure gradient is present from $x = 0.4$ up to the shock-related sharp recompression. The latter, underlined by the dotted line, maintains its original slope while it is clearly deferred by StTW. On the pressure side the two curves almost overlap.

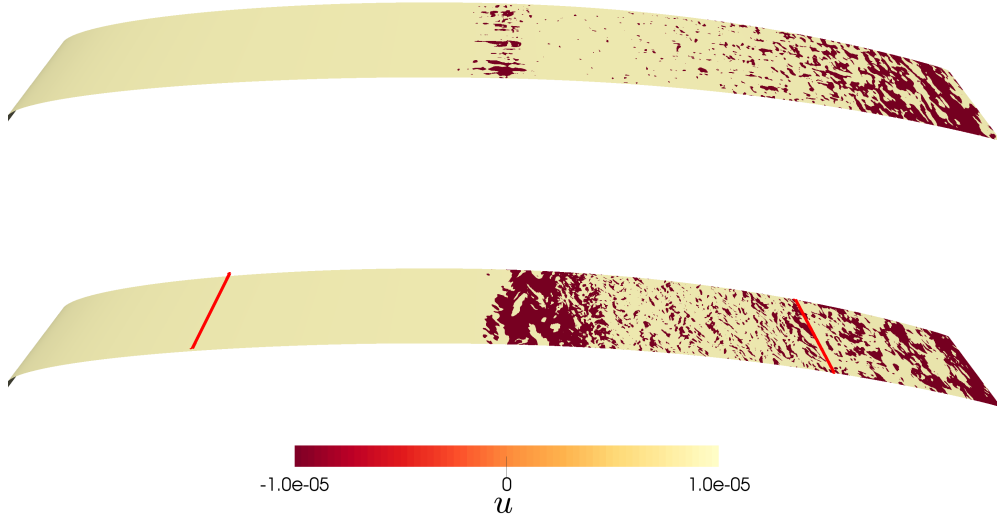


Figure 4.10: Chord-wise velocity component over the suction side of the airfoil, coloured to detect attached (beige) and separated (burgundy) areas: uncontrolled (top) and controlled (bottom) case. The red lines denote the location where forcing starts and ends.

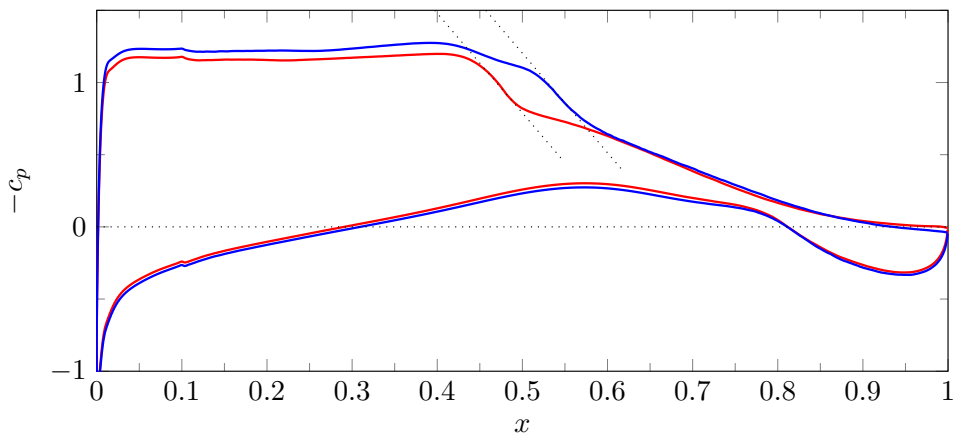


Figure 4.11: Comparison of pressure coefficient between reference (red) and controlled (blue) cases.

4.5 Aerodynamic Forces

This work aims to investigate how friction reduction techniques affect the overall forces of a wing slab in transonic regime. Changes in pressure and friction due to StTW, observed in the previous paragraph, positively affect lift and drag. Table 4.1 reports lift and drag coefficients, C_ℓ and C_d , respectively, for both reference and controlled case. The third column

underlines the relative changes due to StTW. Friction and pressure contributions to drag are computed separately and reported as $C_{d,f}$ and $C_{d,p}$, respectively.

	Ref	StTW	Δ
$C_{d,f}$	0.0084	0.0071	-15.2%
$C_{d,p}$	0.0165	0.0174	+5.5%
C_d	0.0249	0.0245	-1.5%
C_ℓ	0.74	0.815	+10.1%
L/D	29.7	33.3	+11.8%

Table 4.1: Force coefficients. Here $C_{d,f}$ and $C_{d,p}$ are the friction and pressure components of drag respectively, with the total drag $C_d = C_{d,f} + C_{d,p}$ and C_ℓ is the lift coefficient, while L/D represents the lift/drag ratio.

The StTW is observed to reduce the friction share of the total drag by 15%. The influence of StTW on the pressure field observed in the context of figure 4.11, however, produces a relative pressure drag increase of 6%. The combination of these two contributions provides a total drag reduction slightly lower than 2%. The shock-wave delay due to StTW, however, has an impact on lift coefficient too, that is increased by 10%. The wing efficiency, defined by the lift/drag ratio L/D , is therefore enhanced by 12%.

The DNS over transonic wing slab shows the same qualitative results of previous RANS-based works on the whole-aircraft configuration. The skin-friction reduction technique delays the shock-wave location, inducing a moderate pressure drag increase and a considerable increase in both lift and lift/drag ratio. As already observed in the context of chapter 2, by comparing the two cases at constant lift coefficient, the observed increase of lift is turned into a reduction of both angle of attack and total drag. In this case, however, no auxiliary simulations have been performed at lower AoA and the achievable ΔC_d can only be estimated. If the airfoil efficiency of the controlled case $L/D = 33.3$ is supposed to be unchanged when we reduce AoA to obtain the reference lift coefficient $C_\ell = 0.74$, the estimated total drag is $C_d = 0.0222$ leading to a total drag reduction higher than 10%. It is worth noticing that the real drag reduction is expected to be higher than this pessimistic estimation, since L/D usually increases by decreasing C_ℓ .

The present results, however, underline another significant outcome for transonic flows: friction reduction techniques can be used locally to produce a global gain. Indeed, since lift is almost entirely produced by the wing, this observation can be reasonably extended to the whole-aircraft configuration. By actuating a small portion of the suction side of the wing,

the overall aircraft lift (or drag) can be positively affected. This result is particularly appealing, especially considering that the "expected" benefits, as well as the actuation power consumption, of such a small portion, is almost negligible in the overall power budget of the whole aircraft.

4.6 Global power budget

It is therefore interesting to estimate the potential gain and power benefits in aeronautical applications. The present effect due to StTW, i.e. a total drag reduction of 1.5% and increase of lift of 10%, is therefore supposed to be valid over the 3D wing of the DLR-F6 aircraft presented in chapter 2, despite the different setup. Moreover, the impact of the total drag reduction $\Delta C_d = -1.5\%$ of the present wing slab, is supposed to be valid over the entire DLR-F6 wing; its impact on the total drag of the whole-aircraft configuration is estimated to around 0.5%. By comparing reference and controlled aircraft at the reference lift coefficient $C_\ell = 0.5$, by following the same procedure employed in chapter 2, an increase of lift of 10% can be translated in a reduction of the AoA , with an additional 6% of total drag reduction of the entire aircraft. The actuation power, however, should be taken into account in order to understand the achievable energy savings. The power required by StTW is estimated, as already done in chapter 2, as the 13% of the power spent due to friction drag. However, in this extrapolation, the actuated area is nearly one-tenth of the entire aircraft surface. With this estimation, the actuation power is around 0.5% of the power spent due to the total drag, and it is almost negligible in the whole-aircraft power budget. This estimation suggests that by actuating a small portion of the wing surface, a net power savings around 6% can be achieved, even for the whole-aircraft configuration.

This extrapolation ignores the deep differences between a wing slab and the 3D wing as well as the low Reynolds number, however, it gives an estimation of the achievable global impact of StTW, when applied locally. It is worth noticing that this results derives from the first preliminary investigation of StTW applied over a transonic wing slab, and it is performed without a specific optimisation of the several parameters in play, that could drastically improve the overall performances.

4.7 Conclusions

Direct Numerical Simulations of the transonic flow field around an airfoil have been carried out to understand how skin-friction drag reduction

affects the global aerodynamic forces. Numerical tripping downstream the leading edge forces the flow field to become turbulent. The airfoil examined, the V2C supercritical airfoil, presents, in the reference case, a single normal shock-wave and no transonic buffet occurs. The flow is modified by a direct implementation of the spanwise-forcing technique (streamwise-travelling waves of spanwise wall velocity, or StTW) known to reduce friction drag. The actuator is located over a limited portion of the suction side of the wing only.

The StTW is observed to reduce friction and to influence the shock-wave boundary layer interaction, in such a way that the shock-wave is deferred downstream. The overall drag is reduced by 2%, while changes on pressure field increase lift by 10%. Furthermore, the overall wing efficiency, defined by the lift/drag ratio, is enhanced by 12%.

The qualitative changes on the aerodynamics forces, as well as the shock-wave delay agree with previous RANS-based works. Present results, however, suggest a further meaningful outcome. The application of StTW over a limited portion of the suction side of the wing produces a considerable increase of the overall wing lift. If we extend the actuated wing behaviour to the whole-aircraft configuration, friction reduction techniques can be used over a confined portion of the wing to produce a global gain.

It is not immediate, however, to generalize these preliminary results for practical applications, since several questions are still open. The boundary layer around the airfoil V2C at the employed Reynolds number is not fully turbulent. Because of the transitory state of the boundary layer, the effect of StTW can be different than it would be over a fully turbulent airfoil, with a spurious alteration of the shock-wave boundary layer interaction. In this context, the numerical tripping plays a critical role; both the tripping strategy itself and its distance from the actuator could strongly affect the overall picture.

In addition, actuation is observed to induce a wide separation bubble that could affect the entire flow field. Further investigations are needed to verify whether the shock delay is present even in attached flows, in analogy with the study of geometry G_2 in the context of chapter 3. Lastly, in order to rigorously single out the influence of StTW on the shock-wave boundary layer interaction, the actuator efficiency as well as its effect on lift coefficient should be compared with the subsonic duplicate of the present study.

Works to extend this preliminary investigation are underway.

Part II

Wall friction: manipulation and prediction

CHAPTER 5

WALL-NORMAL JETS FOR SKIN-FRICTION REDUCTION

Science is universal and unifying: we are all made of the same elementary particles, and scientific knowledge has no passport, no gender, no race and no political party.

FABIOLA GIANOTTI

THIS chapter aims to investigate the potential benefit of a relatively new actuator concept, based on non-uniform unsteady blowing, currently studied at Harbin Institute of Technology in Shenzhen (HITSZ) wind tunnel laboratory. This project comes from my visiting experience at HITSZ, where I had the opportunity to cooperate with Professor Yu Zhou and his crew.

The blowing actuator, here investigated via Direct Numerical Simulations (DNS), relies on the hypothesis of counter-rotating vortices produced by the non-uniform jets, that interact with the wall-cycle and thus contribute in reducing friction. Numerical investigations assessed the presence of

these vortices; however, the impact of non-uniformity as well as unsteadiness on friction and turbulent activity is observed to be negligible. Finally, the effect of blowing actuator is analysed for an already spanwise-controlled channel flow.

5.1 Introduction

A possible strategy to reduce friction drag is the wall-normal injection of flow-mass. In the past years, the manipulation of turbulent boundary layer has been investigated via different configurations of blowing and/or suction with rectangular exit slot of finite streamwise extent.

The spanwise uniform and steady blowing actuator has been studied by Park and Choi (1999) via direct numerical simulations of a turbulent boundary layer, observing that friction reduction is followed by an overshooting downstream the slot. The same behaviour has been observed by Pamiès et al. (2007), while, more recently, Stroh et al. (2016) concluded that the overshooting downstream the control region depends on the streamwise extent of the slot and can be avoided with longer actuators.

The effect of the blowing unsteadiness has been investigated by Kim and Sung (2003) and Kim and Sung (2006), that simulated a pulsating forcing via DNS. They observed that the blowing frequency influences the turbulence activity and that the steady actuator is more efficient than the unsteady one. By increasing the jet's frequency, however, the efficiency of the steady case is recovered.

The effect of streamwise non-uniformity of the blowing actuator has been investigated by Kametani et al. (2016) via Large Eddy Simulations (LES). When several configurations are compared at constant flow-rate, friction is observed to be, on average, almost unaffected by the intermittency of the actuator. Taking into account the actuation cost, however, the simplest uniform blowing is observed to yield the highest net power savings.

Bai et al. (2014) from HITSZ obtained a high amount of local friction reduction via a spanwise-aligned array of piezo-ceramic actuators, employed to generate a transverse-travelling wave along the wall. A local friction reduction of 35% has been measured 33 wall units downstream the actuator, where a vertical shift in the mean velocity profile $\Delta B^+ \sim 4$ is present. They suggested that the transverse travelling wave created by the oscillating piezo-ceramic actuators generates a wavy layer of highly regularized vortices, as shown in figure 5.1. This layer reduces drag thanks to two different contributions. It behaves as a barrier between the coherent structures and the wall, interfering with the turbulence production

cycle, and significantly increases the dissipation rate, enhancing its drag-reducing effect.

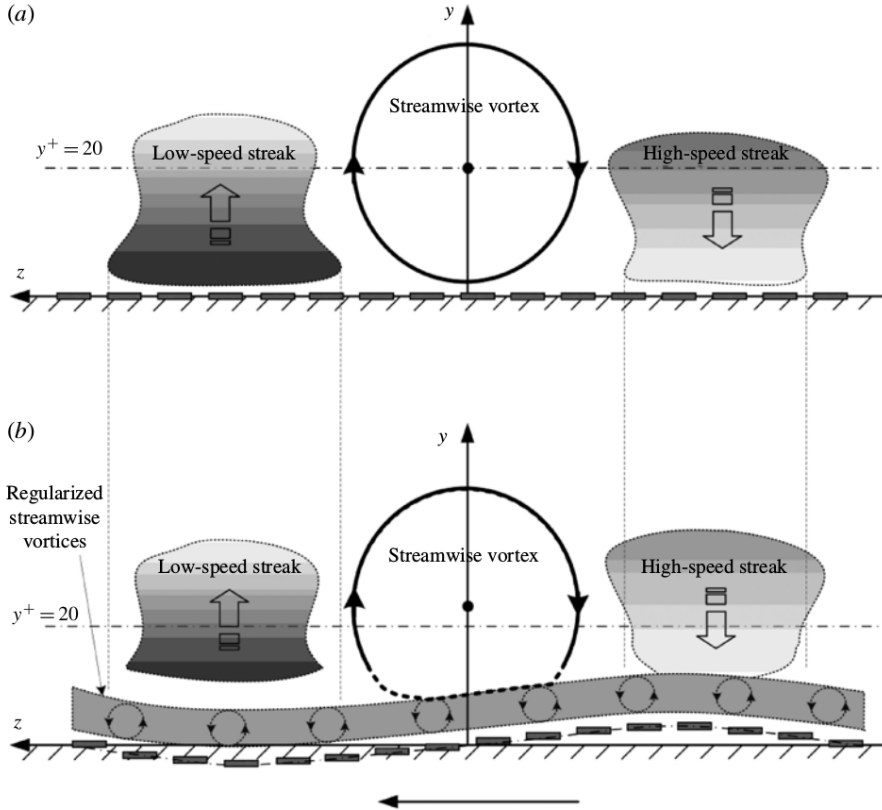


Figure 5.1: A schematic of the drag reduction mechanism: (a) control off; (b) control on. The transverse-travelling wave formed by the wall-based discrete actuators generates a layer of highly regularised streamwise vortices, which acts to weaken or even break the connection between the large-scale coherent structures and the wall. Taken from Bai et al. (2014).

The same physical mechanism is the main focus of the (yet unpublished) blowing actuator, based on spanwise non-uniform jets, that is numerically investigated in the present chapter. This actuator is being experimentally investigated at Harbin Institute of Technology in Shenzhen, China (HITSZ), where they observed a high amount of local friction reduction downstream the slits. They put forward the hypothesis that two different contributions produce the amount of local friction reduction obtained via non-uniform blowing. The first one is due to the wall-normal injection of null streamwise-momentum fluid; the second one is due to the layer of highly regularised streamwise vortices that interfere with the wall-cycle, as already observed by Bai et al. (2014). Direct numerical simulations are performed in this chapter in order to investigate the physical mechanism

behind friction reduction and to estimate the impact of these two different contributions.

Recently, a somehow similar investigation has been pursued by Abbassi et al. (2017), where a spanwise non-uniform actuator has been employed to reproduce the opposition-control strategy. The main focus of their experimental campaign, however, is the suppression of the large scale-structures and the surface of each slits, for example, is nearly 400 times (when expressed in viscous units) the one employed in this work. Nonetheless, it is worth noticing that they estimated the two contributions of local friction reduction, by performing a second experiment. The impact of the wall-normal injection of null streamwise-momentum fluid has been singled out by employing a desynchronised control scheme, and by comparison, they estimated that the opposition control strategy is responsible for nearly one-quarter of the amount of measured local friction reduction.

5.2 Simulations

The friction-reducing efficiency of a blowing control strategy is investigated via Direct Numerical Simulations (DNS) of a turbulent channel flow, with the actuator applied over the lower wall. The DNS are carried out with the same code and in similar setup of chapter 3. Figure 5.2 portraits a sketch of the computational domain, which is split into two streamwise-adjacent portions.

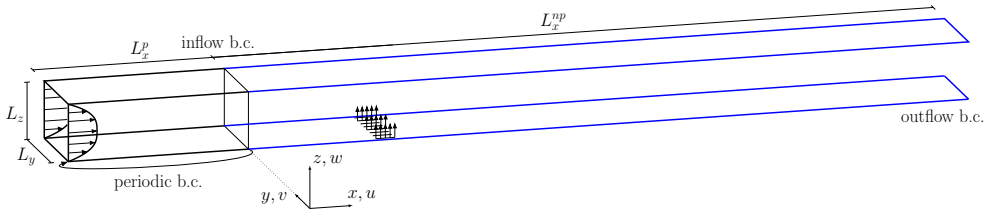


Figure 5.2: Sketch of the computational domain and the reference system. The streamwise-periodic upstream domain (black) provides the inflow boundary condition for the downstream one (blue) which includes the actuator.

The employed bulk Reynolds number is $Re_b = U_b h / \nu = 3173$, the same of chapter 3, and corresponds to a friction Reynolds number of $Re_\tau = u_\tau h / \nu = 200$ in the unforced portion of the domain. In these definitions h is half the distance between the walls, U_b is the bulk velocity and u_τ is the friction velocity. Unless otherwise noted (e.g. with the plus notation indicating viscous units), in the following, quantities are made dimensionless with h and U_b . The computational domain has dimensions

$(L_x^p + L_x^{np}, L_y, L_z) = (2\pi + 8\pi, \pi, 2)$ in the streamwise, spanwise and wall-normal directions respectively, with the lower wall placed at $z = 0$. The upstream domain, with streamwise length of $L_x^p = 2\pi$, has a spatial resolution of $(n_x, n_y, n_z) = (210, 384, 200)$ discretization points, and runs a standard periodic channel flow DNS, performed at Constant Flow Rate (CFR). The downstream portion has the same grid and domain sizes in the spanwise and wall-normal directions of the upstream one, to avoid interpolation. It starts at $x = 0$ and has streamwise extent of $L_x^{np} = 8\pi$, over which 840 discretization points are uniformly distributed. The spanwise resolution is tuned to accurately reproduce the thin actuator slits with uniform grid spacing $\Delta y = 0.008$, which corresponds to $\Delta y^+ = 1.6$ based on the inlet u_τ . Streamwise resolution is uniform in both portions of the domain at $\Delta x = 0.03$ or $\Delta x^+ = 6$. The wall-normal spacing is symmetrical with respect to the centerline. $\Delta z = 0.0015$ is adopted at the two walls, and corresponds to $\Delta z^+ = 0.3$. Then Δz gradually increases and the maximum value of $\Delta z^+ = 4$ is reached at the centerline.

Statistics are accumulated over a simulation time of $T = 1000$, after reaching statistical equilibrium, by employing two different strategies. Statistics on both walls and over a limited portion of the domain that includes the actuator, namely $1.5 \leq x \leq 9$ and up to the centreline, are run-time accumulated every time step, which is set at $\Delta t = 4.7 \cdot 10^{-3}$. A second database provides flow information for the entire channel, and is made by 3D flow fields saved every 10 time units.

Four different configurations of the blowing control strategy are studied in order to investigate both effects of unsteadiness and spanwise non-uniformity, at the same injection flow-rate. Blowing is achieved by the direct imposition of the vertical velocity at the wall, W_w . Streamwise and spanwise extents, as well as the injection parameters, are chosen in order to faithfully reproduce the physical actuator employed in HITSZ wind tunnel. The streamwise length of the control region is kept constant at $l_j^+ = 132$, located at $4.5 \leq x \leq 5.16$. Uniform actuators take up the entire span of the channel. Non-uniform actuators are composed by 48 spanwise-periodic slits of width $1.7 \cdot 10^{-2}$, which corresponds to $d_y^+ = 3.33$. The distance between two slits is three times wider than the slit itself, in such a way that for the streamwise actuator's extent, the total jet's surface S_j is one-quarter of the entire surface S_{tot} . A sketch of the non-uniform actuator is portrayed in figure 5.3. In unsteady simulations, the temporal evolution of the jet aims to reproduce a square wave with duty cycle of 0.2 and frequency $f = 1.75$, which correspond to $f^+ = 0.14$. Moreover, in order to faithfully mimic the physical actuator, the square wave is here bevelled by two ramps.

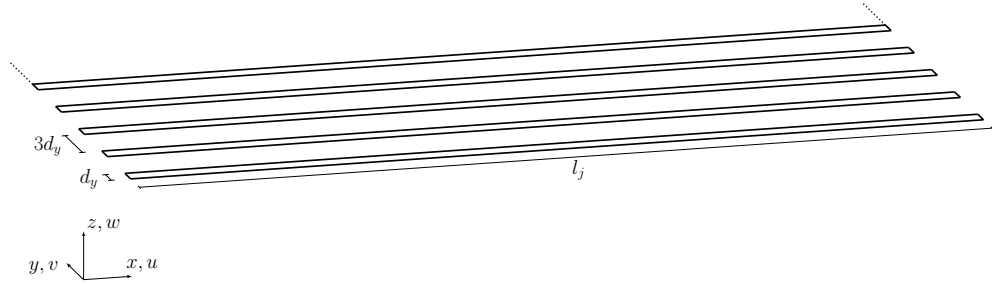


Figure 5.3: Sketch of non-uniform blowing actuator.

In streamwise periodic simulations that aim at studying a blowing actuator, the flow-rate is commonly kept constant by applying suction on the upper wall. This strategy, however, could affect the entire flow field up to the lower wall. In order to reduce its influence on the blowing region, the upper wall is non-actuated in the present work. The flow-rate downstream the actuator is therefore 0.7% higher than the imposed one in the CFR condition; slight differences could, therefore, be observed in the flow statistics with respect to the periodic portion of the domain.

The control parameters are summarised in table 5.1, where W_w^+ , in unsteady simulations, corresponds to the maximum velocity of the bevelled square wave.

Simulation	S_j/S_{tot}	f^+	W_w^+
U-S	1	—	0.355
NU-S	0.25	—	1.42
U-NS	1	0.14	1.775
NU-NS	0.25	0.14	7.1
StW	0.25	—	1.42

Table 5.1: Details of the blowing strategy employed. Here S_j/S_{tot} represents the fraction of the spanwise width covered by jets (unitary for uniform blowing); f^+ is the forcing frequency of the unsteady cases, W_w^+ is the blowing wall-normal velocity. The case StW investigates the blowing actuator over a spanwise-controlled wall by a standing wave with parameters $(A^+, \kappa_x^+) = (12, 0.01)$.

A fifth simulation investigates the effect of blowing over an already controlled wall by a standing wave of spanwise velocity (StW), i.e. a streamwise-travelling wave with null temporal frequency, defined by the equation:

$$V_w(x, t) = A \sin(\kappa_x x) \quad (5.1)$$

where V_w is the spanwise velocity at the wall, A is its maximum amplitude, and κ_x represents the spatial frequency of the wave. The spanwise wall

velocity is set at zero for the entire streamwise extent of the blowing actuator.

The non-uniform actuator has already been investigated in the experimental campaign conducted at HITSZ wind tunnel. At the measurement point x_m , located 33 wall units downstream the control region, an amount of friction reduction around 70% has been observed with both steady and unsteady forcing. Direct numerical simulations are performed in order to further investigate this hypothesis.

Experiments, however, are conducted in a developing boundary layer, with no upper wall, and at higher Reynolds number around $Re_\tau = 500$. Moreover, the present channel flow imposes periodicity in the spanwise direction, while the physical actuator has a finite spanwise extent and 3D effects could arise at its tips. Quantitative differences are, therefore, expected.

5.3 Spanwise non-uniformity

The main goal of this project is to numerically verify the presence of highly regularised streamwise vortices over the non-uniform actuators, and further estimate their impact in friction and turbulent activity. In order to single out how streamwise vortices affect the flow field, the non-uniform steady actuator (NU-S) is compared with the uniform steady case (U-S), performed at the same injection flow-rate. When a uniform slot is applied, no streamwise vortices can be produced by the blowing, and the obtained amount of friction reduction is only due to the wall-normal injection of mass with null streamwise-momentum.

To begin with a qualitative view of the actuators, figure 5.4 shows an instantaneous colour plot of the wall-normal velocity component in the plane $x = 4.9$ passing through the control region. Only a localized portion of the spanwise extent is shown, from the lower actuated wall, located at $z = 0$, up to $z = 0.15$ which corresponds to $z^+ = 30$ when expressed in viscous units by using the inlet u_τ . The first panel portrays the uniform actuator U-S, where w at the wall is constant at $w = 0.022$, which corresponds to 0.355 times the inlet u_τ . For $z \geq 0.1$ the presence of turbulent structures is detected by the positive/negative wall-normal velocity areas. The non-uniform actuator NU-S is shown in the lower panel; the presence of the slits can be appreciated by the high wall-normal velocity $w = 0.09$ at the lower plane. Above the solid wall, a slight negative wall-normal velocity area, underlined by the dotted lines, assess the presence of recirculation between two consecutive jets.

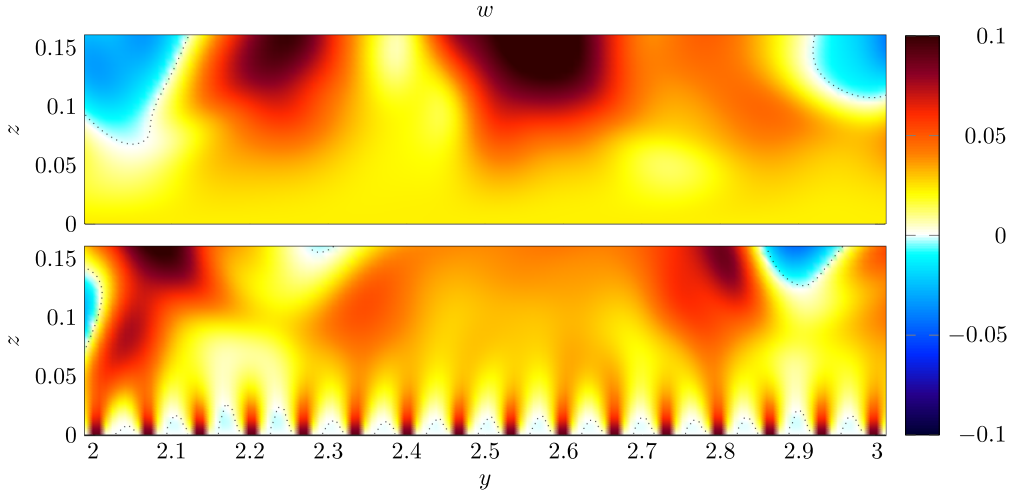


Figure 5.4: Colour plot of an instantaneous wall-normal velocity field, in the plane $x = 4.9$, passing through the actuator for the cases U-S (top) and NU-S (bottom). Contour lines (dotted) are drawn for $w = 0$.

The jet-induced recirculation is further observed in figure 5.5, which portrays an instantaneous flow field of simulations U-S (top) and NU-S (bottom). Here, isosurfaces of the streamwise component of the rotational velocity ω_x depict the presence of regular counter rotating vortices above the non-uniform actuator, while they are absent over the uniform one. Moreover, the qualitative impact of the blowing on turbulent structures can be appreciated by observing the isosurfaces of the intermediate eigenvalue λ_2^+ of the velocity gradient tensor (Jeong and Hussain, 1995), non-dimensionalised by using the inlet u_τ , and colour-coded with the wall-distance z^+ . Above the non-uniform jet, turbulent structures appear to be reduced, while a slight increase of turbulent activity can be appreciated downstream the actuators. Figure 5.5 assesses the presence of highly regularised streamwise vortices over the non-uniform actuator. Moreover, a friction drag reduction of 68% is computed at the measurement point x_m , showing a good agreement with experimental data and suggesting that the blowing actuator is successfully reproduced by the present DNS.

Figure 5.6 shows instantaneous colour plots of the streamwise velocity component in the plane $z = 0.05$, which corresponds to $z^+ = 10$ when expressed in viscous units by using the inlet u_τ , comparing the cases U-S (top) and NU-S (bottom); the vertical bands show the beginning and the end of the actuator. The elongated streaks of high/low streamwise velocity are clearly visible in both cases, far from the actuators. Above the uniform jet, low-momentum fluid is upward-pushed, drastically reducing the streamwise velocity. Above the non-uniform actuator, at this short

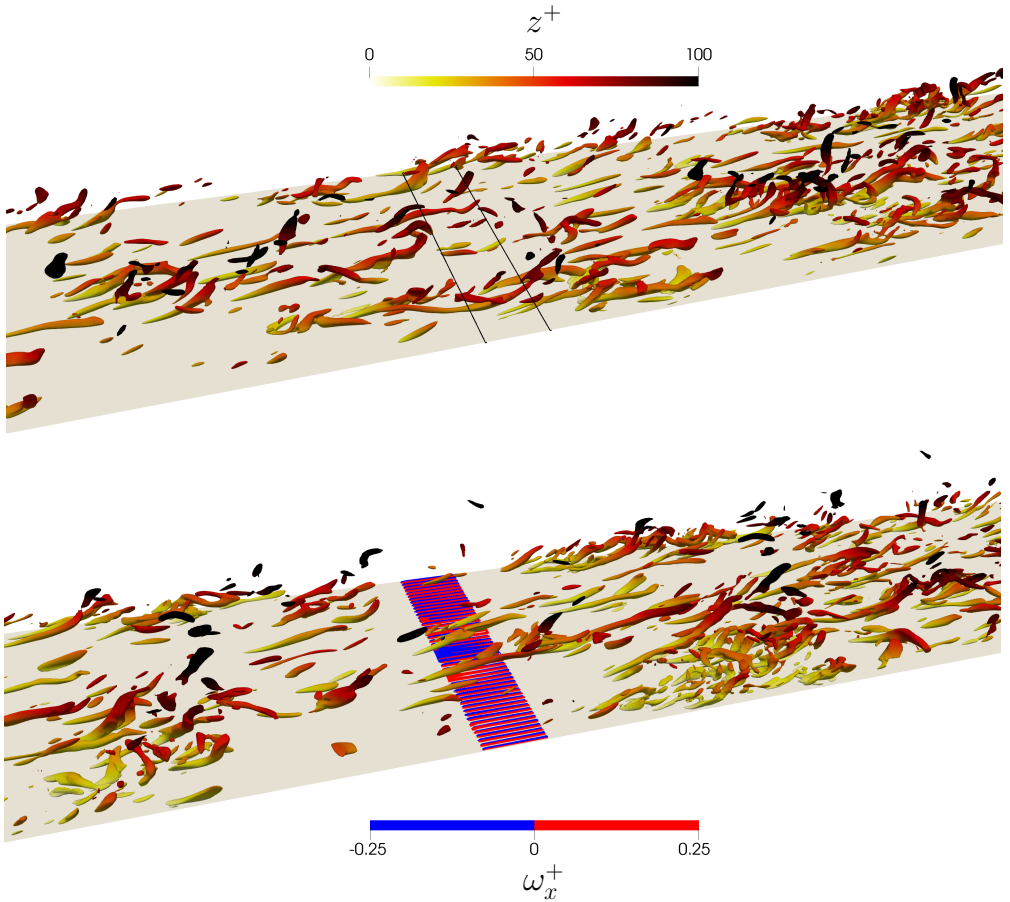


Figure 5.5: Isosurfaces of $\omega_x^+ = \pm 0.25$ (red and blue) that identify the regularised streamwise vortices and isosurfaces of $\lambda^+ = -0.02$ (colour-coded with the wall-distance z^+) for an instantaneous flow field of case U-S (top) and NU-S (bottom). The black lines denote the location where forcing starts and ends.

wall-distance, the slits-induced spanwise modulation of u is still visible. The qualitative effect on the flow field, however, appears to be similar to case U-S.

Figure 5.7 plots a vertical plane with a colour map of the mean vertical velocity component $\langle w \rangle$ for a localized portion of the domain which includes the control region, namely $2.6 \leq x \leq 7.8$; the actuator is identified by the horizontal black line placed at $z = 0$. The operator $\langle \cdot \rangle$ implies averaging over time and the homogeneous spanwise direction. In the non-uniform case, a spatial phase-averaging procedure is employed in the spanwise direction, since slits are periodically repeated at the same distance. Two vertical planes are investigated in the following, the first one is located

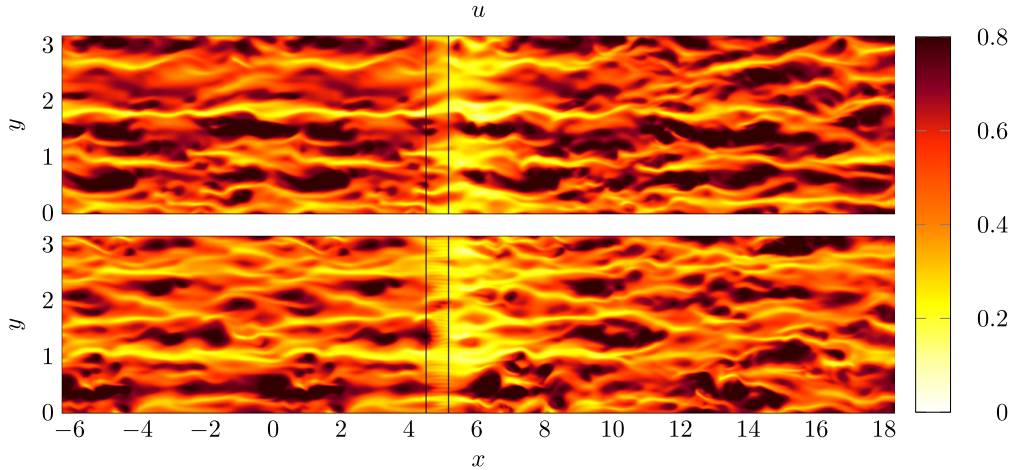


Figure 5.6: Colour plot of an instantaneous streamwise velocity field, in the plane $z = 0.05$, for the case U-S (top) and NU-S (bottom). Flow is from left to right, and the downstream non-periodic section starts at $x = 0$.

equidistant from two slits and the second one passes through the centre of the slit.

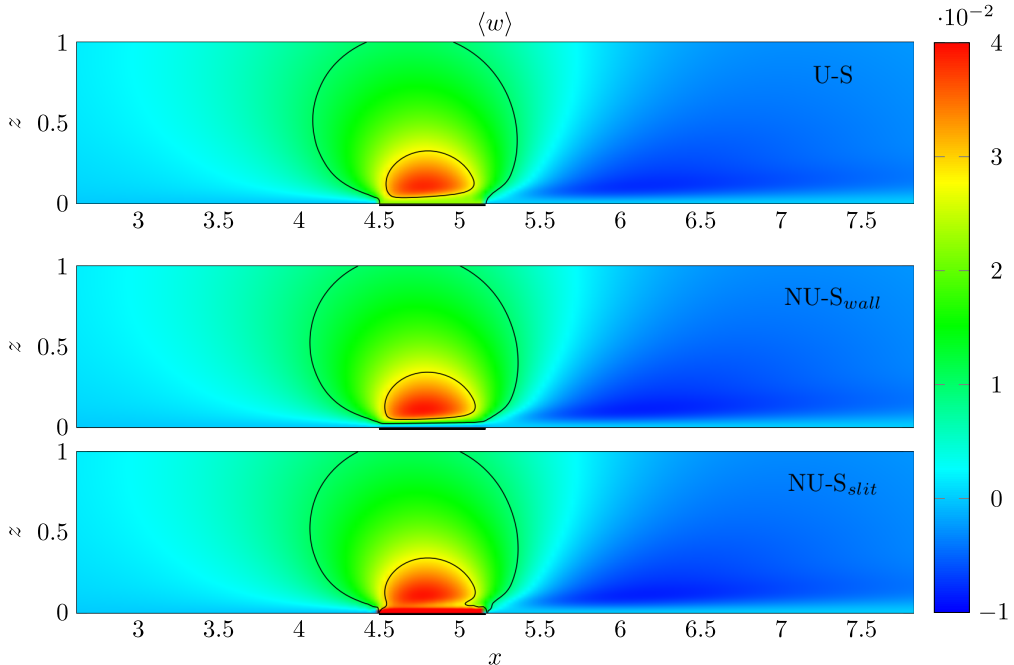


Figure 5.7: Colour plot of the mean wall-normal velocity $\langle w \rangle$, for case U-S (top) and NU-S (bottom). The latter is shown over two planes: above the wall (second panel) and above the slit (third panel). Contour lines are drawn for $\langle w \rangle = (0.01, 0.028)$.

In case U-S, the area of high wall-normal velocity, underlined by the contour line at $\langle w \rangle = 0.028$, is located far from the wall and it is due to the mean velocity vector that is rotated upward by the jet. The area itself shows a positive tilt angle. Almost negligible differences are detected when non-uniform blowing is employed. Except for the area very close to the actuator, the three panels appear almost identical, meaning that the non-uniform jet quickly spread out and immediately recover the uniform blowing behaviour.

Friction coefficient c_f , defined as in equation 3.4, is plotted in figure 5.8 for cases U-S and NU-S, over both walls. Here c_f is computed by averaging in time and spanwise direction even for case NU-S since negligible variations are observed in spanwise direction. The control region extremes are identified by vertical dotted lines. Uniform blowing strongly reduces friction both upstream and downstream the actuator. A significant overshooting starts around $x = 8$, i.e. 600 viscous units downstream the actuator, and last after a long distance, deteriorating the overall performances of the channel. On the upper wall, on the other hand, the actuator induces a non-negligible increase of friction.

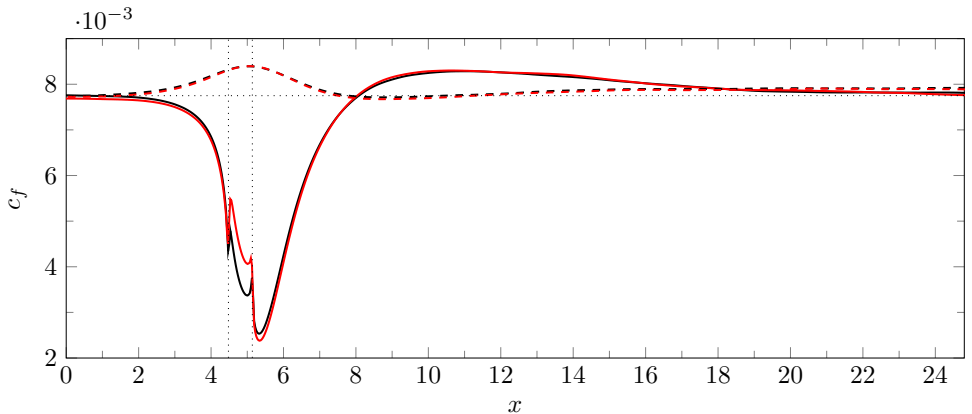


Figure 5.8: Skin-friction distribution $c_f(x)$: cases U-S (black) and NU-S (red) over the lower (solid lines) and upper (dashed lines) walls.

For both walls, the comparison between case U-S (black) and NU-S (red) shows minimal differences, except for the control region where the physical meaning of a friction coefficient is not trivial. The agreement between the two cases, however, suggests that the direct influence of the highly regularised streamwise vortices on friction distribution is almost negligible.

In order to assess the influence of the streamwise vortices in turbulent activity, figure 5.9 shows the turbulent kinetic energy $k = 1/2\langle u'_i u'_i \rangle$ for the same three planes of figure 5.7. In the uniform case (top) two areas of

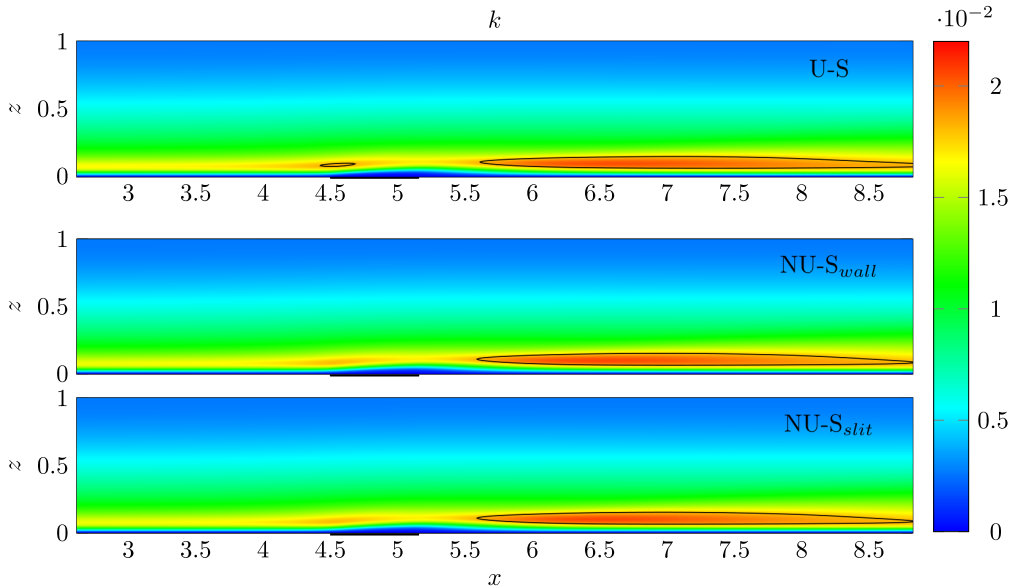


Figure 5.9: Colour plot of the turbulent kinetic energy, in outer units. Panels as in figure 5.7. Contour lines are drawn for $k = 0.018$.

high k are observed: one just ahead of the control region, and the other, more intense, immediately downstream. Even turbulent activity, the main focus of the physical hypothesis put forward by Bai et al. (2014), appears to be poorly affected by the spanwise non-uniformity. Differences induced by the non-uniformity of the jet appear to be negligible, except for the first positive peak upstream the actuator which is slightly reduced in both planes of case NU-S. The distribution of k reinforces the idea put forward in the context of figure 5.8, that streamwise vortices have a negligible impact on the flow field, and the amount of friction reduction is only due to wall-normal injection of null streamwise-momentum fluid.

5.4 Unsteadiness

The effect of unsteadiness is investigated in order to confirm that, by using high-frequency blowing, the steady actuator behaviour is recovered. Because of the negligible influence of the spanwise non-uniformity, observed in the previous section, the effect of the forcing unsteadiness is studied for the uniform actuator only, by comparing cases U-S and U-NS.

The forcing velocity over one blowing period is plotted in figure 5.10. The ideal square wave is bevelled by two ramps, in order to faithfully reproduce the physical actuator dynamics, while preserving the same flow rate of the

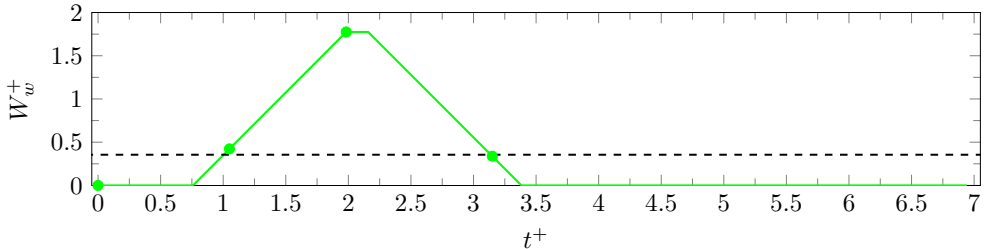


Figure 5.10: Temporal evolution of one period of the unsteady actuator U-NS (green). Four points underline the instants investigated in the following. The black dashed line denotes the steady forcing of case U-S.

steady case. One forcing period is computed in 120 time-steps $\Delta t^+ = 0.06$. The four point highlighted in figure 5.10 are further investigated in the following. The black dashed line, on the other hand, depicts the steady forcing of case U-S.

Figure 5.11 plots a vertical plane with a colour map of the wall-normal velocity component $\langle w \rangle$, for the localized portion around the jet of case U-NS only. The mean flow field is computed by averaging in the homogeneous spanwise direction, and by employing a phase averaging procedure in time. The four panels refer to the marked moments of figure 5.10, at zero blowing velocity, during acceleration, at maximum velocity and during deceleration, respectively. To ease the comparison with case U-S, already shown in figure 5.7, contour lines are drawn for this case too (dashed), over the four panels. Due to the high blowing frequency of the actuator, even at the beginning of the period (first panel), significant values of wall-normal velocity are still present, and the flow field is influenced even above the centreline. During the accelerating and decelerating phases, in the second and fourth panels, the high-velocity area is qualitatively different compared to the steady case, even if the forcing velocity is almost coincident. In the accelerating phase, this area is moved downstream compared to case U-S, with an almost negligible tilt angle. During deceleration, on the other hand, this area is moved upstream with a tilt similar to the steady case. The third panel shows the high wall-normal values, that saturate the adopted map scale up to $z = 0.5$.

Figure 5.12 plots the friction coefficient distribution for cases U-S (black) and U-NS (green); in order to assess the mean benefit, friction is averaged over time even, for the unsteady case. When unsteady blowing is applied, differences appear to be minimal, with a friction reduction slightly higher immediately downstream the actuator and an increased overshooting amplitude. However, these little differences could be due to a finite averaging

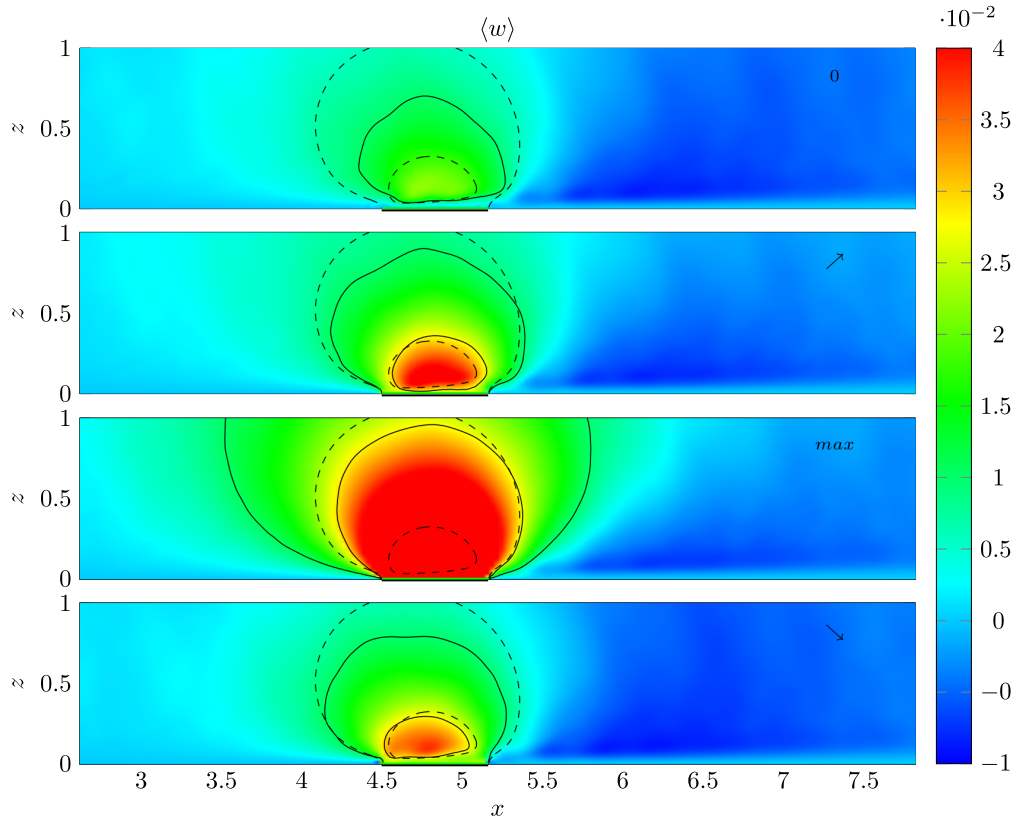


Figure 5.11: Colour plot of the mean wall-normal velocity $\langle w \rangle$ for case U-NS in four moments of the period: zero W_w , acceleration, maximum W_w and deceleration respectively. Contour lines are drawn for $\langle w \rangle = (0.01, 0.028)$ for case U-NS (solid lines) and compared to the steady case U-S (dashed lines).

time.

Turbulent kinetic production P , defined as in equation 3.12, strongly varies along the forcing period. Despite such variations, the unsteady dynamic is so fast that turbulent kinetic energy is similar to the steady case, and it is therefore not shown. P , on the other hand, is portrayed in figure 5.13 for both steady (top) and unsteady (bottom) cases. In case U-S, two areas of high P are present, one just ahead of the control region, and the other, more intense, immediately downstream. When the unsteady jet is employed, bubbles of high turbulent kinetic production are generated at the beginning of the actuator and are then convected downstream by the mean flow field. Their separation is, in fact, consistent with the length travelled by a streamline at the same wall distance. In the fourth panel, where W_w is maximum, turbulent production is strongly inhibited above the slot, while it increases immediately upstream and downstream the ac-

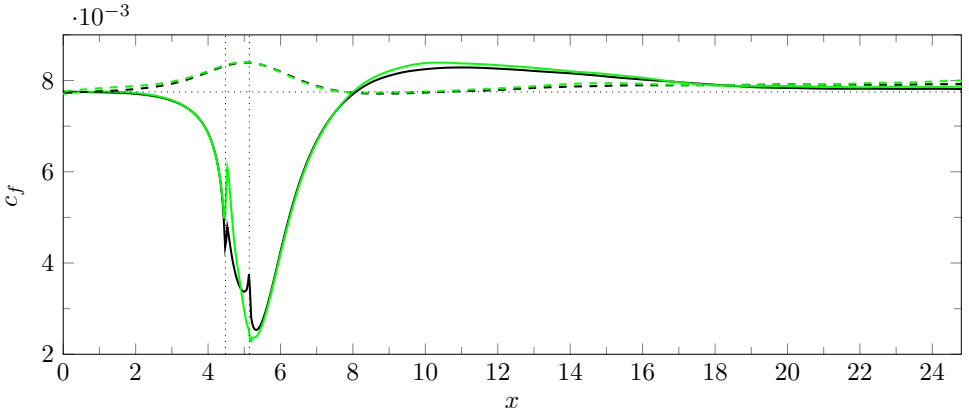


Figure 5.12: Skin-friction distribution $c_f(x)$: cases U-S (black) and U-NS (green) over the lower (solid lines) and upper (dashed lines) walls.

tuator. In agreement with wind tunnel experiments, negligible differences are present in friction distribution, compared to the steady case.

When the non-uniform and unsteady (NU-NS) blowing is employed, the same qualitative behaviour is observed compared to simpler setups. The mean friction distribution almost overlap with the U-S case, except for a slightly increased overshooting. The temporal evolution of the k and P is very similar to the U-NS case, confirming that non-uniformity negligibly affects the turbulent activity.

5.5 Global power budget

Since the employed flow control strategy is a local active technique, the efficiency of the actuators should be compared by taking into account the friction changes of the whole domain and the power required by the actuators P_{req} . Moreover, even though the same injection flow rate has been employed among the four cases, it is worth noticing that the power required by a steady blowing actuator is $P_{req} = (\frac{1}{2}S_j W_w^3)$ and strongly depends on the forcing velocity. In the simpler U-S case, the amount of total friction reduction of the lower wall, computed over the entire non-periodic domain, is slightly higher than 3%, since the overshooting deteriorates the overall performances. Moreover, the power required by the actuator is $\sim 0.004\%$ of the power spent due to the friction drag, and it is therefore negligible, as reported in table 5.2

When the non-uniform actuator is employed, the increase of W_w drastically raises P_{req} , although it is still lower than 0.1% with a P_{net} almost

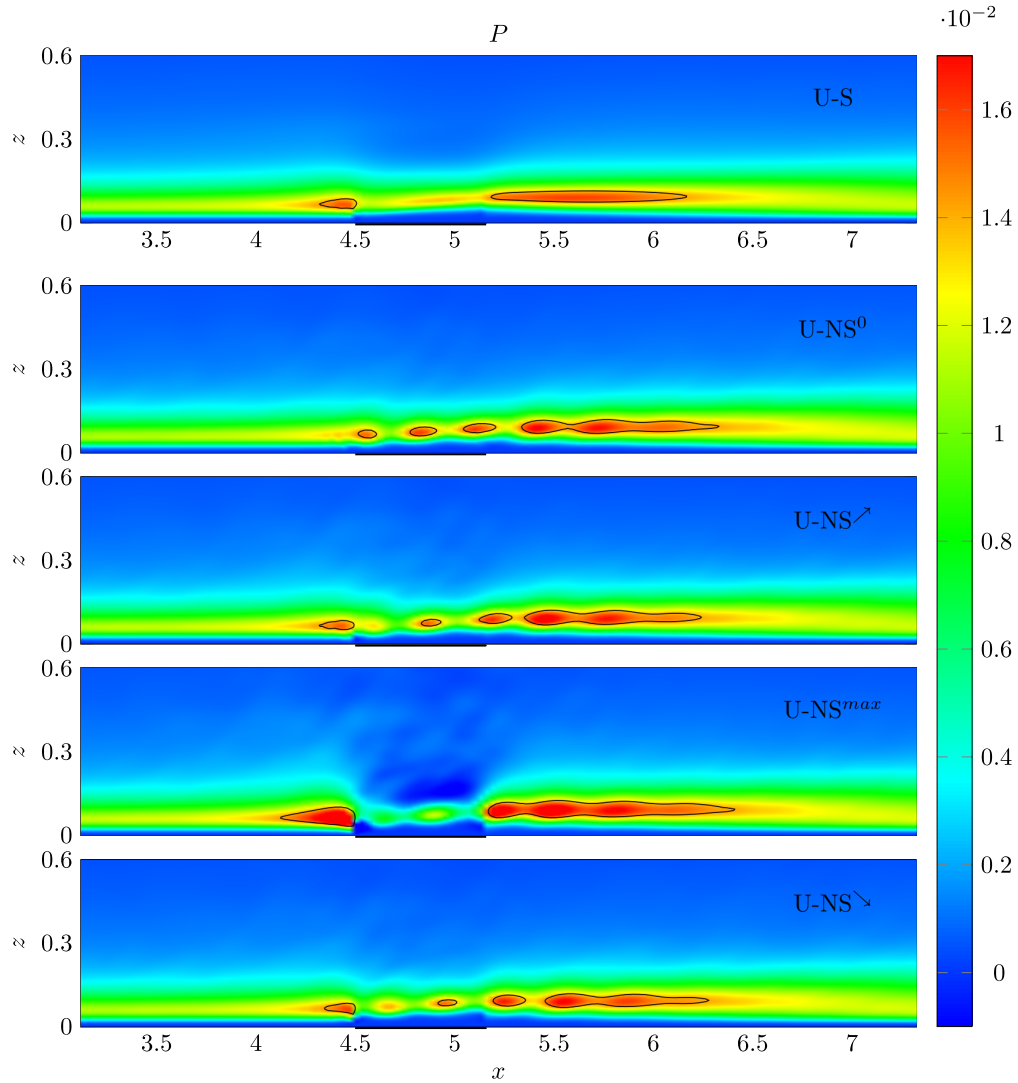


Figure 5.13: Colour plot of the production P of turbulent kinetic energy, for case U-S (top) and U-NS (bottom). The latter is shown in four instants of the forcing period, with panels as in figure 5.11. Contour lines are drawn for $P = (0.014)$.

coincident with the U-S case. In the U-NS case, P_{sav} is slightly lower than 3%, due to the increased overshooting observed in figure 5.12, while the mean actuation power, averaged over one blowing period, is similar to the one observed in case NU-S.

In the NU-NS case, however, due to the increased overshooting, the overall friction drag reduction is slightly lower than 2%. The actuation power P_{req} , averaged over one forcing period, is around 0.7% of the total power, with a net power saving almost halved.

	U-S	NU-S	U-NS	NU-NS
$P_{sav}\%$	3.29	3.23	2.8	1.72
$P_{req}\%$	0.0037	0.06	0.04	0.67
$P_{net}\%$	3.29	3.17	2.76	1.05

Table 5.2: Power budget for the four cases. P_{sav} is the power saved thanks to the reduction of friction drag. P_{req} is the power required for actuation, and $P_{net} = P_{sav} - P_{req}$ represents the net balance. Figures are for the lower wall only and are expressed as a percentage of P_{tot} , which is the power required to overcome the drag produced by the lower wall.

It is worth noticing that the power budget here reported has been computed without taking into account that the flow rate inside the channel changes due to the actuator. The P_{sav} is computed, by using the most conservative strategy, as a difference between the actuated wall and the non-actuated plane of the periodic domain. The increase of flow rate is lower than 1% and its influence on the power budget is estimated to be of the same order of magnitude. This analysis assesses that, from the energetic point of view, the uniform steady blowing is the most efficient strategy.

However, when a blowing actuator is installed in practical applications, for example over an aircraft wing, additional contributions should be considered. Any practical issue about installation and increase of weight is not addressed in this estimation. However, if the air needed by the actuator is taken from the external air, its streamwise velocity must be slowed down by an additional streamwise force, i.e. drag, that influences the force and power budget. By neglecting the friction contribution inside the ducts downstream the air intake, the drag needed to slow down the air is given by the momentum conservation: $D_{in} = \frac{1}{2}\rho S_{in} U_{in}^2$, where U_{in} is the intake velocity of the air and S_{in} is the intake surface. In external flows U_{in} coincides with the flight velocity; by using the channel flow behaviour as a representation of external flows, however, U_{in} can be considered equal to the bulk velocity U_b . The intake surface S_{in} is consequently scaled to obtain the same flow-rate of the blowing actuator. With this estimation, the drag due to the need to slow down the air corresponds to 7.5% of the overall friction drag caused by the lower wall. With this estimation, for the most efficient uniform and steady actuator U-S, the overall drag reduction and the net power saving are negative at -4.2%.

5.6 Combination of jets with spanwise forcing

The non-uniform steady actuator is further studied over an already controlled channel in simulation StW. Here a stationary-wave of spanwise wall velocity is applied over the lower wall; as in chapter 3, StW is imposed over the periodic upstream portion of the domain too. The spanwise wall velocity is manually set at zero where the blowing actuator takes place.

Figure 5.14 shows the mean wall-normal velocity for simulation StW, over two different vertical planes. The first one is located equidistant from two slits and the second one passes through the centre of the slit. To ease the

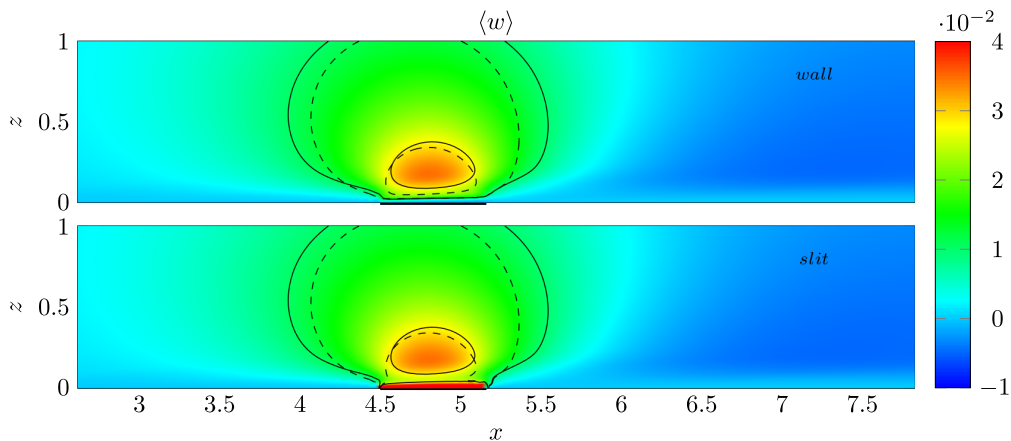


Figure 5.14: Colour plot of the mean wall-normal velocity $\langle w \rangle$, for case StW over two planes: above the wall (first panel) and above the slit (second panel). Contour lines are drawn for $\langle w \rangle = (0.01, 0.028)$ for case StW (solid lines) and compared to the steady case NU-S (dashed lines).

comparison with the case NU-S, already shown in figure 5.7, contour lines are drawn for this case too (dashed). In the spanwise-forced case, the jet is spread at a wider streamwise extent, while the high- w area is pushed at higher distance from the wall, and presents lower values. Above the slit, jet influence seems to be confined in a very thin layer close to the wall, in such a way that the high- w area is split into two different regions.

Friction coefficient for both simulations is plotted in figure 5.15.

When StW is applied, c_f shows both quantitative and qualitative differences. Spanwise forcing yields at the inlet an amount of friction reduction of 40%, in agreement with existing information (e.g. Gatti and Quadrio, 2016). The blowing actuator induces a further 55% of friction reduction at the measurement point x_m . Moreover, the friction recovery downstream the jet is decelerated by StW; the reference inlet value of c_f is recovered 1400 wall units downstream the actuator, i.e. 800 wall units after case

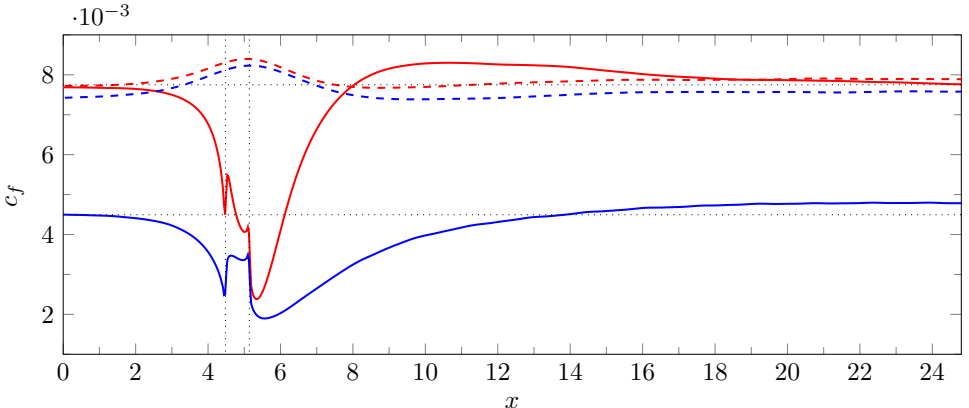


Figure 5.15: Skin-friction distribution $c_f(x)$: cases NU-S (red) and StW (blue) over the lower (solid lines) and upper (dashed lines) walls.

NU-S. Differently from chapter 3, a long overshooting is present over the spanwise-forced wall, in such a way that the domain length is not enough to allow a full recovery. In agreement with chapter 3, StW applied over the lower wall induces a 4% of friction reduction on the upper, non-actuated wall. The effect of blowing on the upper wall, however, is qualitatively unchanged.

The combination of the two flow control strategies is further investigated by plotting the turbulent kinetic energy k in figure 5.16. Only the slice above the wall is shown, since negligible variations are found in spanwise direction. The ease the comparison, the first panel portraits the case NU-S, already shown in figure 5.9. Spanwise forcing induces both qualitative and quantitative differences; note the halved colour-map scale with respect to the first panel. At the inlet, in agreement with the observations by Quadrio and Ricco (2011), far from the jet, the maximum value of k (measured in outer units) is reduced by StW and displaced at higher wall distances. The interaction with the jet appears to be consistent with case NU-S, with a first peak of k ahead of the actuator, and a more intense peak downstream. However, as highlighted by countour lines, k slowly increases downstream the actuator, showing larger values for $x > 7$.

Turbulent kinetic energy is therefore further investigated over a wider area. Because of the quantitative difference between the two cases, the comparison is performed by introducing a new quantity δk , as follows

$$\delta k = \frac{k}{\max(k^p)} - 1, \quad (5.2)$$

where $\max(k^p)$ is the maximum value of k computed in the lower half

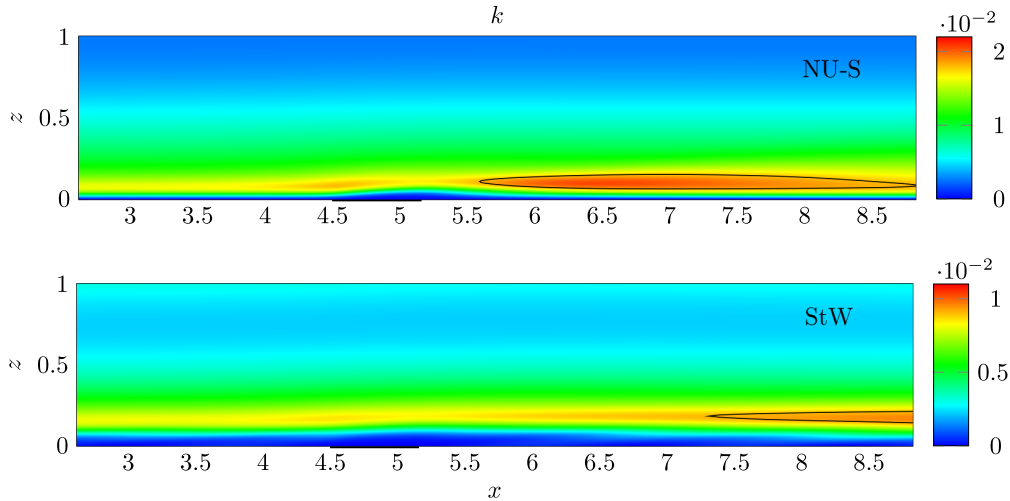


Figure 5.16: Colour plot of the turbulent kinetic energy, in outer units, for cases NU-S (top) and StW (bottom). Note the different colour-map scale. Contour lines are drawn at $k = 0.018$ for case NU-S and at $k = 0.009$ for case StW.

of the periodic portion of the domain. Positive values of δk represent areas where the turbulent kinetic energy is made higher by the jet than the flat channel maximum $\max(k^p)$. In figure 5.17, δk is portrayed with a divergent colour map centred around zero, to ease the detection of positive areas. Of course the scale is saturated for negative values, since δk tends to -1 at the centreline. Previous mean plots derive from a run-time accumulation of statistics, computed over a limited portion of the domain that includes the blowing actuator. The quantity shown in figure 5.17, on the other hand, is computed by analysing the database of flow fields saved every 10 time units. Thus spurious oscillations are present due to

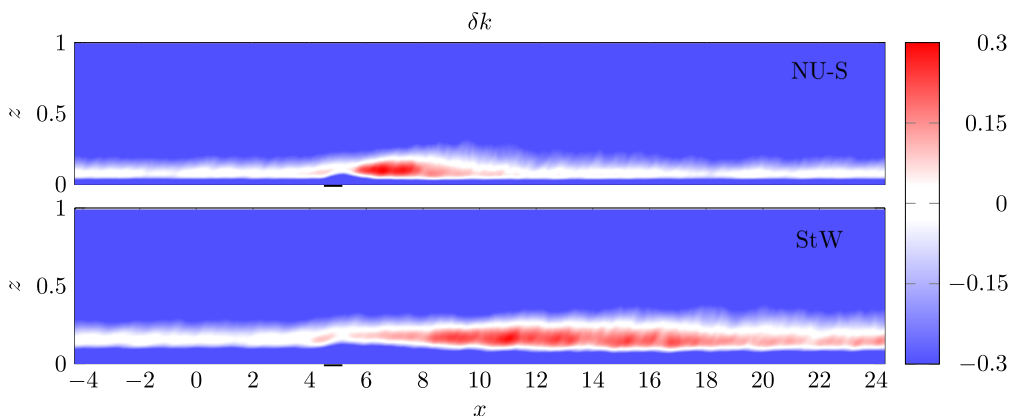


Figure 5.17: Colour plot of δk for case NU-S (top) and case StW (bottom).

the limited number of samples.

In agreement with figure 5.16, in case NU-S, k slightly increases before the actuator, whereas a more intense peak of k starts downstream the jet. The maximum value of the turbulent kinetic energy is 30% higher than $\max(k^p)$. For $x > 12$, the periodic wall-normal distribution of k is recovered, since the maximum value of δk is around zero. This plot is in agreement with the overshooting location and the following smooth recovery of the friction coefficient, shown in figure 5.15. In the spanwise-forced case, a slight increase of k is present before the jet too. Downstream the slits, however qualitative differences are induced by the stationary waves. δk slowly increases for $x > 5$, reaching its maximum, around 30% as in case NU-S, at $x = 9$. This area of high- δk is wider than in case NU-S and the jet-induced increase of turbulent kinetic energy is detected for the entire domain length, in agreement with friction distribution.

5.7 Conclusions

The efficiency of friction-reducing blowing actuators is investigated via direct numerical simulations, shedding light on the influence of unsteadiness and non-uniformity.

Non-uniform blowing yields nearly 70% of friction reduction at the measurement point, in agreement with experimental data, suggesting that the present DNS successfully reproduces the actuator. The presence of regularised streamwise vortices over non-uniform actuator has been verified. However, their impact on the friction-reducing mechanism is observed to be negligible, since uniform blowing yields the same amount of friction reduction. Jets unsteadiness too seems to affect both friction distribution and turbulent activity marginally.

When blowing is applied over an already spanwise-controlled wall, blowing yields a further 55% of friction reduction at the measurement point. Meoreover, downstream the jet the recovery is slower, while a consistend overshooting is present for the entire domain length, deteriorating the overall performances.

CHAPTER 6

LINEAR RESPONSE OF TURBULENT FLOWS OVER GENERIC BUMPS

Just because *we* don't understand something
doesn't mean that it's nonsense.

LEMONY SNICKET

THIS chapter deals with the evergreen problem of the flow field response to a smooth variation in bottom topography. Even if this topic caught the attention of researchers starting from the end of '50s with the seminal work of Benjamin (1959), it still represents an open challenge. The recent review by Belcher and Hunt (1998) starts, nonetheless, quoting the Bible: "I will lift up mine eyes unto the hills from whence cometh my help".

Two possible solutions of the problem have been recently proposed by Luchini and Charru (2017) and Luchini and Charru (2019). The accuracy of these theories is investigated in the present chapter.

6.1 Introduction

The linear response of a turbulent flow over a smoothly varying bottom wall is an important topic that is particularly relevant in geophysical studies, e.g. flow over hills, waves, dunes, and for the evolutionary growth of the waves and dunes themselves. The reviews of Belcher and Hunt (1998) and Charru, Andreotti, and Claudin (2013) report the vast amount of literature devoted to the subject.

Provided that the topography modulation is shallow enough, the response of the flow field is linear. A suitable criterion for this to occur is that the dimensionless perturbation of the shear stress $\tau = \rho u_\tau^2$, defined as $\delta\tau = \tau/\tau_{flat} - 1$, with subscript *flat* denoting its flat-wall value, should respect the condition $|\delta\tau| \ll 1$. In its definition, u_τ is the friction velocity and ρ is the fluid density.

When the linearity condition is met, the problem can be addressed in Fourier space, where the Fourier-transformed dimensionless $\delta\tau$, denoted as $\widehat{\delta\tau}$, is proportional to the Fourier-transformed slope of the wall $\widehat{dh_w/dx}$, through a complex transfer function \mathcal{T} (Luchini and Charru, 2019). In the above definition, $h_w(x)$ is the wall-perturbation height and x is the streamwise coordinate. If wall units are adopted, the transfer function $\mathcal{T}^+(\mathbf{k}^+)$ is defined as

$$\mathcal{T}^+(\mathbf{k}^+) = \frac{\widehat{\delta\tau^+}}{\widehat{dh_w^+/dx^+}} = \frac{\widehat{\delta\tau^+}}{-i\mathbf{k}^+\widehat{h_w^+}}, \quad (6.1)$$

where $\mathbf{k}^+ = \mathbf{k}\nu/u_\tau$ is the dimensionless wavenumber, with ν the kinematic viscosity of the fluid.

The aim of this chapter is to assess the accuracy of some analytical expressions of the transfer function $\mathcal{T}(\mathbf{k})$ proposed by Luchini and Charru (2017) and Luchini and Charru (2019), by comparing them with direct numerical simulations of the flow over a smooth bump. In particular, Luchini and Charru (2019) proposed the following analytical asymptotic approximation:

$$\mathcal{T}(\mathbf{k}^+)^+ = \left[\frac{c_1}{c_2} (-i\mathbf{k}^+)^{2/3} - i \frac{c_0}{c_2} (U_{\text{ext}}^+)^{-2} (-i\mathbf{k}^+)^{-2/3} \text{sign}(\mathbf{k}) \right]^{-1}, \quad (6.2)$$

where $c_1/c_2 = 0.93889$, $c_0/c_2 = 0.72901$ and U_{ext} denotes the external velocity in laminar flow whereas in turbulent flow U_{ext}^+ is replaced by $U_{\text{mean}}^+((\mathbf{k}^+)^{-1})$, $U_{\text{mean}}(z)$ being the unperturbed turbulent mean velocity profile. Since the wall perturbation must be shallow for the response to be

linear, the latter velocity profile can be identified with the universal law of the wall, for which the interpolation provided by Luchini (2018) will be adopted:

$$U_{\text{mean}}^+(z^+) = \frac{\log(z^+ + 3.109)}{0.392} + 4.48 - \frac{7.3736 + (0.4930 - 0.02450z^+)z^+}{1 + (0.05736 + 0.01101z^+)z^+} e^{-0.03385z^+}. \quad (6.3)$$

In laminar regime, the expression (6.2) applies to an open flow, one where the distance to any bounding walls is large compared to the wavelength, and peaks at $k^+ \simeq (U_{\text{ext}}^+)^{-3/2}$, a point where the boundary-layer thickness (which is proportional to U_{ext} in these dimensionless units) is smaller than the wavelength. For $k^+ \lesssim (U_{\text{ext}}^+)^{-3/2}$ the response of open and confined flows differs, since the latter keeps increasing with decreasing k . For $k^+ \gtrsim (U_{\text{ext}}^+)^{-3/2}$ confined flow behaves similarly, in such a way that both cases tends to the $k^{-2/3}$ behavior already observed by Benjamin (1959).

A separate approximation of the transfer function was provided by Luchini and Charru (2017) on somewhat different assumptions. There the authors studied the quasilaminar approximation, suitable in a range of $k^+ \gtrsim 10^{-3}$, which assumes that perturbations occur close enough to the wall for them to be determined by the turbulent mean velocity profile in combination with laminar viscosity only. By comparing and combining the quasilaminar result with DNS and experiments taken from previous literature, they proposed the Padé interpolation

$$\begin{aligned} -ik^+ \mathcal{T}^+(k^+) - 2k^+ = \\ k^+ - 0.002087 - 0.000928i \\ \frac{0.05220 + 0.03837i + (1.6592 + 1.2380i)k^+ + (-0.7009 + 1.2051i)(k^+)^2}{0.05220 + 0.03837i + (1.6592 + 1.2380i)k^+ + (-0.7009 + 1.2051i)(k^+)^2}. \end{aligned} \quad (6.4)$$

6.2 Friction prediction in laminar flows

The asymptotic transfer function reported in eq.(6.2) is first evaluated in the laminar regime. In order to perform an accurate analysis of the friction prediction, the lower wall of a channel is perturbed by using the bump G_1 , already introduced in chapter 3. Laminar simulations are performed inside a channel at $Re_\tau = 200$, by employing the same code of chapter 3. G_1 has maximum height of $h_b = 0.084h$, where h is half the distance between the

plane walls, and corresponds to $h_b^+ = 17$ when expressed in viscous scale by using the friction velocity u_τ computed far from the bump. Unless otherwise noted (e.g. where viscous units are employed), in the following lengths are made dimensionless with h .

As already mentioned, despite equation (6.2) in laminar regime applies to open flows only, it can be used to predict friction perturbation for confined flows in the range of wavenumbers $k^+ \gtrsim (U_{\text{ext}}^+)^{-3/2}$. In order to investigate if the present test case meets this condition, figure 6.1 plots the module of the transformed wall-slope, i.e. $k^+ |\widehat{G_1^+}|$, here vertically shifted in order to compare it with $\mathcal{T}^+(k^+)$. The range of significant wavelengths falls where open and confined flows behaves similarly, with k^+ larger than $(U_{\text{ext}}^+)^{-3/2}$ (whose value is denoted by the vertical dotted line), and both imaginary and real components of equation (6.2) almost coincide with the $k^{-2/3}$ behaviour of Benjamin (1959). For this confined test case, the asymptotic transfer function can therefore be used to predict the wall-shear stress perturbations.

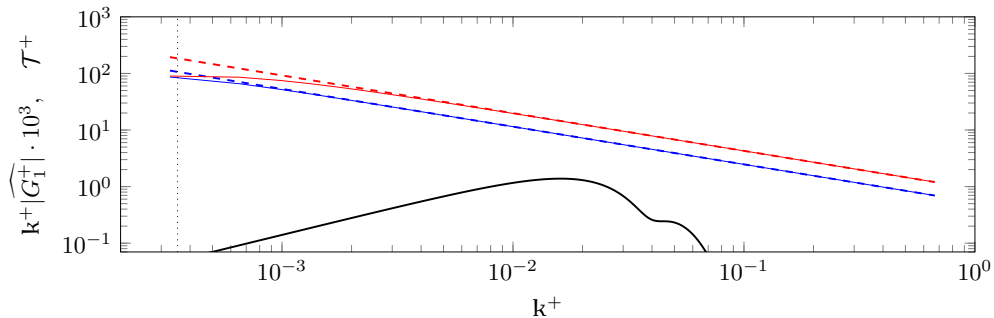


Figure 6.1: Module of the transformed wall-slope $k^+ |\widehat{G_1^+}|$ (black) and comparison between the asymptotic response function (6.2) (solid lines) and classical theory (Benjamin, 1959) (dashed lines): real (blue) and imaginary (red) components.

Five DNS in laminar regime are performed by progressively decreasing the vertical extent of the bump: $(\frac{G_1}{1}, \frac{G_1}{2}, \frac{G_1}{4}, \frac{G_1}{8}, \frac{G_1}{16})$. For simplicity, in the following, any simulations will be labeled only using its denominator, here called a . The employed mesh is the same of chapter 3, with the exception of the spanwise direction where only one cell is required. The inlet condition is the Poiseuille velocity profile.

The wall-shear stress perturbation $\delta\tau$ computed over the five geometries is shown in the upper panel of figure 6.2. The tallest bump, with the scale factor $a = 1$, has a maximum value close to $\delta\tau \approx 7$ and it is the only case where flow separation occurs, identified by $\delta\tau < -1$. The cases with $a = 2$ and $a = 4$ also present a maximum $\delta\tau$ larger than 1. For these three

cases no agreement is expected with the asymptotic prediction, since the maximum $\delta\tau$ exceeds the validity range of the linear assumption, all the more so when separation occurs. In order to assess the linearity of the laminar response, the lower panel of figure 6.2 also plots the quantity $a\delta\tau$. The two cases with $a = 8$ and $a = 16$ are very close to each other, implying that they are approaching the linear regime. For $a = 16$, the maximum of $\delta\tau$ is in fact around 0.2, approaching the hypothesis of $\delta\tau \ll 1$.

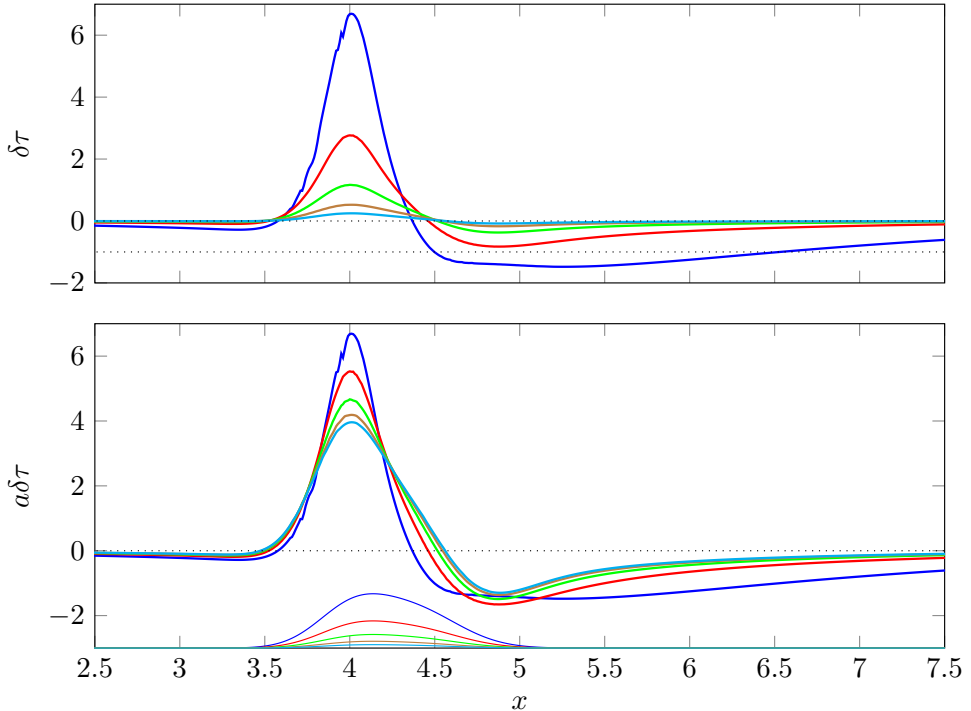


Figure 6.2: Wall-shear stress perturbation $\delta\tau$ for the five bumps $\frac{G_1}{a}$: $a = 1$ (blue), $a = 2$ (red), $a = 4$ (green), $a = 8$ (brown), $a = 16$ (cyan). Top: $\delta\tau$; bottom: $a\delta\tau$. The thin profiles at the bottom of the plot draw the five bump geometries.

The comparison between the computed and analytical $\delta\tau$ is plotted in figure 6.3 for the five geometries. The predicted $\delta\tau$ is always in qualitative agreement with DNS data, with the exception of the separated area of the case $a = 1$, where the two curves show a different behaviour. Quantitative differences, more evident around the extremes of $\delta\tau$, decrease when the linearity range is approached and for $a = 16$ the two curves almost overlap.

The relative error in predicting the maximum (Δ_M) and minimum (Δ_m) of $\delta\tau$ is reported for the five geometries in table 6.1. The error for both maxima and minima monotonically decreases by increasing a to a value around 5% once the linear regime is approached. The only exception is

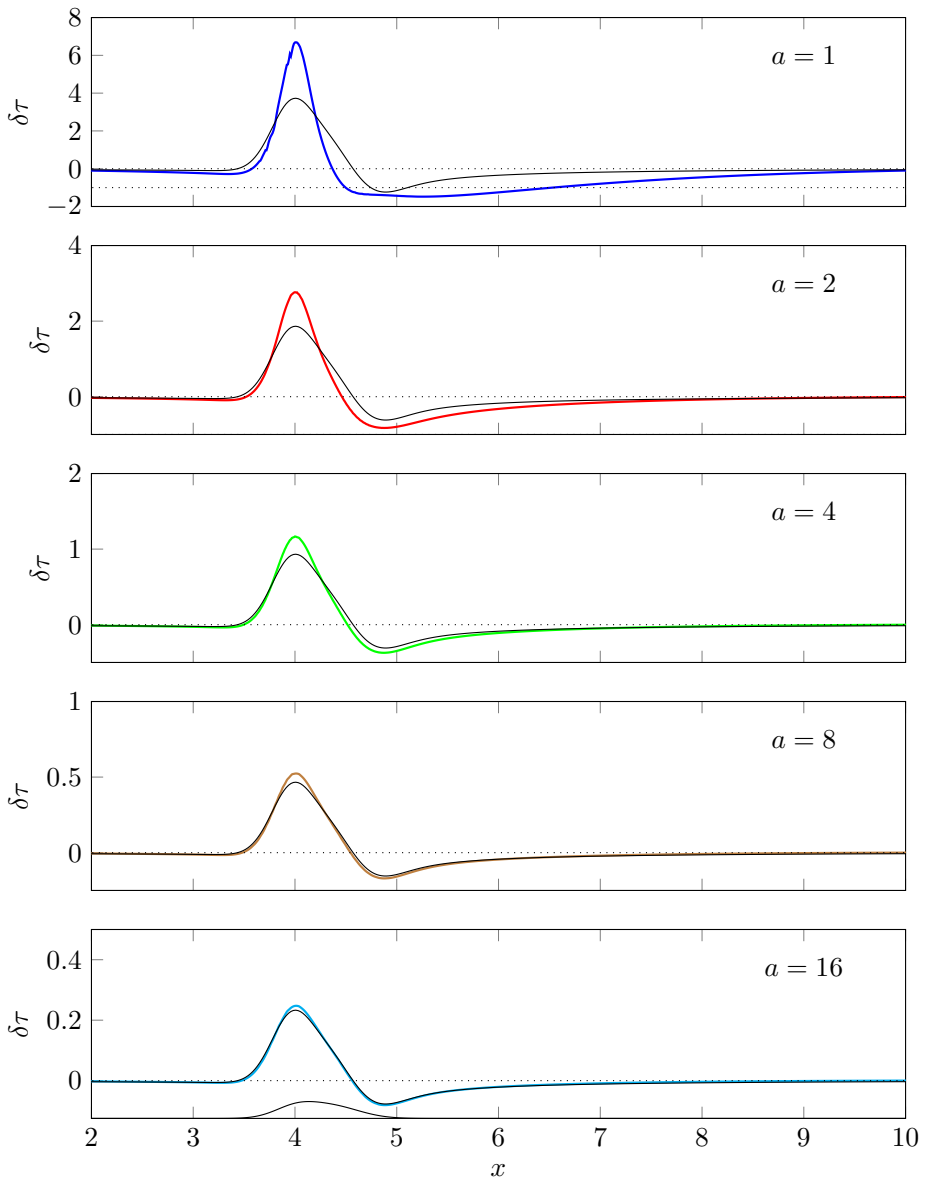


Figure 6.3: Wall-shear stress perturbation $\delta\tau$: computed (thick colour line, colour-coded as in figure 6.1) and predicted (thin black lines) for the five geometries. Note the vertical scale that is multiplied by $1/a$.

related again to the case $a = 1$ where $\Delta_m\%$ is lower than in case $a = 2$. This exception is, however, due to a qualitative difference between the two curves when separation occurs. Both maxima and minima streamwise location are well predicted for all geometries, except the negative value in the separated case $a = 1$. When separation occurs, the asymptotic transfer

a	$\Delta_M\%$	$\Delta_m\%$
1	45.5	16 ($\Delta x_m = 0.37h$)
2	32.6	25.3
4	20.2	17.0
8	11	9.3
16	5.9	4.7

Table 6.1: Relative error for maximum (Δ_M) and minimum (Δ_m) of $\delta\tau$.

function fails to forecast both detachment and reattachment streamwise locations.

The asymptotic transfer function correctly predicts the wall-shear stress perturbations when the linear regime is approached. It is worth noticing that this analysis does not test the range of wavelength where equation (6.2) differs from classical theory. Boundary layer simulations to amplify the investigated range are underway.

6.3 Friction prediction in turbulent flows

The analysis is here extended to the turbulent regime. Analytical $\delta\tau$ is compared with data obtained via turbulent DNS over G_1 , already discussed in chapter 3 and over two additional geometries. The first, namely G_{1h} , is the case with halved vertical extent, i.e. with scale factor $a = 2$, whereas G_{1L} is derived from the original geometry by a streamwise expansion factor of 2. These new geometries hence possess the same wall slope. Turbulent DNS over G_{1h} and G_{1L} are carried out with the same setup reported in chapter 3. The three bumps are shown in figure 6.4. As observed in the context of chapter 3, the geometry G_1 significantly modifies the friction distribution and largely exceeds the linear regime. No agreement is therefore expected between analytical and computed friction perturbation.

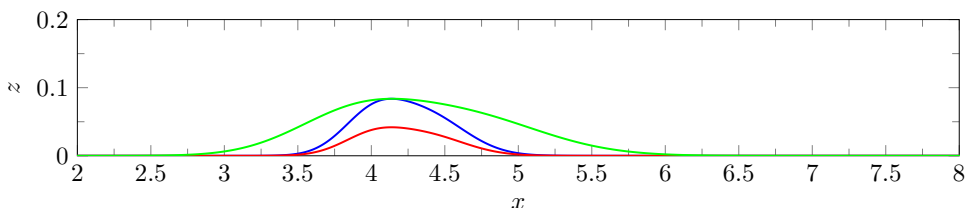


Figure 6.4: Bump geometries G_1 (blue), G_{1h} (red) and G_{1L} (green).

In turbulent regime, the asymptotic transfer function (6.2), introduced by

Luchini and Charru (2019), and already tested for laminar flows in the previous paragraph, can be compared with the empirical transfer function (6.4) presented in Luchini and Charru (2017).

Figure 6.5 plots the comparison between computed and analytical wall-shear stress perturbation over the three bump geometries separately. $\delta\tau$

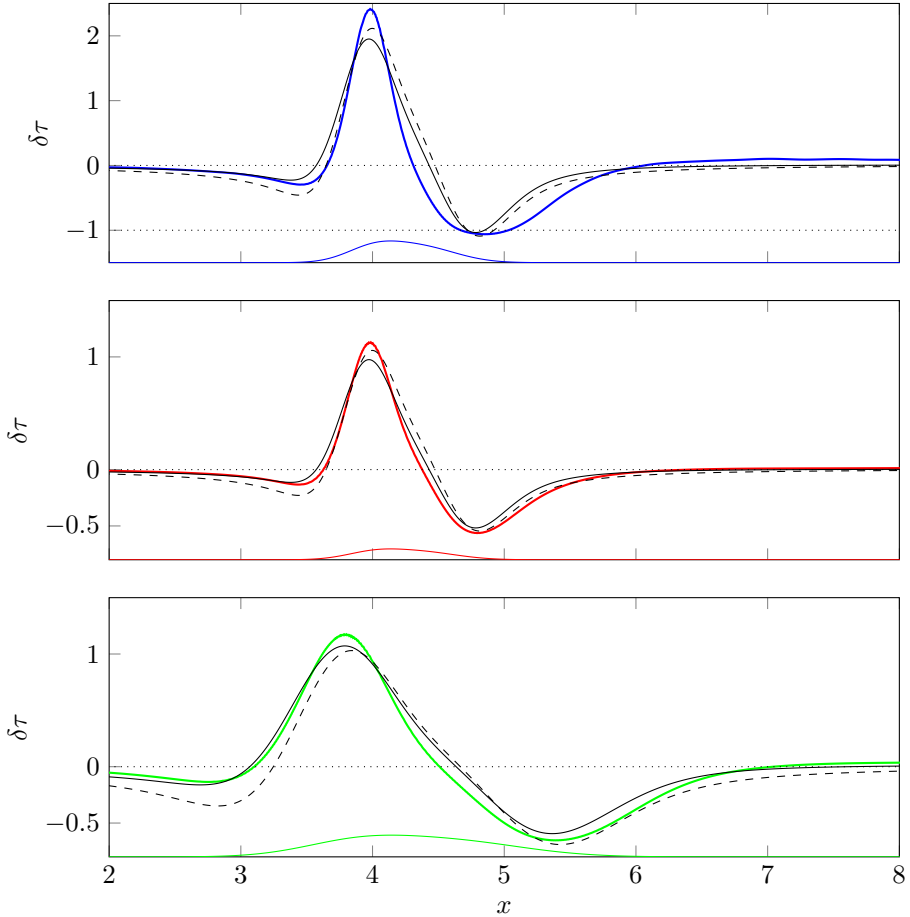


Figure 6.5: Wall-shear stress perturbation $\delta\tau$: computed (thick colour lines, colour-coded as in figure 6.4) and predicted via asymptotic (thin solid lines, black) and empirical (thin dashed lines, black) transfer functions. Top: G_1 ; centre: G_{1h} ; bottom: G_{1L} .

over G_1 reaches a maximum value higher than 2, and a mild separation occurs in the aft part, leading to $\delta\tau$ below -1 . Nevertheless, the first panel of figure 6.5 shows a good agreement between computed and analytical friction perturbation; both transfer functions correctly reproduce the qualitative behaviour, with the only exception of the aft side of G_1 , where separation takes place and friction slope is not well captured.

Quantitative differences are obviously present; errors at the extremes are reported in table 6.2. Since in turbulent flows a quite pronounced local minimum is present immediately upstream the bump, error in predicting the friction perturbation amplitude is computed for this point too, and reported in table 6.2 with subscript lm .

	$\Delta_{lm}\%$	$\Delta_M\%$	$\Delta_m\%$
G_1	23.5 (54.5)	19.0 (12.2)	2.5 (2.7)
G_{1h}	14.8 (72.2)	13.6 (6.3)	8.1 (3.2)
G_{1L}	19.4 (158)	8.7 (12.2)	9.1 (5.6)

Table 6.2: Relative error of the analytical (6.2) and empirical (6.4) prediction, for the local minimum (Δ_{lm}), the maximum (Δ_M) and minimum (Δ_m) of $\delta\tau$. Error via empirical transfer function (6.4) is reported in parentheses.

Differences between the analytical prediction and computed friction perturbation are satisfying since, for the steeper bump G_1 , the maximum error is around 20%. Moreover, even the streamwise location of the minimum inside the separation bubble is well reproduced, dissimilarly from the laminar case; this disagreement, however, could be explained with the reduced intensity and dimension of the recirculation. The empirical transfer function improves the accuracy in reproducing both maximum and minimum of $\delta\tau$, while it strongly overestimates the first local minimum.

Over geometries G_{1h} and G_{1L} , wall slope is halved compared to G_1 . The maximum and minimum of $\delta\tau$ are almost halved too (note the halved vertical scale of the plot) and a better agreement is expected. When the analytical transfer function is employed, table 6.2 reports a substantial error reduction in reproducing maximum of $\delta\tau$ and a slight error reduction for the first local minimum. As already observed in laminar flows, the error related to the negative minimum increases moving from G_1 to G_{1h} . This unexpected trend is, however, only related to the minimum value, and it is not confirmed if the analysis is expanded to the entire aft side of the bump. In the separated case G_1 , the slope of $\delta\tau$ is poorly reproduced, and the distance between computed and analytical curves increases. The only exception is the minimum value itself, whose intensity is quite well predicted, strengthening the idea that the presence of separation can be correctly forecast by the two tested transfer functions.

6.4 Comparison with literature data

The previous paragraph shows that a decent wall-shear stress prediction is obtained in turbulent flows by using both the transfer functions (6.2) and

(6.4) even when $\delta\tau$ is larger than 1. It is interesting to extend the analysis to steeper and larger obstacles by comparing analytical results to previous literature studies. In Mollicone et al. (2018), three different arc-shaped bumps, analytically defined by the equation $y = -a(x - 4)^2 - 0.5$, are studied via DNS inside a turbulent channel flow. Figure 6.6 portrays the three geometries; the maximum height is $h_b = 0.5h$, that corresponds to $h_b^+ = 80$ at the lowest Reynolds number employed $Re_\tau = 160$. Moreover,

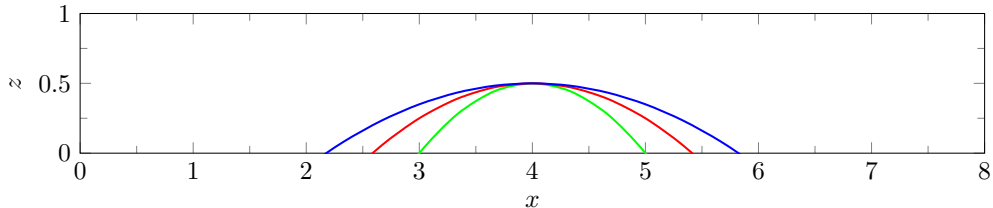


Figure 6.6: Different bump geometries analysed by Mollicone et al. (2018), given by $y = -a(x - 4)^2 - 0.5$. $a = 0.15$ (blue), $a = 0.25$ (red) and $a = 0.5$ (green).

the less steep geometry, with $a = 0.15$, is investigated even at friction Reynolds number $Re_\tau = 280$ and $Re_\tau = 550$. A wide separation bubble is observed over each geometry, and the maximum of $\delta\tau$ obtained is around 6. No agreement is therefore expected with analytical wall-shear stress perturbation.

Figure 6.7 plots the streamwise distribution of $\delta\tau$ for the five cases individually. Numerical and analytical results do differ, of course, when the large separation bubble is present, but the agreement is still quite good even when the first recirculation occurs before the bump, and a reasonable maximum value is reproduced even if $\delta\tau$ strongly exceeds the linearity range. Moreover, the predicted streamwise location of the maximum of $\delta\tau$ is moved upstream over each geometry. Increasing the Reynolds number leads to loss of agreement when the empirical transfer function is employed, while the asymptotic theory seems to guarantee a discrete agreement in terms of maximum amplitude. The streamwise distance between computed and analytical maximum of $\delta\tau$, negligible over the small bumps analysed in the previous paragraph, significantly increases with the Reynolds number. In this context, however, several differences arise: the departure from the linearity range is now stronger, and the more prominent separation bubble could affect the entire flow field.

In order to further investigate the influence of a wide separation bubble, the Large Eddy Simulations of a boundary layer over an arc-shaped bump performed by Wu and Squires (1998) is now considered. A more recent work by Matai and Durbin (2019) considers the same geometry again, with

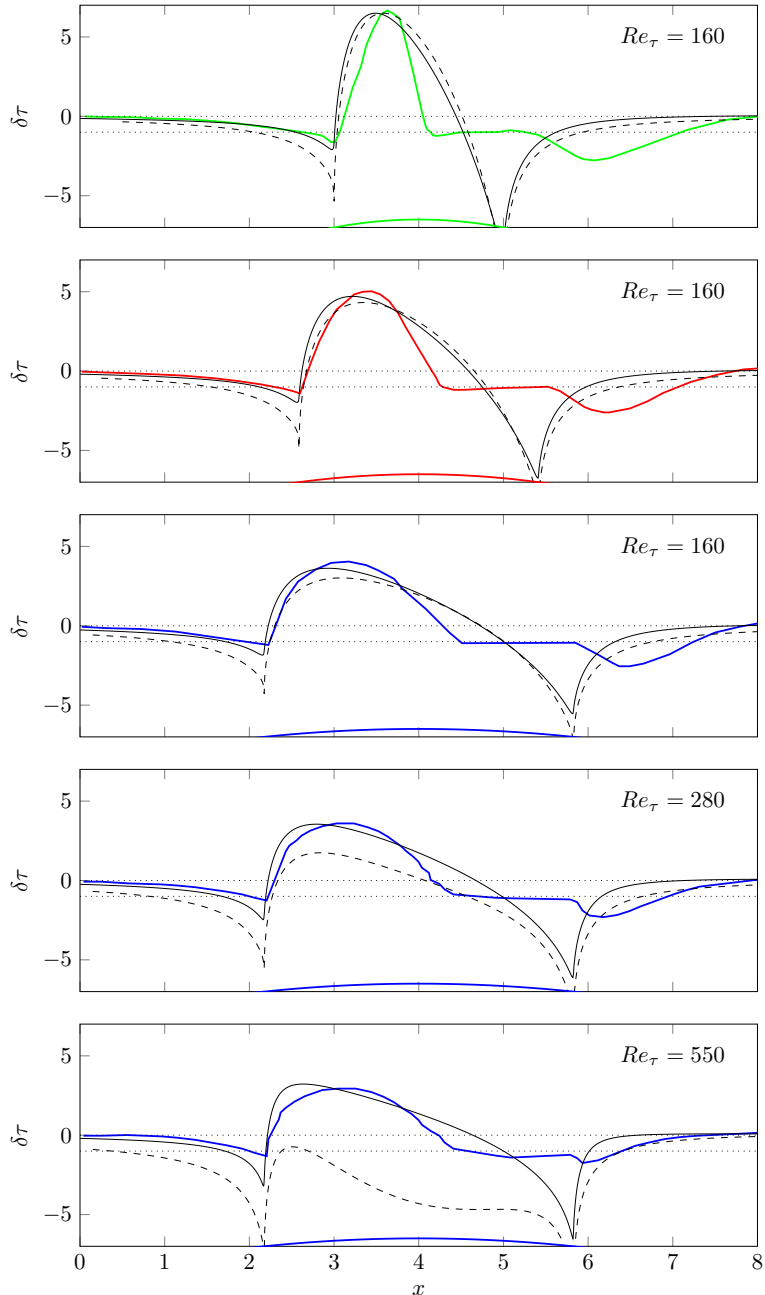


Figure 6.7: Wall-shear stress perturbation $\delta\tau$: computed (thick colour lines, colour-coded as in figure 6.6), and predicted via the asymptotic (thin solid lines, black) and empirical (thin dashed lines, black) transfer functions. First panel: $a = 0.5$; second panel: $a = 0.25$; third, fourth and fifth panels: $a = 0.15$ at $Re_\tau = 160 - 280 - 550$, respectively. DNS data taken from Mollicone et al. (2018)

a slightly increased Reynolds number, and then performs a parametric study by increasing the bump height. By considering the smallest and the highest geometries within the parametric study, the influence of a large separation bubble can be properly investigated, since separation occurs only over the highest bump.

Figure 6.8 plots the two geometries. In boundary layer simulations, the half channel height h is not defined since there is no upper wall, and lengths are made dimensionless with the bump length ℓ_b , as explicitly specified in the following figures. Unlike Mollicone et al. (2018), two smaller arcs are

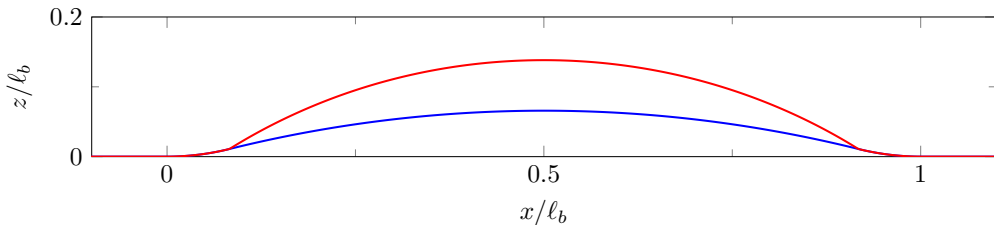


Figure 6.8: Different bump geometries analysed by Wu and Squires (1998) and Matai and Durbin (2019): $h_b/\ell_b = 0.066$ (blue), $h_b/\ell_b = 0.137$ (red).

used to connect the flat wall with the arc-shaped geometry in such a way that the smallest bump does not present derivative discontinuities. The smallest geometry, with $h_b/\ell_b = 0.066$, is here investigated at two different Reynolds numbers, thus leading to different dimensions, when expressed in viscous units. In Wu and Squires (1998), its streamwise and wall-normal extents are $\ell_b^+ = 6200$ and height of $h_b^+ = 400$, while in Matai and Durbin (2019) they become $\ell_b^+ = 8500$ and $h_b^+ = 560$. The tallest bump with $h_b/\ell_b = 0.137$, on the other hand, has been investigated by Matai and Durbin (2019) only, and in viscous units it has dimensions $\ell_b^+ = 8500$ and $h_b^+ = 1165$.

In figure 6.9, the wall-shear stress perturbation taken from literature data, is compared with the predicted $\delta\tau$ computed by using the analytical transfer function only, since the empirical one did not match at all. The agreement is good, and the qualitative behaviour is well reproduced. Differently from previous comparison with DNS, the maximum amplitude is over-estimated. Moreover, over the smallest bump, that does not lead to flow separation, the streamwise position of the maximum value, that is quite close to the bump beginning, is well captured by the prediction strategy. When the highest bump, which induces a wide separation bubble, is analysed, however, the forecast maximum of $\delta\tau$ is strongly anticipated as already observed in the context of figure 6.7. Figure 6.9 reinforces the idea that the discrepancy in the streamwise location of the maximum of

$\delta\tau$ is induced by the presence of the large separation bubble. Moreover, when the smallest bump is considered, differently from previous comparisons, there is no agreement between LES and the prediction strategy in assessing whether or not separation occurs.

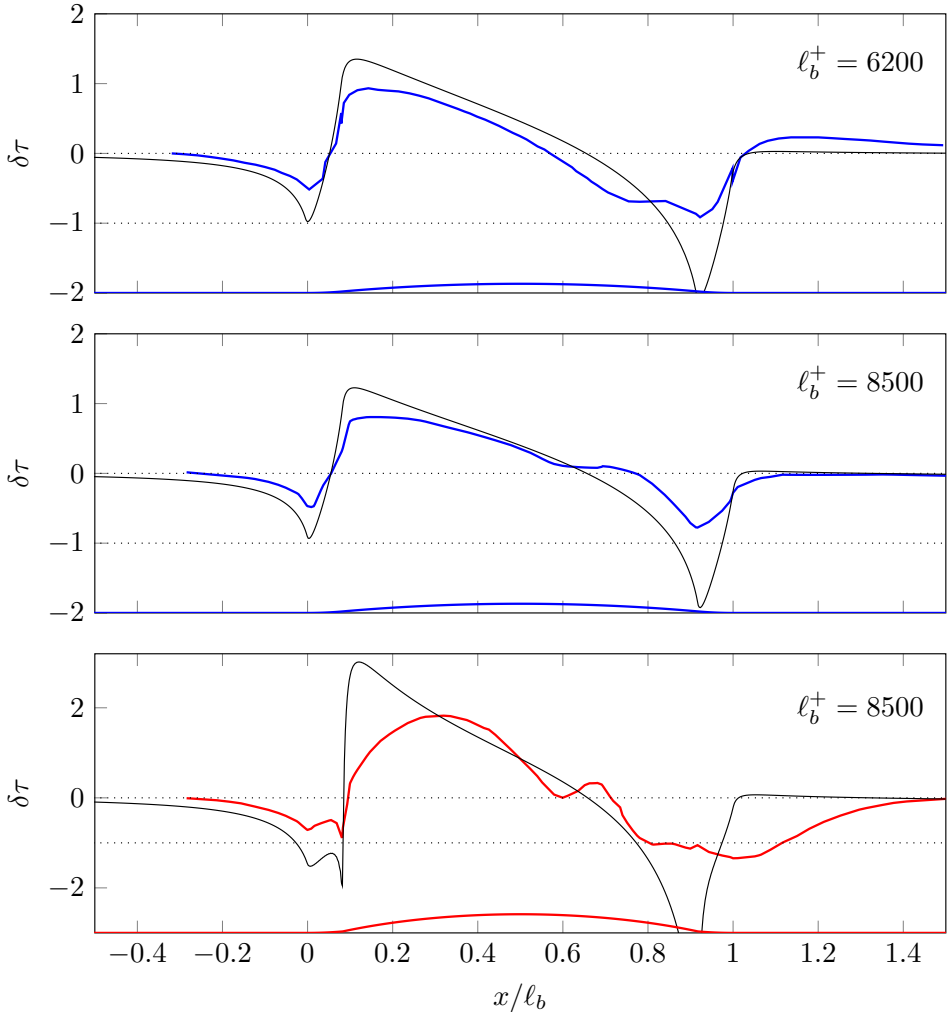


Figure 6.9: Wall-shear stress perturbation $\delta\tau$: computed (thick colour lines, colour-coded as in figure 6.8), and predicted via asymptotic transfer function 6.2 (black lines). First panel: $h_b/\ell_b = 0.066$ with $\ell_b^+ = 6200$; second panel: $h_b/\ell_b = 0.066$ with $\ell_b^+ = 8500$; third panel: $h_b/\ell_b = 0.137$ with $\ell_b^+ = 8500$. DNS data taken from Wu and Squires (1998) and Matai and Durbin (2019).

6.5 Conclusions

The theory for the prediction of wall-shear stress over smooth non-planar walls proposed by Luchini and Charru (2019) has been numerically investigated, with DNS simulations as well as with reference to existing datasets. The transfer function has been first tested in the laminar regime, where five localized bumps of different height have been considered. It has been shown that, when the linear regime is approached, i.e. with $|\delta\tau^+| \ll 1$, the agreement between the computed and predicted friction deviations is remarkable.

The prediction strategy has been then studied in the turbulent regime, where the turbulent channel flow with one wall with a bump of three sizes has been studied via DNS. The prediction theory has been also compared with another transfer function obtained by interpolating several DNS results and previously reported in Luchini and Charru (2017). Both strategies show a good agreement despite the departure from linearity range and the presence of the small separation bubble.

Finally, available literature results have been used to generalize the comparison. The DNS channel flow simulations by Mollicone et al. (2018), and the LES boundary layers reported in Wu and Squires (1998) and Matai and Durbin (2019) have been used. These two comparisons assessed that in presence of larger bumps, the empirical transfer function by Luchini and Charru (2017) fails to reproduce the friction perturbation distribution, while the most recent theory unexpectedly reproduce a similar behaviour even when $\delta\tau$ is over 6. Moreover, significant differences arise when a large separation takes place: the streamwise position of the maximum of $\delta\tau$ is predicted quite upstream. As long as the flow remains attached, the validity of friction prediction seems to persist even when the flat wall is perturbed by higher and longer bumps.

CHAPTER 7

CONCLUSIONS

Don't confuse movement
with progress.

DENZEL WASHINGTON

THE work described throughout this Thesis has tackled one of the several open questions that nowadays still surround the whole discipline of flow control: How does a (percentage) friction reduction measured in a lab experiment or low-*Re* numerical simulations over a flat wall translate into a potential saving of energy (fuel) for a commercial aircraft? In other words: what would be the true impact of a friction drag reduction technique when applied over the external surface of a commercial aircraft?

The trivial answer is quite widespread in the flow control community, and I have heard it several times during my PhD years. The flow control strategy is usually supposed to act on the friction component alone of the total drag, without interfering with pressure drag, as in experiments over plane walls. Our preliminary investigation has used RANS-based simulations to assess whether or not such trivial answer is reliable. Of course

the technique of choice, namely StTW, had to be modeled indirectly, via a modified wall boundary condition in a wall-functions formulation. The StTW has thus been applied over the whole external surface of a commercial aircraft in transonic flight. The analysis on lift and drag has led to positive conclusions, both for our self-esteem (the answer is indeed not trivial) and the flow control community (StTW reduce friction and interact with the pressure field too). Most importantly, StTW change the shock-wave position, consequently increasing lift. The energy budget of the aircraft does not confirm the trivial first guess, and shows total savings which are 50% higher than expected.

Such a RANS-based study, however, is obviously relying on several questionable assumptions, and we refrained to deduce out of it more than a motivation to begin a thorough research from the ground up. The first step was a low- Re Direct Numerical Simulations of an incompressible turbulent channel flow with a curved wall, in order to establish first how friction drag reduction affects the total drag in presence of form drag. The work has led us to demonstrate that the actual power saving can be larger than the simple extrapolation discussed above thanks to two different effects. In fact, the amount of friction reduction over the curved wall is higher than the flat wall percentage; moreover, pressure drag is significantly reduced. These results are just a first step along the path leading to the actual aircraft, yet they confirm, reliably this time, that the problem we are addressing is not trivial, although the setup still resembles very much that of a channel flow.

To overcome that limitation and move a step closer to the ultimate application, Direct Numerical Simulations of the transonic flow field around an airfoil have been carried out. In this case, StTW were only applied over a limited portion of the suction side of the airfoil. The idea is to look at the problem from a different perspective, by changing the physics and allowing compressibility and the presence of a shock-wave to come into play. The StTW was observed to clearly reduce friction; more importantly, it influenced the interaction between shock-wave and boundary layer, such that the shock-wave is deferred downstream and lift is significantly increased. The airfoil efficiency, i.e. the ratio between lift and drag, is increased by 12%, although StTW is applied over one-quarter of the airfoil surface only. These results fully confirm the outcome of our RANS-based exploratory work, and confirm a potentially far-reaching concept: skin-friction reduction techniques can be applied locally, to produce a global gain. In other words, drag reduction can be thought of as a sort of localized actuator, similarly to a vortex generator or a winglet. Typically such actuators imply a direct drag penalty which can be overcome by a larger performance

benefit. In this case, the drag penalty itself is negative (i.e. drag decrease). The perspective change from distributed to localized skin-friction drag reduction has the potential to change the cost-benefit analysis significantly. Traditionally, to achieve friction reduction one would need to cover the whole surface area with the drag-reduction technology (e.g. riblets). But a large fraction of the drag benefit could be obtained with a radical reduction of covered surface, provided riblets are suitable placed on the wing.

The investigation on flow control is then extended to a relatively new concept for friction reduction, based on non-uniform and unsteady blowing (oscillating jets through narrow streamwise slits). We have joined an ongoing experimental campaign and attempted to complement it with DNS. The actuator has been successfully reproduced, and the friction reduction obtained in the numerical simulations matches very well the experimental data. The rich dataset that comes naturally with a DNS has allowed us to ascertain, however, that both unsteadiness and spatial non-uniformity of the blowing provide but marginal contributions to the drag reduction effectiveness, and that the proposed actuation strategy is essentially equivalent to a simple uniform blowing

In our work, we have also considered the problem of wall friction prediction. When the wall smoothly varies, the flow field response becomes linear and, when studied in Fourier-space, the friction perturbation is proportional to the wall slope via a complex transfer function. We have used our DNS capabilities to carry out incompressible DNS over curved walls and assess the accuracy of the transfer functions recently proposed by Luchini and Charru (2017) and Luchini and Charru (2019). The analytical prediction of the friction distribution is observed to satisfactorily agree with numerical data, in both laminar and turbulent regime. Surprisingly, even when the bump-induced perturbations exceed the linearity range a discrete friction prediction is still present, observed

7.1 Roadmap of future research and development

The results presented in this Thesis only represent a few steps, and way more distance need to be covered to see friction reduction techniques applied in real life and on real airplanes. The new results presented in this Thesis lead to new questions and suggestions for interesting next steps. The possible follow-ups are listed below on a chapter-by-chapter basis:

- RANS-based simulations presented in chapter 2 have captured the interaction between active flow control and the shock-wave position,

as subsequently confirmed by the transonic DNS. The qualitative agreement observed in the shock-wave displacement, however, should be quantitatively investigated by studying the same, or similar, case of study. In this context RANS simulations represent a powerful tool, owing to their ability to address complex geometries at high-Reynolds-numbers. Developments would require a rigorous validation of their reliability, as well as improvements in the way a possibly unsteady, small-scale flow control technique is modeled within the RANS approach.

- The effect of applying StTW over the shallow bump described in chapter 3 should be generalized by investigating different geometries and different friction reduction techniques. An optimization could identify the bump of a given height that yields the largest drag reduction. Moreover, since taller bumps increase the blockage effect, boundary layer simulations should be employed to generalize the impact of friction reduction techniques over curved walls.

Moving on to compressible flows, the boundary layer over a curved wall in transonic regime could represent a suitable setup to investigate the interaction between friction drag reduction and shock-wave thoroughly.

- The flow phenomena observed around the transonic airfoil in chapter 4 need more attention for several reasons, already pointed out in the text. The value of the Reynolds number, obviously limited by the computational cost, should be increased until a fully turbulent boundary layer is obtained before the actuator. To trust these results fully, it should be demonstrated that the shock-wave displacement is independent of both the employed tripping strategy and the presence of flow separation. In addition, it is interesting to reproduce the same case, with and without StTW, in the subsonic regime, so that the influence of the deferred shock-wave could be singled out. Finally, the interaction between StTW and shock-waves hints that spanwise forcing can be used locally to produce a global gain. Hence, it is interesting (but computationally expensive) to expand the analysis to a three-dimensional wing geometry in transonic regime.
- The study of blowing actuators presented in chapter 4, can be enhanced following several strategies. The streamwise length of the control region can be increased in order to verify the optimal extension to avoid the undesired increase of friction downstream the actuator. Moreover, the spanwise non-uniform configuration here investigated can be suitably employed to reduce friction by using the

opposition-control strategy.

Finally, since results presented in chapter 4 assessed that friction reduction strategies could be applied locally, to produce a global gain, it should be interesting to investigate how the shock-wave over a transonic airfoil interacts with blowing/suction actuators.

- The laminar investigation of the asymptotic transfer function presented in chapter 6 should be generalized for a larger range of wavenumbers. In order to test the accuracy of the employed strategy at lower wavenumbers, boundary layer simulations must be employed.

BIBLIOGRAPHY

- Abbassi, M.R., W.J. Baars, N. Hutchins, and I. Marusic (2017). “Skin-friction drag reduction in a high-Reynolds-number turbulent boundary layer via real-time control of large-scale structures”. In: *Int. J. Heat and Fluid Flow* 67, pp. 30–41 (cit. on p. 84).
- Airbus (2020). *A320neo*. <https://www.airbus.com/aircraft/passenger-aircraft/a320-family/a320neo.html> [Online: Accessed 24-September-2020] (cit. on p. 32).
- Almeida, G.P., D.F.G. Durao, and M.V. Heitor (1993). “Wake flows behind two-dimensional model hills.” In: *Exp Thermal Fluid Sci* 7, pp. 87–101 (cit. on p. 37).
- Atzori, M., R. Vinuesa, A. Stroh, B. Frohnappel, and P. Schlatter (2018). “Assessment of skin-friction-reduction techniques on a turbulent wing section”. In: *12Th ERCOF-TAC Symp. on Engineering Turbulence Modeling and Measurements (ETMM12)* (cit. on pp. 36, 64).
- Aupoix, B., G. Pailhas, and R. Houdeville (2012). “Towards a General Strategy to Model Riblet Effects”. In: *AIAA J.* 50, pp. 708–716 (cit. on p. 11).
- Auteri, F., A. Baron, M. Belan, G. Campanardi, and M. Quadrio (2010). “Experimental assessment of drag reduction by traveling waves in a turbulent pipe flow”. In: *Phys. Fluids* 22.11, pp. 115103/14 (cit. on pp. 7, 41).
- Babinsky, H. and J.K. Harvey (2011). *Shock wave-boundary-layer interactions*. Vol. 32. Cambridge University Press (cit. on pp. 64, 65).
- Bai, H.L., Y. Zhou, W.G. Zhang, S.J. Xu, Y. Wang, and R.A. Antonia (2014). “Active control of a turbulent boundary layer based on local surface perturbation”. In: *J. of Fluid Mech.* 750, pp. 316–354 (cit. on pp. 12, 13, 82, 83, 92).
- Banchetti, J., P. Luchini, and M. Quadrio (2020). “Turbulent drag reduction over curved walls”. In: *J. Fluid Mech.* 896 (cit. on p. 36).
- Banchetti, J. and M. Quadrio (2019). “Turbulent drag reduction for a wall with a bump”. In: *European Turbulence Conference, Turin, September 3–6 2019* (cit. on p. 36).
- Bandyopadhyay, P. R. (1986). “Review - Mean Flow in Turbulent Boundary Layers Disturbed to Alter Skin Friction”. In: *J. Fluids Eng.* 108.2, pp. 127–140 (cit. on p. 10).
- Belcher, S.E. and J. C.R. Hunt (1998). “Turbulent flow over hills and waves”. In: *Annual Rev. Fluid Mech.* 30, pp. 507–538 (cit. on pp. 103, 104).

Bibliography

- Benjamin, T.B. (1959). "Shearing flow over a wavy boundary". In: *J. Fluid Mech.* 6, pp. 161–205 (cit. on pp. 13, 103, 105, 106).
- Berger, T. W., J. Kim, C. Lee, and J. Lim (2000). "Turbulent boundary layer control utilizing the Lorentz force". In: *Phys. Fluids* 12.3, pp. 631–649 (cit. on p. 3).
- Bernard, A., J. M. Foucaut, P. Dupont, and M. Stanislas (2003). "Decelerating boundary layer: a new scaling and mixing model." In: *AIAA J.* 41.2, pp. 248–255 (cit. on p. 37).
- Breuer, M., N. Peller, Ch. Rapp, and M. Manhart (2009). "Flow over periodic hills: a numerical and experimental study in a wide range of Reynolds number". In: *Computers & Fluids* 38.2, pp. 433–457 (cit. on p. 37).
- Charru, F., B. Andreotti, and P. Claudin (2013). "Sand Ripples and Dunes". In: *Annual Rev. Fluid Mech.* 45.1, pp. 469–493 (cit. on pp. 13, 104).
- Choi, H., P. Moin, and J. Kim (1994). "Active turbulence control for drag reduction in wall-bounded flows". In: *J. Fluid Mech.* 262, pp. 75–110 (cit. on pp. 3, 12).
- Choi, J.-I., C.-X. Xu, and H. J. Sung (2002). "Drag reduction by spanwise wall oscillation in wall-bounded turbulent flows". In: *AIAA J.* 40.5, pp. 842–850 (cit. on pp. 5, 6).
- Choi, K.-S. (1989). "Near-wall structure of a turbulent boundary layer with riblets". In: *J. Fluid Mech.* 208, pp. 417–458 (cit. on pp. 10, 20).
- Choi, K.-S., T. Jukes, and R. Whalley (2011). "Turbulent boundary-layer control with plasma actuators". In: *Phil. Trans. R. Soc. A* 369.1940, pp. 1443–1458 (cit. on p. 7).
- Delery, J.M. (1983). "Experimental investigation of turbulence properties in transonic shock/boundary-layer interactions". In: *AIAA J.* 21.2, pp. 180–185 (cit. on p. 64).
- Ducros, F., V Ferrand, F. Nicoud, C. Weber, D. Darracq, C. Gachereau, and T. Poinsot (1999). "Large-eddy simulation of the shock/turbulence interaction". In: *J. Comp. Phys.* 152.2, pp. 517–549 (cit. on p. 65).
- Duggleby, A., K.S. Ball, and M.R. Paul (2007). "The effect of spanwise wall oscillation on turbulent pipe flow structures resulting in drag reduction". In: *Phys. Fluids* 19.125107, p. 12 (cit. on p. 6).
- Duque-Daza, C.A., M.F. Baig, D.A. Lockerby, S.I. Chernyshenko, and C. Davies (2012). "Modelling turbulent skin-friction control using linearised Navier-Stokes equations". In: *J. Fluid Mech.* 702, pp. 403–414 (cit. on p. 9).
- Endo, T., N. Kasagi, and Y. Suzuki (2000). "Feedback control of wall turbulence with wall deformation". In: *Int. J. Heat Fluid Flow* 21, pp. 568–575 (cit. on p. 4).
- European Environment Agency (2019). *Greenhouse gas emissions from transport in Europe*. <https://www.eea.europa.eu/data-and-maps/indicators/transport-emissions-of-greenhouse-gases/transport-emissions-of-greenhouse-gases-12> [Online: Accessed 27-July-2020] (cit. on p. 1).
- Fournier, G., J.-P. Laval, C. Braud, and M. Stanislas (2010). "Numerical simulations of the flow in a converging-diverging channel with control through a spanwise slot". In: *Int. J. Flow Control* 2.4, pp. 289–310 (cit. on p. 38).
- Gad-el-Hak, M. (1994). "Interactive control of turbulent boundary layers - A futuristic overview". In: *AIAA J.* 32.9, pp. 1753–1765 (cit. on p. 2).
- (2001). "Flow Control: the Future". In: *J. Aircraft* 38.3, pp. 402–418 (cit. on pp. 2, 3).
- Gadda, A. (2016). "A unified GPU-CPU aeroelastic compressible URANS solver for aeronautical, turbomachinery and open rotors applications". PhD thesis. Politecnico di Milano (cit. on p. 24).
- Gadda, A., L. Mangani, G. Romanelli, P. Mantegazza, and E. Casartelli (2016). "A GPU-accelerated compressible RANS solver for Fluid-Structure Interaction simula-

-
- tions in turbomachinery". In: *Int. Symposium on Transport Phenomena and Dynamics of Rotating Machinery* (cit. on p. 22).
- Gadda, A., J. Banchetti, G. Romanelli, and M. Quadrio (2017). "Drag reduction of a whole-aircraft configuration via spanwise forcing". In: *16th EDRFCM, Monteporzicatone* (cit. on pp. 20, 64).
- García-Mayoral, R. and J. Jiménez (2011). "Drag reduction by riblets". In: *Phil. Trans. R.Soc. A* 369.1940, pp. 1412–1427 (cit. on p. 2).
- Gatti, D. and M. Quadrio (2016). "Reynolds-number dependence of turbulent skin-friction drag reduction induced by spanwise forcing". In: *J. Fluid Mech.* 802, pp. 553–58 (cit. on pp. 9–11, 20, 24, 33, 36, 41, 46, 59, 98).
- Gatti, D., A. Güttler, B. Frohnappel, and C. Tropea (2015). "Experimental assessment of spanwise-oscillating dielectric electroactive surfaces for turbulent drag reduction in an air channel flow". In: *Exp. Fluids* 56.5, pp. 1–15 (cit. on p. 7).
- Hosseini, S.M., R. Vinuesa, P. Schlatter, A. Hanifi, and D.S. Henningson (2016). "Direct numerical simulation of the flow around a wing section at moderate Reynolds number". In: *Int. J. Heat and Fluid Flow* 61, pp. 117–128 (cit. on p. 64).
- Jansen, K. (1996). "Large-eddy simulation of flow around a NACA 4412 airfoil using unstructured grids". In: *Annual Research Briefs*, pp. 225–232 (cit. on p. 64).
- Jeong, J. and F. Hussain (1995). "On the identification of a vortex". In: *J. Fluid Mech.* 285, pp. 69–94 (cit. on pp. 42, 88).
- Jiménez, J. (2004). "Turbulent Flows over Rough Walls". In: *Ann. Rev. Fluid Mech.* 36, pp. 173–196 (cit. on p. 10).
- Jiménez, J. and A. Pinelli (1999). "The autonomous cycle of near-wall turbulence". In: *J. Fluid Mech.* 389, pp. 335–359 (cit. on p. 2).
- Jung, W.J., N. Mangiavacchi, and R. Akhavan (1992). "Suppression of turbulence in wall-bounded flows by high-frequency spanwise oscillations". In: *Phys. Fluids A* 4 (8), pp. 1605–1607 (cit. on pp. 2, 5).
- Kalitzin, G., G. Medic, G. Iaccarino, and P. Durbin (2005). "Near-wall behavior of RANS turbulence models and implications for wall functions". In: *J. Comp. Physics* 204.1, pp. 265 –291 (cit. on p. 24).
- Kametani, Y. and K. Fukagata (2012). "Direct numerical simulation of spatially developing turbulent boundary layer for skin friction drag reduction by wall surface-heating or cooling". In: *J. Turbulence* 14.34, pp. 1–20 (cit. on p. 2).
- Kametani, Y., K. Fukagata, R. Örlü, and P. Schlatter (2016). "Drag reduction in spatially developing turbulent boundary layers by spatially intermittent blowing at constant mass-flux". In: *J. Turbulence* 17.10, pp. 913–929 (cit. on pp. 12, 82).
- Kasagi, N., Y. Hasegawa, and K. Fukagata (2009). "Towards cost-effective control of wall turbulence for skin-friction drag reduction". In: *Advances in Turbulence XII*. Ed. by B. Eckhardt. Vol. 132. Springer, pp. 189–200 (cit. on p. 4).
- Khater, C.J., S. Scharnowski, and C. Cierpka (2016). "Highly resolved experimental results of the separated flow in a channel with streamwise periodic constrictions." In: *J. Fluid Mech.* 796, pp. 257–284 (cit. on p. 37).
- Kim, J. and F. Hussain (1993). "Propagation velocity of perturbations in turbulent channel flow". In: *Phys. Fluids A* 5.3, pp. 695–706 (cit. on p. 6).
- Kim, K. and H.J. Sung (2003). "Effects of periodic blowing from spanwise slot on a turbulent boundary layer". In: *AIAA J.* 41, pp. 1916–1924 (cit. on pp. 12, 82).
- (2006). "Effects of unsteady blowing through a spanwise slot on a turbulent boundary layer". In: *J. Fluid Mech.* 557, pp. 423–450 (cit. on pp. 12, 82).

Bibliography

- Kline, S. J., W. C. Reynolds, F. A. Schraub, and P. W. Runstadler (1967). “The structure of turbulent boundary layers”. In: *J. Fluid Mech.* 30, pp. 741–773 (cit. on p. 2).
- Laflin, K., S. Klausmeyer, T. Zickuhr, J. Vassberg, R. Wahls, J. Morrison, O. Brodersen, M. Rakowitz, E. Tinoco, and J.L. Godard (2005). “Data summary from second AIAA computational fluid dynamics drag prediction workshop”. In: *J. Aircraft* 42.5, pp. 1165–1178 (cit. on p. 22).
- Luchini, P. (2013). “Linearized no-slip boundary conditions at a rough surface”. In: *J. Fluid Mech.* 737, pp. 349–367 (cit. on p. 38).
- (2016). “Immersed-boundary simulation of turbulent flow past a sinusoidally undulated river bottom”. In: *Eur. J. Mech. B / Fluids* 55, pp. 340–347 (cit. on p. 38).
- (2018). “Structure and interpolation of the turbulent velocity profile in parallel flow”. In: *Eur. J. Mech. B/Fluids* 71, pp. 15–34 (cit. on p. 105).
- Luchini, P. and F. Charru (2017). “Quasilaminar regime in the linear response of a turbulent flow to wall waviness”. In: *Phys. Rev. Fluids* 2 (1), p. 012601 (cit. on pp. 13, 14, 103–105, 110, 116, 119).
- (2019). “On the large difference between Benjamin’s and Hanratty’s formulations of perturbed flow over uneven terrain”. In: *J. Fluid Mech.* 871, pp. 534–561 (cit. on pp. 13, 14, 103, 104, 110, 116, 119).
- Lumley, J. L. (1973). “Drag reduction in turbulent flow by polymer additives”. In: *J. Polymer Science: Macromolecular Rev.* 7.1, pp. 263–290 (cit. on p. 10).
- Marquillie, M., U. Ehrenstein, and J.P. Laval (2011). “Instability of streaks in wall turbulence with adverse pressure gradient”. In: *J. Fluid Mech.* 681, pp. 205–240 (cit. on pp. 37, 53).
- Marquillie, M., J.-P. Laval, and R. Dolganov (2008). “Direct numerical simulation of a separated channel flow with a smooth profile”. In: *J. Turbulence* 9, pp. 1–23 (cit. on pp. 37, 40).
- Matai, R. and P. Durbin (2019). “Large-eddy simulation of turbulent flow over a parametric set of bumps”. In: *J. Fluid Mech.* 866, pp. 503–525 (cit. on pp. 112, 114–116).
- Mele, B., R. Tognaccini, and P. Catalano (2016). “Performance assessment of a transonic wing-body configuration with ripples installed”. In: *J. Aircraft* 53.1, pp. 129–140 (cit. on pp. 11, 14, 20, 21, 24, 25, 28, 33, 34, 62, 64).
- Memmolo, A. (2018). “Numerical study of transonic buffet on supercritical airfoil with different boundary layer states”. PhD thesis. Sapienza-University of Rome (cit. on pp. 66–68).
- Memmolo, A., M. Bernardini, and S. Pirozzoli (2018). “Scrutiny of buffet mechanisms in transonic flow”. In: *Int. J. Numerical Methods for Heat & Fluid Flow* 28.5, pp. 1031–1046 (cit. on p. 65).
- Mickley, H.S., R.C. Ross, A.L. Squyers, and W.E. Stewart (1954). “Heat, mass, and momentum transfer for flow over a flat plate with blowing or suction, NACA Techn”. In: *NACA Techn. Note* 3208 (cit. on pp. 3, 11).
- Mollicone, J.-P., F. Battista, P. Gualtieri, and C. M. Casciola (2017). “Effect of geometry and Reynolds number on the turbulent separated flow behind a bulge in a channel”. In: *J. Fluid Mech.* 823, pp. 100–133 (cit. on pp. 37, 54).
- (2018). “Turbulence dynamics in separated flows: the generalised Kolmogorov equation for inhomogeneous anisotropic conditions”. In: *J. Fluid Mech.* 841, pp. 1012–1039 (cit. on pp. 37, 112–114, 116).

-
- Mollicone, J.-P., M. Sharifi, F. Battista, P. Gualtieri, and C. M. Casciola (2019). “Particles in turbulent separated flow over a bump: effect of the Stokes number and lift force”. In: *arxiv* 1907:02270v1, pp. 1–8 (cit. on p. 38).
- Nakanishi, R., H. Mamori, and K. Fukagata (2012). “Relaminarization of turbulent channel flow using traveling wave-like wall deformation”. In: *Int J Heat Fluid Flow* 35, pp. 152–159 (cit. on p. 2).
- Orlandi, P. (2006). *Fluid flow phenomena: a numerical toolkit*. Kluwer Academic Publishers (cit. on p. 65).
- Orlandi, P. and J. Jiménez (1994). “On the generation of turbulent wall friction”. In: *Phys. Fluids* 6.2, pp. 634–641 (cit. on p. 2).
- Pamiès, M., E. Garnier, A. Merlen, and P. Sagaut (2007). “Response of a spatially developing turbulent boundary layer to active control strategies in the framework of opposition control”. In: *Phys. Fluids* 19.10, pp. 108–102 (cit. on pp. 12, 82).
- Park, J. and H. Choi (1999). “Effects of uniform blowing or suction from a spanwise slot on a turbulent boundary layer flow”. In: *Phys. Fluids* 11.10, pp. 3095–3105 (cit. on pp. 12, 82).
- Poinsot, T.J. and S.K. Lele (1992). “Boundary conditions for direct simulations of compressible viscous flows”. In: *J. Comp. Phys.* 101.1, pp. 104–129 (cit. on p. 65).
- Pope, S.B. (2000). *Turbulent Flows*. Cambridge University Press, Cambridge (cit. on p. 9).
- Quadrio, M., B. Frohnnapfel, and Y. Hasegawa (2016). “Does the choice of the forcing term affect flow statistics in DNS of turbulent channel flow?” In: *Eur. J. Mech. B / Fluids* 55, pp. 286–293 (cit. on p. 39).
- Quadrio, M. and P. Luchini (2003). “Integral time-space scales in turbulent wall flows”. In: *Phys. Fluids* 15.8, pp. 2219–2227 (cit. on p. 39).
- Quadrio, M. and P. Ricco (2004). “Critical assessment of turbulent drag reduction through spanwise wall oscillation”. In: *J. Fluid Mech.* 521, pp. 251–271 (cit. on p. 6).
- (2011). “The laminar generalized Stokes layer and turbulent drag reduction”. In: *J. Fluid Mech.* 667, pp. 135–157 (cit. on pp. 7, 54, 99).
- Quadrio, M., P. Ricco, and C. Viotti (2009). “Streamwise-traveling waves of spanwise wall velocity for turbulent drag reduction”. In: *J. Fluid Mech.* 627, pp. 161–178 (cit. on pp. 7, 8, 20, 36, 40, 58).
- Quadrio, M. and S. Sibilla (2000). “Numerical simulation of turbulent flow in a pipe oscillating around its axis”. In: *J. Fluid Mech.* 424, pp. 217–241 (cit. on p. 5).
- Rapp, C. and M. Manhart (2011). “Flow over periodic hills: an experimental study.” In: *Exp. Fluids* 51.1, pp. 247–269 (cit. on p. 37).
- Ricco, P. and M. Quadrio (2008). “Wall-oscillation conditions for drag reduction in turbulent channel flow”. In: *Int. J. Heat Fluid Flow* 29, pp. 601–612 (cit. on p. 5).
- Schlatter, P. and R. Örlü (2012). “Turbulent boundary layers at moderate Reynolds numbers: inflow length and tripping effects”. In: *J. Fluid Mech.* 710, pp. 5–34 (cit. on p. 67).
- Shan, H., L. Jiang, and C. Liu (2005). “Direct numerical simulation of flow separation around a NACA 0012 airfoil”. In: *Computers & fluids* 34.9, pp. 1096–1114 (cit. on p. 64).
- Simpson, R.L., Y.T. Chew, and B.G. Shivaprasad (1981). “The structure of a separating turbulent boundary layer. Part 1. Mean flow and Reynolds stresses”. In: *J. Fluid Mech.* 113, pp. 23–51 (cit. on pp. 57, 58).
- Skote, M. (2011). “Turbulent boundary layer flow subject to streamwise oscillation of spanwise wall-velocity”. In: *Phys. Fluids* 23.081703, p. 4 (cit. on p. 7).

Bibliography

- Spalart, P.R. and J.D. McLean (2011). “Drag reduction: enticing turbulence, and then an industry”. In: *Phil. Trans. R. Soc. A* 369.1940, pp. 1556–1569 (cit. on p. 2).
- Stroh, A., Y. Hasegawa, P. Schlatter, and B. Frohnapfel (2016). “Global effect of local skin friction drag reduction in spatially developing turbulent boundary layer”. In: *J. Fluid Mech.* 805, pp. 303–321 (cit. on pp. 12, 51, 82).
- Sumitani, Y. and N. Kasagi (1995). “Direct Numerical Simulation of Turbulent Transport with Uniform Wall Injection and Suction”. In: *AIAA J.* 33.7, pp. 1220–1228 (cit. on p. 12).
- Temmerman, L. and M.A. Leschziner (2001). “Large Eddy Simulation of separated flow in a streamwise periodic channel construction”. In: *Int. Symp. on Turbulence and Shear Flow Phenomena, Stockholm, June 27-29, 2001* (cit. on p. 37).
- Touber, E. and M.A. Leschziner (2012). “Near-wall streak modification by spanwise oscillatory wall motion and drag-reduction mechanisms”. In: *J. Fluid Mech.* 693, pp. 150–200 (cit. on p. 9).
- Viotti, C., M. Quadrio, and P. Luchini (2009). “Streamwise oscillation of spanwise velocity at the wall of a channel for turbulent drag reduction”. In: *Phys. Fluids* 21, p. 115109 (cit. on pp. 6, 7).
- Walsh, M.J. and A. Lindemann (1984). “Optimization and application of riblets for turbulent drag reduction”. In: *AIAA Paper 84-0347* (cit. on pp. 2, 20).
- Webster, D.R., D.B. Degraaff, and J.K. Eaton (1996). “Turbulence characteristics of a boundary layer over a swept bump”. In: *J. Fluid Mech.* 323, pp. 1–22 (cit. on p. 37).
- Wilcox, D.C. (1998). *Turbulence modeling for CFD*. Vol. 2. DCW industries La Canada, CA (cit. on pp. 11, 20).
- Wu, X. and K.D. Squires (1998). “Numerical investigation of the turbulent boundary layer over a bump”. In: *J. Fluid Mech.* 362, pp. 229–271 (cit. on pp. 37, 53, 112, 114–116).
- Yakeno, A., S. Kawai, T. Nonomura, and K. Fujii (2015). “Separation control based on turbulence transition around a two-dimensional hump at different Reynolds numbers”. In: *Int. J. Heat Fluid Flow* 55, pp. 52–64 (cit. on p. 38).
- Yao, J. and F. Hussain (2019). “Supersonic turbulent boundary layer drag control using spanwise wall oscillation”. In: *J. Fluid Mech.* 880, pp. 388–429 (cit. on p. 9).
- Yudhistira, I. and M. Skote (2011). “Direct numerical simulation of a turbulent boundary layer over an oscillating wall”. In: *J. Turbulence* 12.9, pp. 1–17 (cit. on pp. 24, 67).